NASA Innovation Fund 2010 Project

Elastically Shaped Future Air Vehicle Concept

Nhan Nguyen

NASA Ames Research Center

Intelligent Systems Division

M/S 269-1

Moffett Field, CA 94035

October 8, 2010

Executive Summary

This report presents the findings of the NASA Innovation Fund project entitled "Elastically Shaped Air Vehicle Concept". The study has completed all the objectives as outlined in the NASA Innovation Fund proposal. New concrete ideas have been developed to meet the intent and spirit of the NASA Innovation Fund Award. Three emerging themes have been developed in support of meeting national and global aviation challenges of reducing fuel burn for present and future aviation systems. These themes are intertwined and promote the multi-disciplinary nature of the goal of drag reduction in current and future air vehicles.

The first theme addresses the drag reduction goal through innovative vehicle configuration optimization with innovative thinking on wing shapes. Three new promising concepts have been identified from this theme through aerodynamic optimization: a drooped wing shape, an inflected wing shape, and a squashed fuselage. The drooped wing shape is a truly biologically inspired wing concept that mimics a seagull wing and could achieve about 5% to 6% drag reduction, which is aerodynamically significant. The aerodynamic efficiency gain is theoretically justifiable from aeroelasticity theory. From a practical perspective, this concept would require new radical changes to the current aircraft development capabilities for new vehicles with futuristic-looking wings such as this concept. One idea that could support this new wing shape would be to incorporate articulating mechanisms for increasing ground clearance during take-off and landing by rotating upward a portion of the wing tip.

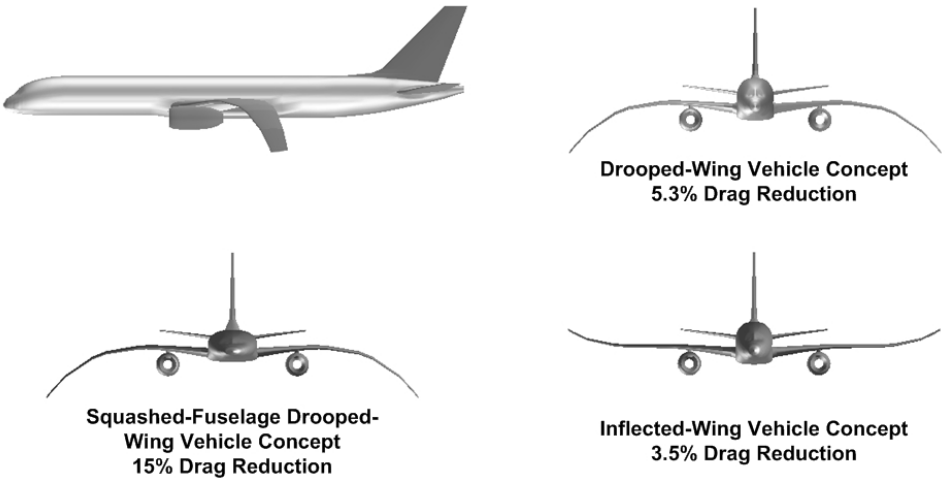

The inflected wing concepts could achieve between 3% to 4% drag reduction. While the benefit may be modest with the inflected wing, the concept could have a near-term impact since this concept could be developed within the current aircraft development capabilities. The squashed fuselage concept is found to have a substantial drag reduction benefit. Up to 15% drag reduction has been seen in the study. By changing the aspect ratio of the cross sections of the fuselage while maintaining the same cross sectional areas, the fuselage can contribute to vehicle lift, thereby reducing the wing lift which in turn reduces lift-induced drag. As with the inflected wing concept, the squashed fuselage could have a near-term impact.

The second theme addresses the drag reduction goal through a new concept of elastic wing shaping control. The multi-disciplinary nature of flight physics is appreciated with the recognition of the adverse effects of aeroelastic wing shape deflections on aerodynamic drag. By aeroelastically tailoring the wing shape with active control, a significant drag reduction benefit could be realized. A 17% drag reduction for long-range cruise from elastic wing shaping control could be realized as has been shown in the study when compared with the drooped-wing aircraft configuration without elastic wing shaping control.

To realize the potential of the elastic wing shaping control concept, the third theme emerges that addresses the drag reduction goal through a new type of aerodynamic control surfaces. This concept is referred to as variable camber continuous trailing edge flap. Conventional aerodynamic control surfaces are discrete independent surfaces that cause geometric discontinuities at the trailing edge region. These discontinuities promote vorticities which result in drag rises. The variable camber trailing edge flap concept could provide a substantial drag reduction benefit over a conventional discrete flap system. Aerodynamic simulations show a drag reduction of over 50% could be achieved with the flap concept over a conventional discrete flap system. Moreover, elastic wing shaping control potential could only be realized with low drag aerodynamic control surfaces such as this flap concept.

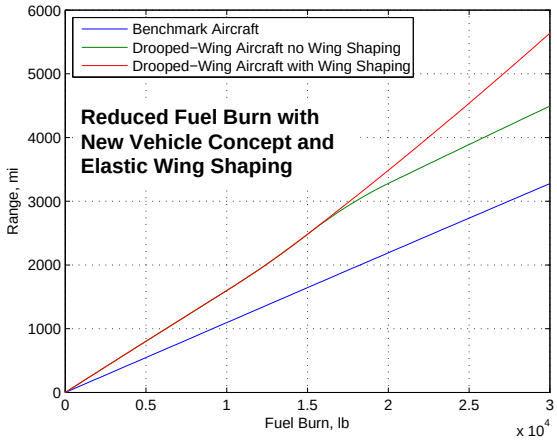

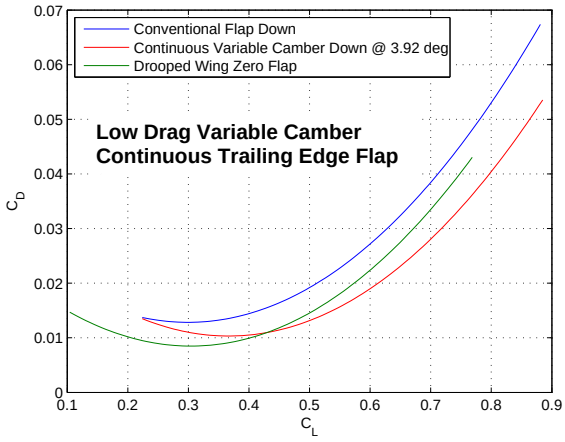

Research and technology development of new vehicle concepts to support the drag reduction goal requires a multi-disciplinary approach that integrates knowledge domains across different disciplines to bring forth potential solutions that recognize the interactive nature of these disciplines in contributing to the common goal of drag reduction. The project recognizes this important aspect of research and technology development and proceeds to conduct a multi-disciplinary study that brings together a diverse set of disciplines in aerodynamics, optimization, structural analysis and aeroelasticity, flight dynamics and control, and system analysis to develop integrated solutions for future air vehicle systems.

The potential significant contributions of this project to future aviation systems in supporting national and global challenges of fuel efficiency could only be realized by continuing to advance these new ideas toward higher levels of technology readiness through a scientific discovery process that would require more thorough analysis, computation, and experimentation than what has been accomplished by this project within the four-month performance period. Toward that end, the project has compiled a list of recommendations from NASA project personnel and Boeing Research and Technology in St. Louis, the project's industry partner, for a possible follow-on effort to mature these ideas into new areas for research and technology development for future aviation systems. In particular, Boeing Research and Technology has expressed a strong interest in future partnership with NASA to further advance the system-level concepts developed by the project; namely, the variable camber continuous trailing edge flap and the elastic wing shaping control, for possible future aircraft applications. Furthermore, Boeing Research and Technology has also indicated that they will share the results of this study with Boeing Airplane Company in Seattle.

In terms of other accomplishments, the project has filed a NASA Disclosure of Invention and New Technology (Including Software) entitled "Variable Camber Continuous Aerodynamic Control Surfaces and Methods for Active Wing Shaping Control" with NASA Ames Office of the Chief Counsel on October 8, 2010. On a related note, upon a request of the NASA Aeronautics Research Mission Directorate (ARMD) Subsonic Fixed Wing (SFW) project personnel at NASA Langley at the final project meeting, the project has agreed to allow the SFW project personnel to use the variable camber continuous trailing edge flap concept for their future work. The project is also planning to file one or more invention disclosures on the new aircraft concepts developed by the project. In addition, the project will also plan to file an invention disclosure on the aircraft optimization software tool as well as to further develop the optimization tool for future NASA work. The project will plan to publish the results of this study through NASA publication such as NASA Technical Memorandum and technical papers at the American Institute of Aeronautics and Astronautics (AIAA) Atmospheric Flight Mechanics Conference in 2011 and Aerospace Sciences Meeting in 2012.

In closing, the project team wishes to thank NASA Innovative Partnerships Program for their funding support of this project that has allowed new ideas to be developed that could make positive impacts on the future of aviation.

Acknowledgment

The project wishes to acknowledge NASA Innovative Partnerships Program for their NASA Innovation Fund support and NASA Aeronautics Research Mission Directorate for their technical support through the Subsonic Fixed Wing Project under the Fundamental Aeronautics Program. The technical execution of this project is contributed by NASA Ames, NASA Langley, Boeing Research and Technology, and California State University Sacramento. The project wishes to acknowledge the following personnel for their contribution, consultation, and participation

NASA Ames Research Center
Moffett Field, CA 94035

Nhan Nguyen

Susan Frost

Khanh Trinh (Stinger Ghaffarian Technologies Inc.)

Kevin Reynolds

Joe Totah

James Kless (Science & Technology Corp.)

Thomas Pulliam

Michael Aftosmis

Marian Nemec (Science & Technology Corp.)

Michael Rogers

NASA Langley Research Center
Hampton, VA 23681

Suresh Joshi

Parag Patre (LaRC PostDoctoral)

Karen Taminger

James Moore

Carol Wieseman

NASA Dryden Flight Research Center
Edwards, CA 93523

Steven Jacobson

Brian Taylor

Boeing Research and Technology
St. Louis, MO 63166

James Urnes, Sr.

Timothy Smith

Charles Morris

California State University Sacramento
Sacramento, CA 95819

Ilhan Tuzcu

Carnegie Mellon University Silicon Valley
Moffett Field, CA 94035

Abraham Ishihara

Contents

1 Background

NASA is taking a lead role in developing a "green" aviation initiative that begins to seek technology development for environmentally responsible future aviation systems to meet national and global challenges of improving aircraft fuel efficiency while reducing noise and emissions. NASA leadership in this area is important to maintain its preeminent heritage in aeronautics. Green aviation focuses on new aeronautic technologies that could potentially revolutionize aviation systems that could lead to improved aerodynamic efficiency, less fuel burn, and reduced noise and emissions. These important goals represent current challenges in the present aviation systems in response to the emerging needs for innovative aircraft design that can address future aviation systems. In the context of commercial aviation, civilian aircraft remains the largest U.S. export category ($9.4 billion, "U.S. Export Fact Sheet, March 2009). The increasing demand for fuel-efficient aircraft for global commerce prompts the aircraft industry to address improved fuel efficiency as a top national and global challenge.

The "elastically shaped future air vehicle concept" represents an innovative approach that holds potential to help realize the goal of drag reduction that can directly address the global challenge of improving aircraft fuel efficiency. This concept is a significant departure from a conventional design, but is firmly grounded in science, thus making it a revolutionized, yet realizable concept.

Air vehicles are typically designed to maintain sufficient structural rigidity for safe load-carrying capacity. Modern engineered materials such as composites have begun to appear in new airframe designs that can provide less structural rigidity while maintaining the same load-carrying capacity. A good example of a current airframe design that leverages light-weight composites materials is the Boeing 787 Dreamliner aircraft, which exhibits a greater degree of wing flexibility than an older-generation aircraft design. Thus, there is a realization that future air vehicle concepts can be developed to take advantage of the structural flexibility afforded by modern engineered materials to improve aerodynamic efficiency.

Elastically shaped air vehicle is a concept whereby highly flexible aerodynamic surfaces are elastically shaped in-flight by actively controlling the wing wash-out twist and wing bending deflection in order to change the local angle of attack in such a manner that can result in lower fuel burn by drag reduction during cruise and or enhanced performance during take-off and landing by increasing lift. Moreover, structural flexibility will be leveraged to realize a revolutionary, optimal wing shape design that can accommodate a significant curvature for drag reduction benefits as opposed to a conventional straight wing design. Elastically shaped air vehicle, therefore, may be viewed as a biologically-inspired concept that could potentially revolutionize the conventional airframe design. Taking a cue from birds' efficient shape-changing wings, this concept may be able to bring future air vehicle concepts to the next level in terms of performance, efficiency, and maneuverability.

To realize the goals of this proposal, this project conducts a feasibility study with the funding support of NASA Innovation Fund Award sponsored by NASA Innovative Partnerships Program. The plan of this study is to conduct a multi-disciplinary design, analysis and optimization to examine the potential benefits of the elastically shaped future air vehicle concept over a conventional vehicle design. The four major technical areas of the study are:

1. Vehicle conceptual design and optimization – A futuristic elastically shaped wing superimposed on an available commercial transport fuselage will be designed using aerodynamic strip theory and vortex lattice aerodynamic code. Optimization will be conducted to identify an optimal shape defined by the varying curvature and wash-out twist of the elastic wing that minimizes induced drag or maximizes lift-to-drag ratio, hence aircraft range. A comparative study of the fuel savings will be made using available performance data for a representative commercial transport and engines.

2. Aeroelastic flight dynamic modeling – A static and dynamic aeroservoelastic model of the elastically shaped wing will be developed in conjunction with a flight dynamic model for analyzing aerodynamics, stability and control of the elastically shaped air vehicle.

3. Elastically wing shaping actuation design – A low drag distributed actuation concept will be developed to size and strategically place new aerodynamic surfaces throughout the elastically shaped wing. The distributed control surfaces will be used to actively shape the elastic wing to gain aerodynamic efficiency. Commercially available sensor technology for shape measurement will be leveraged and assumed to be available for elastically wing shaping control.

4. Flight control design and vehicle simulation – A multi-objective flight control system will be developed to simultaneously gain aerodynamic efficiency and maintain traditional pilot command-tracking tasks for guidance

and navigation. A guidance law to achieve a low drag objective will be developed for a cruise phase to specify both the desired drag and vehicle attitude objectives for flight control performance. Multi-objective optimal control will be introduced for flight control design. A complete vehicle control simulation will be performed to demonstrate feasibility.

The technical execution of this project has been performed by NASA Ames and Langley, as well as through external partnerships with Boeing Research and Technology in St. Louis, MO and California State University, Sacramento. Representatives of NASA ARMD Subsonic Fixed Wing (SFW) project from NASA Ames, Langey, and Dryden; and Carnegie-Mellon University personnel attended weekly and bi-weekly web-based meetings and provided useful feedback during the project execution.

The results of this study are now described in detail.

2 Vehicle Aerodynamic Optimization

The goal of this study is to develop new wing shape concepts that will provide aerodynamic benefits of induced drag reduction. To conduct this study, aerodynamic optimization is performed to identify optimal wing shapes that can achieve induced drag reduction. In addition, other ideas of drag reduction are explored besides the wing shape optimization. The ultimate goal of this project is to develop novel aircraft concepts based on optimized wing shapes and other ideas obtained from this study that could potentially provide a breakthrough from the equilibrium in the current aircraft design which has remained virtually unchanged for the past several decades. These new concepts could provide a new impetus to aircraft design for future aviation systems that would operate in a resource-constrained ecosystem.

2.1 Benchmark Vehicle

The benchmark vehicle selected for the study is a notional single-aisle, mid-size, 200-passenger aircraft having a similar outer mold line as Boeing 757. The geometry of the benchmark aircraft is obtained by scaling up the geometry of NASA generic transport model (GTM) by a scale of 200:11. The GTM is a research platform that includes a wind tunnel model, shown in Figure 2.1, and a remotely piloted vehicle, shown in Figure 2.2 [1]. Figure 2.3 is an illustration of the benchmark aircraft. The reason for selecting this benchmark vehicle is that there already exists an extensive wind tunnel aerodynamic database that would be used subsequently in the study for validating results of the optimization study. The benchmark configuration represents one of the most common types of transport aircraft in the commercial aviation sector that provides short-to-medium range passenger carrying capacities.

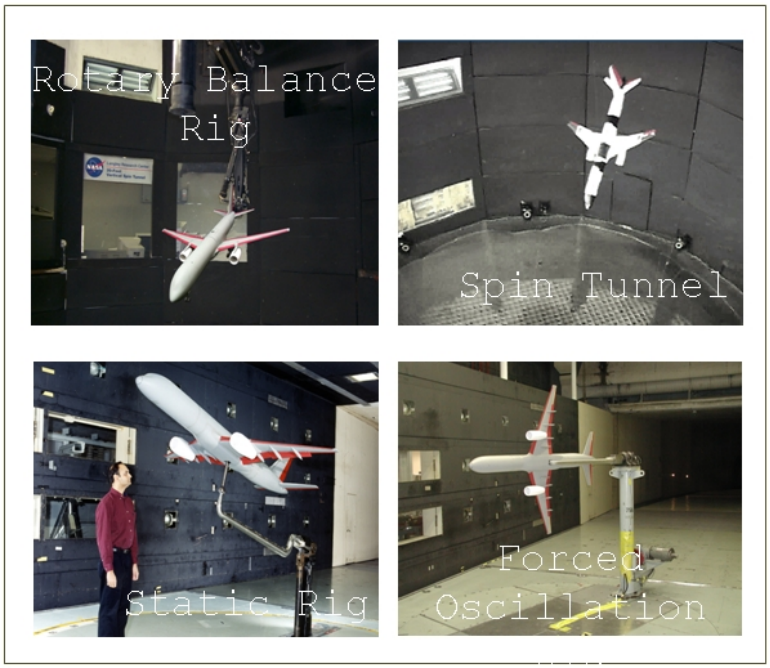

Figure 2.1 - Generic Transport Model (GTM) Undergoing Wind Tunnel Tests in NASA Langley

The aircraft has a take-off weight of 200,000 lbs for a typical operating load (gear up, flap up) that includes cargo, fuel, and passengers. The operational empty weight (OEW) of the aircraft is 132,821 lbs. Fuel weighs about 50,000 lbs for a range of about 3,000 nautical miles. Table 2.1 shows some typical aircraft characteristics:

Wing Reference Area, S_{ref}	1951 ft^2
Aspect Ratio, AR	7.82
Taper Ratio, λ	0.212
MAC, $\bar{c}$	16.6417 ft
Wing Span, b	124.8333 ft
Wing Leading Edge Sweep Angle, Λ	28.4286^o
Wing Dihedral Angle, Γ	5^o

Table 2.1 - Benchmark Aircraft Characteristics

Figure 2.2 - Generic Transport Model (GTM) Remotely Piloted Vehicle at NASA Langley

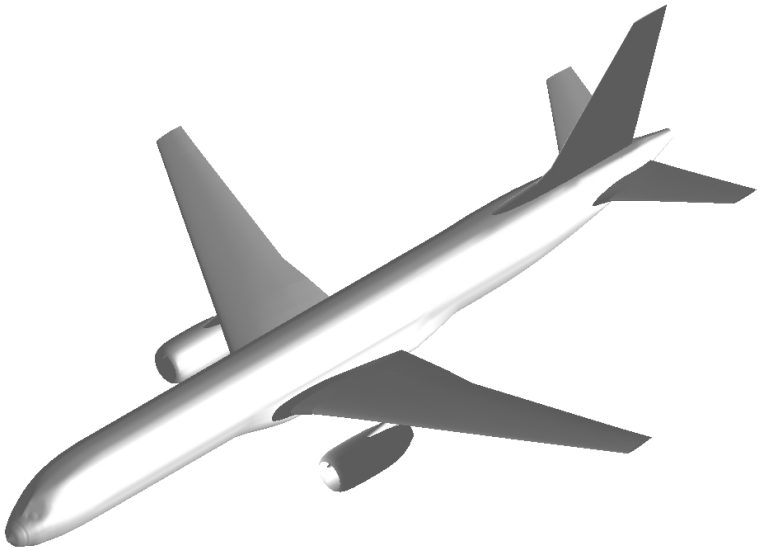

Figure 2.3 - Benchmark Aircraft

With reference to Figure 2.4, the coordinate reference frame (x_B, y_B, z_B) defines the Body Station (BS), the Body Butt Line (BBL), and the Body Water Line (BWL) of the aircraft, respectively. The coordinate reference frame (x_V, y_V, z_V) is the translated coordinate system attached to the nose of the aircraft such that $x_V = x_B - 13.25$ ft, $y_V = y_B$, and $z_V = z_B - 15.8333$ ft. This reference frame is used for the aerodynamic modeling and optimization. The stability reference frame(x, y, z) is attached to the CG such that $x = \bar{x}_V - x_V$, $y = y_V - \bar{y}_V$, and $z = \bar{z}_V - z_V$, where $(\bar{x}_V, \bar{y}_V, \bar{z}_V)$ is the coordinate of the CG in the (x_V, y_V, z_V) reference frame.

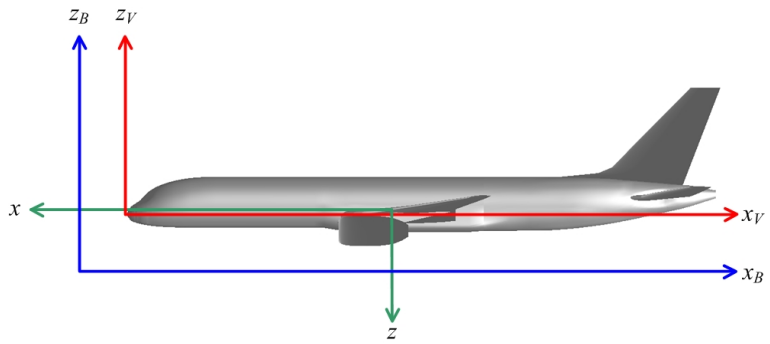

Figure 2.4 - Benchmark Aircraft Coordinate Systems

To compute the mass and inertia properties of the benchmark aircraft, a component-based approach is used. The aircraft is divided into the following components: fuselage, wings, horizontal tails, vertical tail, engines, operational empty weight (OEW) equipment, and typical load including passengers, cargo, and fuel. The fuselage, wings, horizontal tails, and vertical tail are modeled as shell structures with constant wall thicknesses. Based on [2], an average wing mass relative to the total empty weight of the aircraft is taken to be 24.2% of the OEW. Similarly, the mass contributions of the fuselage and the combined horizontal and vertical tails are taken to be 19.0% and 4.2%, respectively. This equivalent shell model is subsequently used to generate structural stiffness estimates of the concept vehicle for aeroservoelastic flight dynamic modeling to evaluate aeroelastic stability and control issues associated with flexible airframe. The breakdown of mass, CG, and inertia properties of the components is shown in Table 2.2 [3].

	m	$\bar{x}_B$	$\bar{y}_B$	$\bar{z}_B$	$I_{xx,B}$	$I_{yy,B}$	$I_{zz,B}$	$I_{xz,B}$
Fuselage	25293	87.285	0	18.592	303922	7551945	7277573	1285606
Wings	32174	92.543	0	17.318	1295119	8926720	9616518	1610173
Horizontal Tails	2932	157.889	0	21.472	61332	2315773	2292944	309182
Vertical Tail	2690	154.678	0	34.987	106127	2111440	2005368	455436
Engines	23000	77.000	0	12.167	440314	4354793	4578404	670400
Equipment	46732	77.648	0	16.566	38867	11318764	10552349	1828149
Typical Load	67179	86.832	0	17.178	1312885	17385143	17442859	3120326
Typical GTM	200000	86.486	0	16.963	3558565	53964579	53766014	9279272

Table 2.2 - Estimated Component Weight (lb), CG (ft), and Inertias of Benchmark Aircraft in (x_B, y_B, z_B) Reference Frame

The aircraft is powered by two 44,000-lb rated turbofan engines. The maximum thrust per engine at sea level take-off is 44,000 lbs and varies linearly to 30,000 lbs at sea level Mach 0.8 The thrust specific fuel consumption (TSFC) at sea level take-off is 0.3460 /hr and varies linearly to 0.6656 /hr at sea level Mach 0.8. The total maximum engine thrust and TSFC as functions of altitude and Mach number are given by the following formulas:

$$T_{max}(h,M) = (-77031M + 100986)\left(1 + \frac{\gamma-1}{2}M^2\right)^{\frac{\gamma}{\gamma-1}}\delta(h) \tag{2.1}$$

$$c(M,h) = (0.45642M + 0.26156)\sqrt{\theta(h)\left(1 + \frac{\gamma-1}{2}M^2\right)} \tag{2.2}$$

where T_{max} is the maximum thrust, c is the TSFC, M is Mach number, $\delta = p/p_{SL}$ is the pressure ratio, $\theta = T/T_{SL}$ is the temperature ratio, and p_{SL} and T_{SL} are the pressure and temperature at sea level.

The TSFC represents the fuel burn rate, thus an important parameter in the estimation of range and fuel burn.

2.2 Computational Aerodynamic Tools

Two computational tools are used in the study. A vortex-lattice computational code, called VORVIEW, is used extensively in the design, analysis, and optimization for the development of elastically shaped air vehicle concepts [4]. Another computational fluid dynamic (CFD) tool, Cart3D, is used for validation of candidate optimized vehicle concepts identified by the optimization study [5]. Both of these tools have been used in the past for modeling the NASA GTM. Therefore, some amount of validation has been done previously to compare the computational results of these two codes with wind tunnel data.

VORVIEW provides a rapid method for estimating aerodynamic force and moment coefficients as well as aerodynamic stability and control derivatives of a given aircraft configuration. It is based on the vortex-lattice aerodynamic theory. The vehicle configuration is constructed within VORVIEW by a series of panels that are formed by spanwise and chordwise locations of bound vortices. VORVIEW computes the vehicle aerodynamics in both the longitudinal and lateral directions independently. The longitudinal and lateral aerodynamics are then combined to produce overall aerodynamic characteristics of the vehicle at any arbitrary angle of attack and angle of sideslip. Due to the inviscid nature of any vortex-lattice method, the drag prediction by VORVIEW is most reliable for induced drag prediction. For viscous drag due to boundary layer separation or wave drag due to shock-induced boundary layer separation, the prediction may be less reliable. VORVIEW can provide a rapid estimation of aerodynamic derivatives including dynamic derivatives due to angular rates. Owing to the computationally efficient vortex-lattice method, aerodynamic derivatives can be estimated in VORVIEW fairly quickly. A flight dynamic model for a given vehicle configuration can be easily developed with VORVIEW that supplies the model with all necessary aerodynamic information for the vehicle.

Cart3D is a high-fidelity, three-dimensional Euler solver suitable for CFD analysis on complex geometries. Cart3D has a mesh adaptation feature that uses adjoint-weighted residual error estimates to drive mesh adaptation for user selected outputs (such as drag or lift). In this way, the mesh refinement procedure generates a mesh that reduces the discretization errors in the outputs so that the influence of these errors on the output functional is below a specified error tolerance. A more complete analysis of the adjoint formulation and its applications on complex geometries can be found in [6] and [7]. Another valuable capability of Cart3D is the ability to achieve a user-requested value of C_L by modifying the angle of attack at specified time steps. This capability can be helpful in comparing induced-drag benefits across different geometries.

2.3 Automated Vehicle Geometry Modeling Tool

Aircraft configuration optimization requires an efficient way to generate new vehicle configurations during the optimization. An automated vehicle geometry modeling tool has been developed in MATLAB specifically for the optimization study. The vehicle geometry modeler directly outputs a geometry input file that can be read by VORVIEW during the optimization. The vehicle geometry modeler has access to the outer mold line geometry information of the full-scale GTM. The coordinate reference frame (x_V, y_V, z_V) defines the coordinate system used in the vehicle geometry model. Wing chordwise and flapwise bending deflection shapes and a twist distribution are superimposed on top of the wing geometry as shown in Figure 2.5. A new wing geometry is generated by performing successive coordinate translation and rotation. The order of the coordinate transformation is important. To reduce the frontal area of the wing due to twist which can affect drag, the order of the coordinate transformation is as follows:

1. A coordinate rotation to account for twist is performed first by rotating a baseline wing section about its area center by a specified twist angle at a given y_V-coordinate. The transformed coordinates due to twist are computed as

$$x_V^{'} = \bar{x} + (x_V - \bar{x})\cos\Theta(y_V) - (z_V - \bar{z})\sin\Theta(y_V) \tag{2.3}$$

$$z_V^{'} = \bar{z} + (x_V - \bar{x})\sin\Theta(y_V) + (z_V - \bar{z})\cos\Theta(y_V) \tag{2.4}$$

   where Θ is the twist angle, positive nose-down and negative nose-up.

2. A coordinate translation in the x_V-direction to account for chordwise bending is performed next by translating the previously transformed $x_V^{'}$-coordinate by a specified chordwise bending deflection at a given y_V-coordinate. The transformed coordinates due to chordwise bending are computed as

$$x_V^{''} = x_V^{'} + V(y_V) \tag{2.5}$$

$$z_V'' = z_V' \tag{2.6}$$

where V is the chordwise bending deflection, positive swept back and negative swept forward.

3. Finally, a coordinate translation in the z_V-direction to account for flapwise bending is performed by translating the previously transformed z_V'' by a specified flapwise bending deflection at a given y_V-coordinate. The transformed coordinates due to flapwise bending are computed as

$$x_V''' = x_V'' \tag{2.7}$$

$$z_V''' = z_V'' + W(y_V) \tag{2.8}$$

where W is the flapwise bending deflection, positive up and negative down.

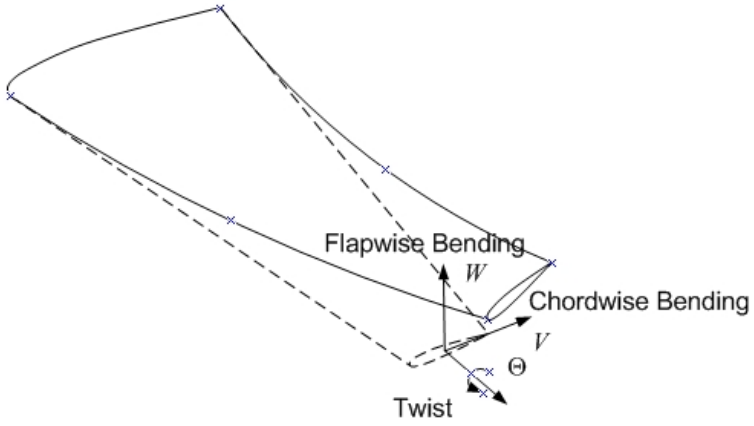

Figure 2.5 - Wing Bending Deflections and Twist

It is noted that the coordinate transformation is not length-preserving since as the curvature increases, the wing span also increases. The increase in the wing span can be computed as

$$\Delta b = 2\int_{y_r}^{y_t}\left(\sqrt{1+\left[V'(y_V)\right]^2+\left[W'(y_V)\right]^2}-1\right)dy \approx \int_{y_r}^{y_t}\left\{\left[V'(y_V)\right]^2+\left[W'(y_V)\right]^2\right\}dy \tag{2.9}$$

The engine geometry and the pylon geometry are also affected by the coordinate transformation of the wing geometry. Thus, coordinate transformations of the engine geometry and the pylon geometry are also performed in order to keep the relative positions of the engines and pylons with respect to the wing geometry the same at the engine mount locations on the wings.

The vehicle geometry also includes the following additional features:

- A "squashed" fuselage geometry can be modeled by scaling the y_V and z_V-coordinates of the fuselage by specified scaling factors. The squashed fuselage concept is of particular interest, since it can provide an additional lift contribution derived from the fuselage itself. As a result, the wing lift is reduced that results in lower lift-induced drag. The squashed fuselage concept will be discussed in the subsequent section on optimization.

- A "high-wing" geometry allows the wing position to be placed above the fuselage centerline. The majority of commercial aircraft are of low-wing configurations which provide added roll stability with a positive wing dihedral. Many military transports such as C-5 are designed with a high-wing configuration.

- A "V-tail" geometry is available that allows the V-tails to serve as both directional stabilizer and horizontal stabilizer. This can be an advantage if the wing curvature is significant that can also contribute to the directional stability, thereby allowing the vertical tail to be eliminated for weight savings.

- A new type of low-drag continuous trailing edge (TE) flap concepts has been developed as part of this study and is also included in the vehicle geometry model. The benefit of drag reduction due to this type of flap concepts will be shown later.

The ability of the geometric modeler to superimpose bending deflection shapes and twist on a rigid wing shape provide a future capability for developing a coupled aeroelastic-aerodynamic modeling tool by coupling an aerodynamic code such as VORVIEW with a structural analysis code that computes bending deflection shapes and twist. This capability would fill a gap that is highly desirable and would greatly benefit studies like the present one.

Figure 2.6 illustrates various vehicle concepts generated by the automated vehicle geometry modeler.

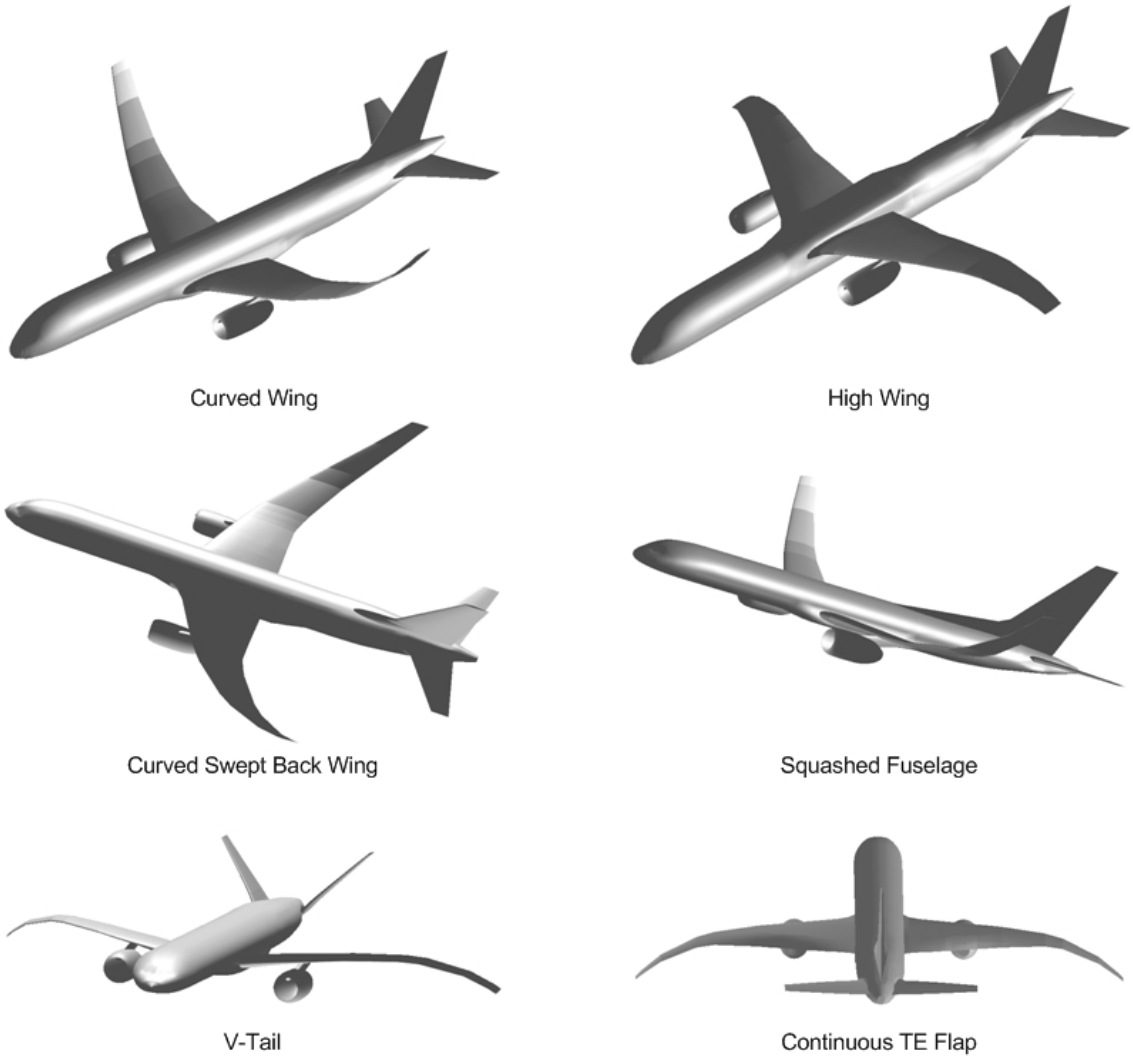

Figure 2.6 - Automated Vehicle Geometry Modeling

2.4 Vehicle Design Optimization Approach

An aerodynamic optimization is conducted to develop candidate elastically shaped air vehicle concepts that achieve lower drag than the benchmark vehicle. The focus of the design optimization is a new wing geometry that replaces the conventional wing of the benchmark vehicle. Any potential benefit of other geometric features such as squashed fuselage or V-tail may be additive to the new wing geometry. Thus, these new features are not part of the optimization.

Given that the use of modern light weight composites materials is becoming more prevalent in modern aircraft due to the benefit of weight savings while providing sufficient load carrying capacities, the conventional straight wing design might give way to a new type of wings that could include significant curvatures and flexibility that could be tailored for improved aerodynamic efficiency. Thus, the goal of the optimization is to allow each wing section to possess all three degrees of freedom in chordwise displacement, flapwise displacement, and twist. These degrees of freedom then would become the design variable in the optimization. In theory, this could be done. However, a simpler

approach is pursued in the interest of time. This approach parametrizes the wing degrees of freedom by using assumed shape functions with unknown coefficients.

In particular, each shape function is described by a 4th degree polynomial with 5 unknown coefficients or design variables. Moreover, the wing sections inboard of BBL 21.6000 ft at the engine sections are assumed to be unaffected due to the large structural stiffness near the wing root that could present a challenge to shape a wing. Thus, the shape function starts at BBL 21.6000 ft. Furthermore, the displacement and slope of the shape function are enforced to be zero at this location. This enforcement reduces the number of design variables from 5 to 3. A further simplification is made by eliminating the chordwise displacement components. Thus, the shape functions are given by

$$W(y_V) = \begin{cases} a_4\left(\frac{y_V-y_e}{y_t-y_e}\right)^4 + a_3\left(\frac{y_V-y_e}{y_t-y_e}\right)^3 + a_2\left(\frac{y_V-y_e}{y_t-y_e}\right)^2 & y_e < y_V \leq y_t \\ 0 & y_V \leq y_e \end{cases} \tag{2.10}$$

$$\Theta(y_V) = \begin{cases} b_4\left(\frac{y_V-y_e}{y_t-y_e}\right)^4 + b_3\left(\frac{y_V-y_e}{y_t-y_e}\right)^3 + b_2\left(\frac{y_V-y_e}{y_t-y_e}\right)^2 & y_e < y_V \leq y_t \\ 0 & y_V \leq y_e \end{cases} \tag{2.11}$$

where $y_e = 21.6000$ ft and $y_t = 62.1286$ ft which is the BBL of the wing tip.

The shape function optimization thus becomes a parametric optimization where the design variables are a_i and b_i, $i = 2,3,4$. Upper and lower limits on the shape functions are imposed as constraints on the flapwise bending displacement and twist at the wing tip such that

$$|W(y_t)| = |a_4 + a_3 + a_2| \leq W_{t,max} \tag{2.12}$$

$$|\Theta(y_t)| = |b_4 + b_3 + b_2| \leq \Theta_{t,max} \tag{2.13}$$

where $W_{t,max} = 20$ ft is the maximum allowable flapwise bending displacement and $\Theta_{t,max} = 4.5^{\circ}$ is the maximum allowable twist at the wing tip.

Moreover, an additional constraint is imposed on the optimization and that is the cruise condition. For a given vehicle weight flying at a given airspeed and altitude, there corresponds a lift coefficient that the vehicle must operate at. Thus, the cruise condition is expressed as

$$C_L = \frac{W}{q_\infty S} \tag{2.14}$$

The design point for the benchmark aircraft is selected for an operating weight of $W = 200,000$ lbs, cruise speed of $M_\infty = 0.8$, and cruise altitude at 30,000 ft. The design cruise lift coefficient is $C_L = 0.364$. This design lift coefficient is enforced during the optimization.

The optimization is conducted using a sampling method over a chosen design space. The design space is chosen such that each design variable a_i and b_i, $i = 2,3,4$, can take on any one of three pre-selected values as shown in Table 2.3 such that the wing tip constraints are satisfied. This is a sample of 729 possible shape functions or design points, which is fairly limited due to the time constraint. All the possible shape functions are plotted in Figures 2.7 and 2.8. Future work will investigate expanding the design space that will include a larger number of sampling points.

a_4	a_3	a_2	b_4	b_3	b_2
$0, \pm 7.5$	$0, \pm 3.75$	$0, \pm 8.75$	$0, \pm 1.5$	$0, \pm 1.5$	$0, \pm 1.5$

Table 2.3 - Design Space for Parametric Optimization

To implement the optimization, a computer code is developed to couple the vehicle geometry modeler with the aerodynamic code VORVIEW. Each design point is evaluated with a different combination of the parameters a_i and b_i, $i = 2,3,4$. The execution time for each design point in VORVIEW is about 2 minutes on a single dual-core CPU computer. Thus, each optimization cycle takes about one day to complete.

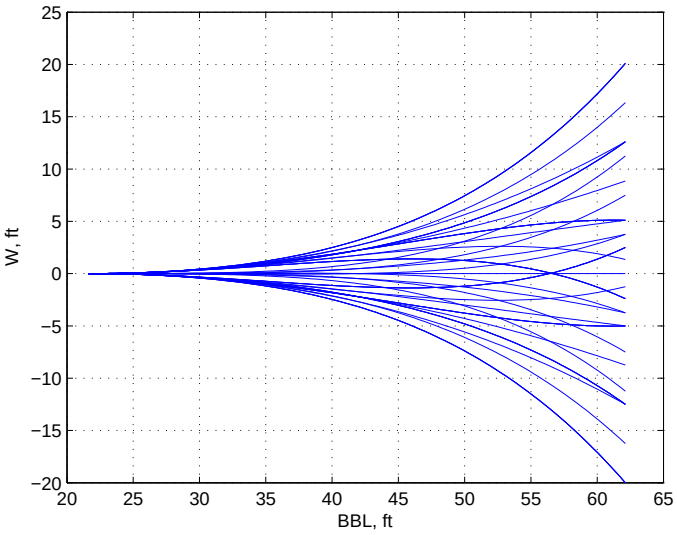

Figure 2.7 - Bending Shape Function Sample

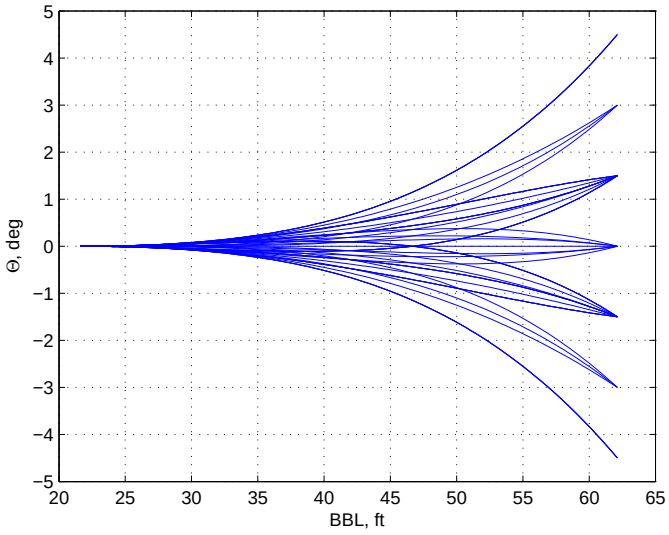

Figure 2.8 - Torsion Shape Function Sample

2.5 Optimization Results

The drag coefficient of the benchmark aircraft at the design flight condition as computed by VORVIEW is $C_D = 0.010$. At each design point, the C_D value corresponding to the design cruise $C_L = 0.364$ is obtained. The results of the C_D calculation from the optimization are plotted in Figure 2.9. Each point on the plot corresponds to a given design. As can be seen, there are several designs with C_D less than that of the benchmark aircraft.

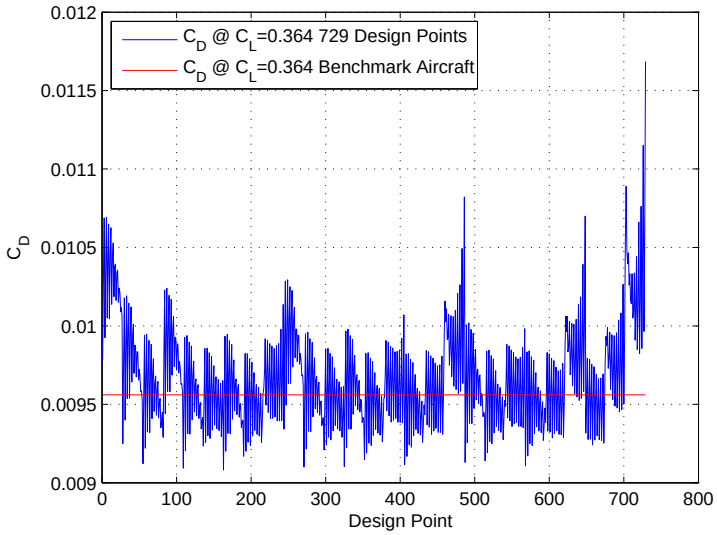

Figure 2.9 - C_D Variation in Design Space

2.5.1 Drooped Wing Shape

The design corresponding to the minimum C_D is identified as a vehicle with a drooped wing shape, which has a significant negative wing curvature with the wing tip at its maximum negative deflection as shown in Figure 2.10. The optimal shape function parameters are a_4 =-7.5, $a_3 = -3.75$, $a_2 = -8.75$, $b_4 = -1.5$, $b_3 = 1.5$, and $b_2 = -1.5$. Figures 2.11 and 2.12 show the mean line of the drooped wing shape and the wing wash-out twist distribution (positive nose-down). The wing tip has a very small ground clearance which can be problematic. Thus, the new wing design would have to incorporate a mechanism to articulate the wing tip portion to increase ground clearance. Nonetheless, notwithstanding practical implementation aspects of this concept, this optimal wing shape is quite interesting and revolutionary. The drooped wing shape in fact seems to mimic a seagull wing. Thus, it could be viewed as a biologically inspired concept. In fact, a literature search reveals that there was a study of a seagull-type wing in a wind tunnel at NASA Langley Research Center in 2006 [8]. The article stated that a seagull wing can be proved to have the greatest drag reduction - a 4 percent improvement over the theoretically best conventional aircraft wing.

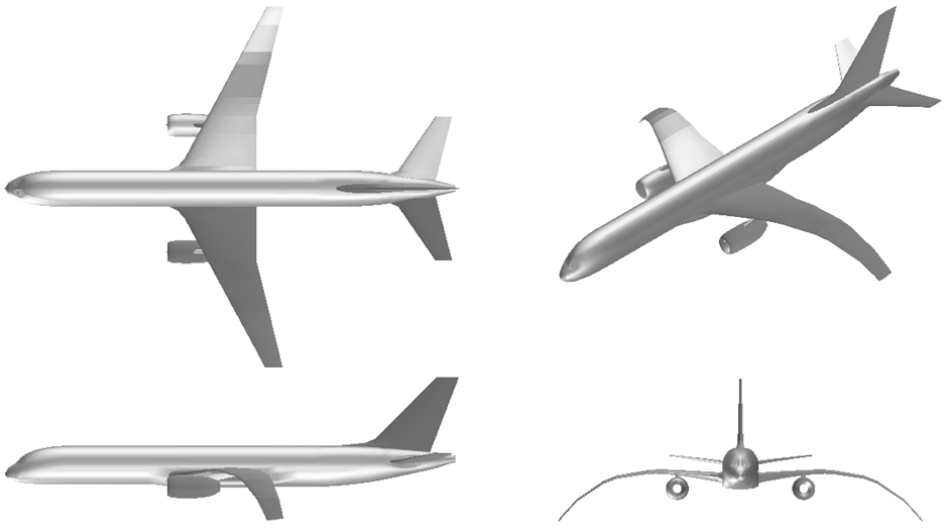

Figure 2.10 - Drooped-Wing Aircraft Concept

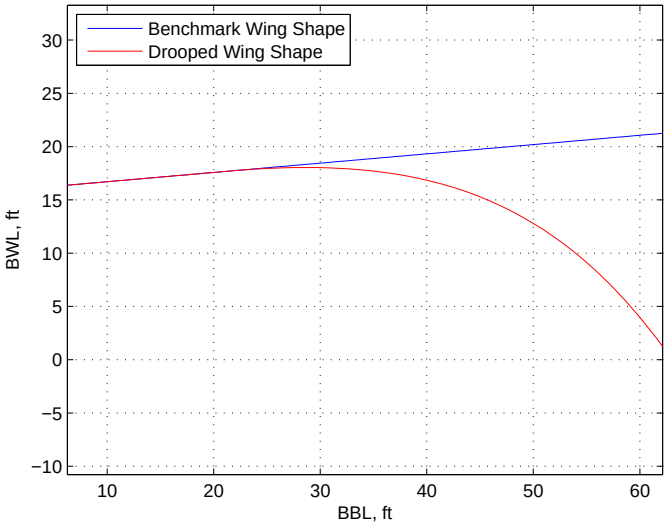

Figure 2.11 - Mean Line of Drooped Wing Shape

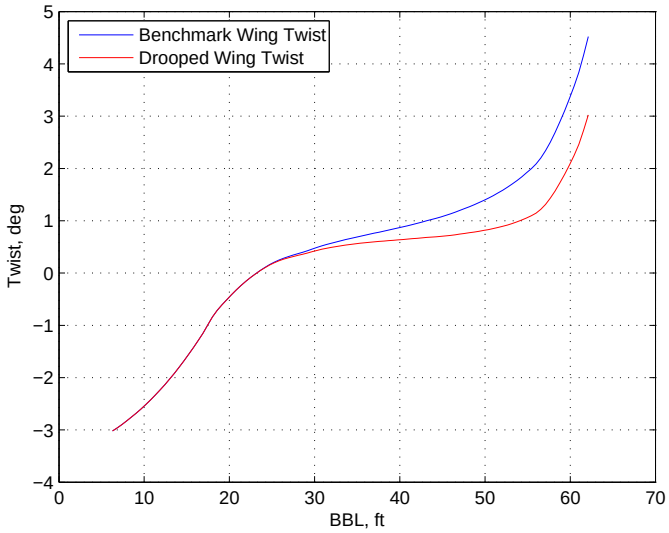

Figure 2.12 - Wash-Out Twist Distribution of Drooped Wing Shape

The low drag benefit of the drooped wing could be explained by aeroelasticity theory which shows that the local angle of attack of an elastic wing is a function of the wing curvature and twist according to [10, 11]

$$\alpha_c = \frac{\alpha}{\cos\Lambda} - \gamma - W_x \tan\Lambda - \Theta \tag{2.15}$$

where α_c is the section or local angle of attack, α is the aircraft angle of attack, Λ is the wing sweep angle, γ is the wing pre-twist wash-out angle (positive nose-down), W_x is the wing flapwise bending deflection slope which represents the wing curvature, and Θ is the torsional deflection.

Thus with a negative wing curvature, the local angle of attack increases. This increase causes the lift coefficient C_L for the drooped wing to be higher than that for the straight wing of the benchmark aircraft. Figure 2.13 is a plot of the lift coefficient C_L versus α, which shows that indeed the C_L value for the drooped wing vehicle is larger than the C_L value for the benchmark aircraft at the same angle of attack. Thus, the computational result seems to corroborate the

observation deduced from aeroelasticity theory. This would mean that for a given C_L value at cruise, a drooped-wing aircraft would be trimmed at a lower angle of attack than the benchmark aircraft. The reduction in the angle of attack results in the drag coefficient C_D being moved closer to the minimum-drag angle of attack, which tends to be a small angle.

Another explanation for the potential drag reduction benefit of the drooped wing shape is that the negative curvature of the wing shape may effectively reduce the tendency for the high pressure flow field on the lower surface of the wing to form a flow circulation around the wing tip as a result of the low pressure region on the upper surface. Reducing tip circulation will directly result in a reduction in lift-induced drag.

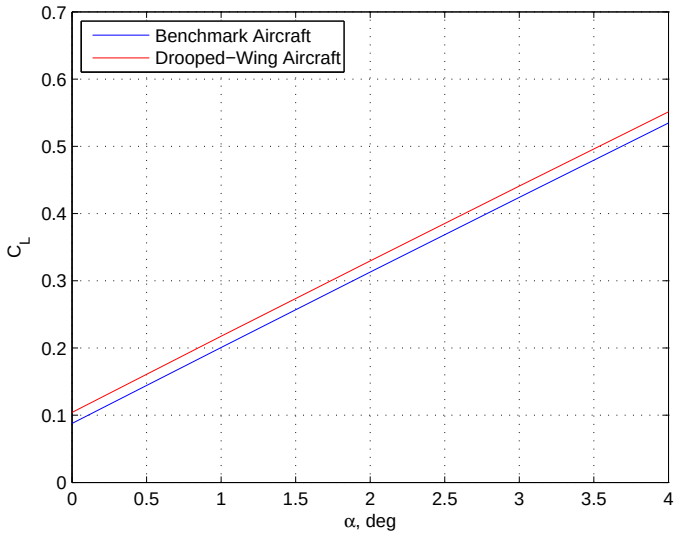

Figure 2.13 - C_L vs. α for Drooped-Wing Aircraft

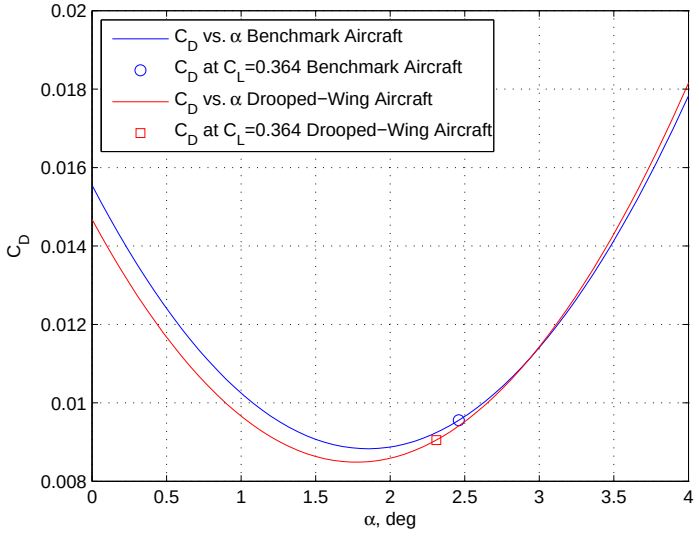

Figure 2.14 - C_D vs. α for Drooped-Wing Aircraft

Figures 2.14 and 2.15 show the drag coefficient as a function of the angle of attack and lift coefficient. As confirmed by the deduction, the C_D value for the drooped-wing aircraft concept moves closer to the minimum-drag angle of attack, thereby resulting in a lower C_D value than that for the benchmark aircraft. The C_D value for the drooped-wing

aircraft is established by $C_D = 0.00905$ as compared to $C_D = 0.00956$ for the benchmark aircraft. The overall induced drag reduction for the drooped-wing aircraft concept is 0.00051 or 5 drag counts. This represents a 5.3% reduction in the induced drag, which is considered significant.

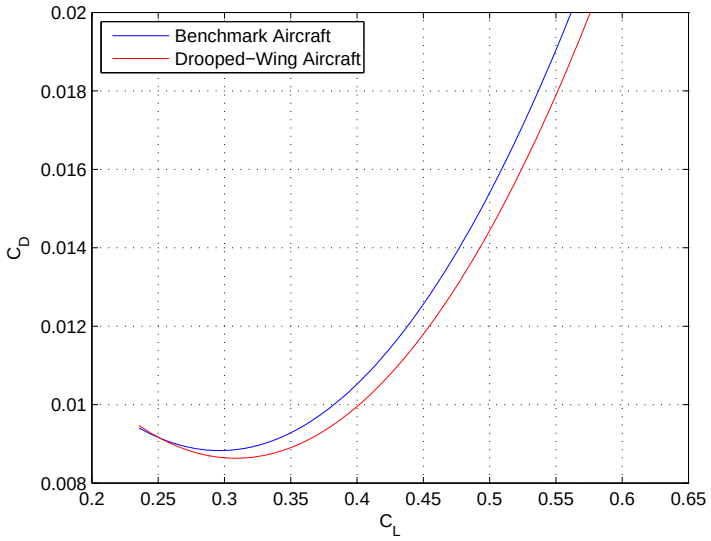

Figure 2.15 - Drag Polar for Drooped-Wing Aircraft

The sensitivity of the optimality of the drooped wing shape with the design cruise lift coefficient is also investigated. During cruise, as the fuel is burned, the aircraft weight is reduced and so is the cruise lift coefficient. For the worst case of empty fuel with 50,000 lbs of fuel expanded, the cruise lift coefficient drops to $C_L = 0.273$. An optimization cycle is performed for this design cruise lift coefficient. The results remain essentially unchanged with the same drooped wing shape being the most optimal. Thus, if the drooped-wing shape could be maintained at all times during cruise, a potential fuel saving could be realized. To maintain a constant wing shape in-flight would require an active wing shaping control system that would adjust the wing shape due to changes in the cruise condition. The active wing shape control will be further discussed.

Because the wing slope is much larger than the applied twist for the drooped-wing geometry, the effect of the wing droop tends to be more dominant than the effect of twist. For the same drooped wing shape, variations in the parameters b_i, $i = 2,3,4$ appear to have little effect on the C_D value for a small nose-up twist angle. For example, for the same drooped wing shape with $b_4 = -1.5$ and $b_3 = b_2 = 0$, the C_D value is 0.00907; and with $b_4 = b_3 = b_2 = 0$, the C_D value is 0.00912. However, there are configurations with the same drooped wing shape that produce higher C_D. For example, with $b_4 = b_3 = b_2 = -1.5$, the C_D value is 0.00974.

In addition, other drooped-wing aircraft concepts with lower wing tip deflections are also found to have lower C_D values than that for the benchmark aircraft. Figure 2.16 shows two other drooped-wing aircraft concepts and their minimum C_D values for all the configurations with the same a_i, $i = 2,3,4$.

Based on the observation above, it may be deduced that an aircraft with a negative wing curvature and proper wing twist may be aerodynamically more efficient than that with a straight horizontal wing. If this observation could be confirmed by wind tunnel testing, it could potentially be a new contribution to aeronautics.

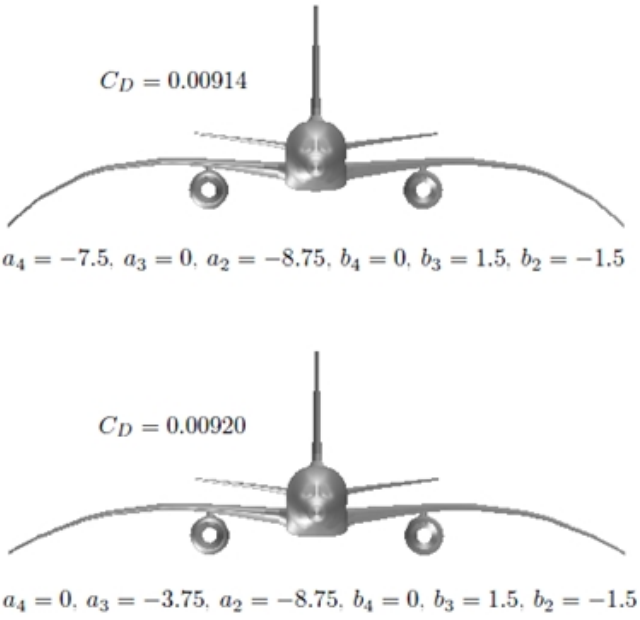

Figure 2.16 - Other Drooped-Wing Aircraft Concepts

2.5.2 Inflected Wing Shape

Since most of the low drag concepts are associated with drooped wing configurations, it is of interest in identifying a low drag concept with a positive wing curvature. The lowest drag with a positive wing tip deflection is found to be associated with a wing with a slight inflection in the mid-span. Thus, this concept is referred to as an inflected-wing aircraft as illustrated in Figure 2.17. The inflected wing shape is described by $a_4 = 7.5$, $a_3 = 3.75$, $a_2 = -8.75$, $b_4 = 1.5$, $b_3 = 1.5$, and $b_2 = -1.5$. Figures 2.18 and 2.19 show the mean line of the inflected wing shape and the wash-out twist distribution. The C_D value for this concept is $C_D = 0.00923$, which represents a 3.5% reduction. Figure 2.20 shows the drag polar of the inflected-wing aircraft concept.

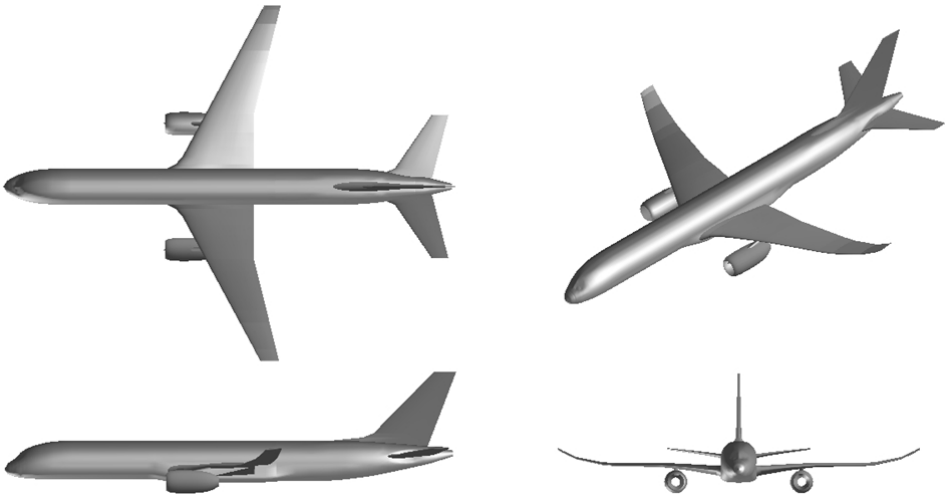

Figure 2.17 - Inflected-Wing Aircraft Concept

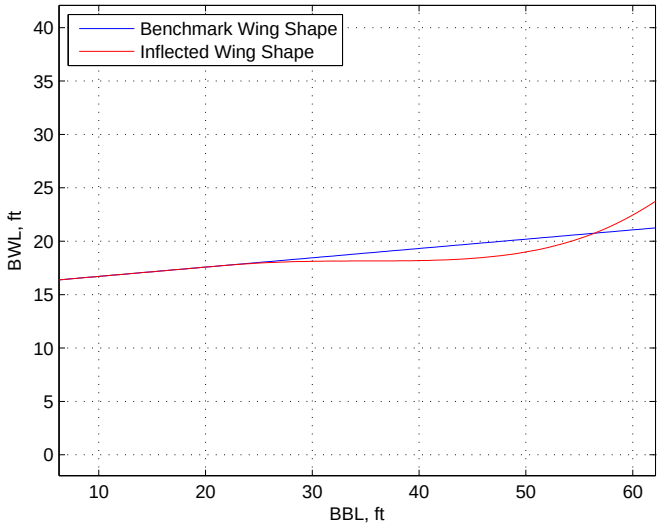

Figure 2.18 - Mean Line of Inflected Wing Shape

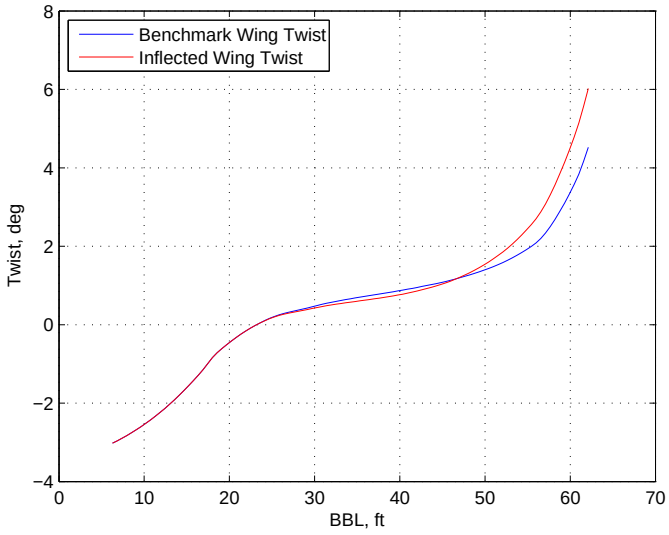

Figure 2.19 - Wash-Out Twist Distribution of Inflected Wing Shape

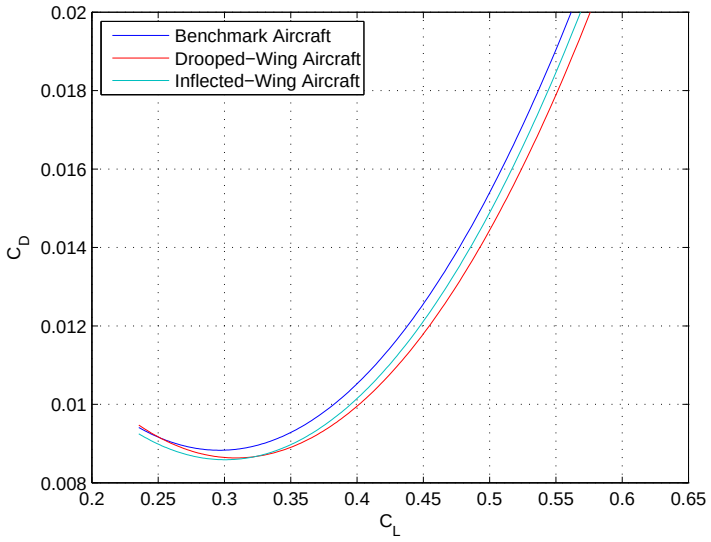

Figure 2.20 - Drag Polar for Inflected-Wing Aircraft

2.5.3 Squashed Fuselage

A typical conventional fuselage design tends to have nearly circular cross sections for passenger and cargo accommodation. Such a fuselage does not contribute significantly to the aircraft lift. As a result, the lift force is derived primarily from the aircraft wing. The squashed fuselage concept enables the fuselage to generate lift at a small positive angle of attack. Therefore, it effectively increases the lift coefficient at zero angle of attack. As a result, less lift is required from the wing and in effect the lift-induced drag is thereby reduced. A small reduction in lift can lead to a significant reduction in the induced drag, since lift and induced drag are related by a power law with a power of greater than 1.

A squashed fuselage concept is generated by scaling down the fuselage vertical dimension by a multiplier of 0.75 while scaling up the fuselage horizontal dimension by the reciprocal of the vertical dimension multiplier, so as to keep their product the same which effectively maintains the same fuselage cross sectional areas. The drooped wing is used for the squashed fuselage concept. Figure 2.21 illustrates the squashed-fuselage, drooped-wing aircraft concept.

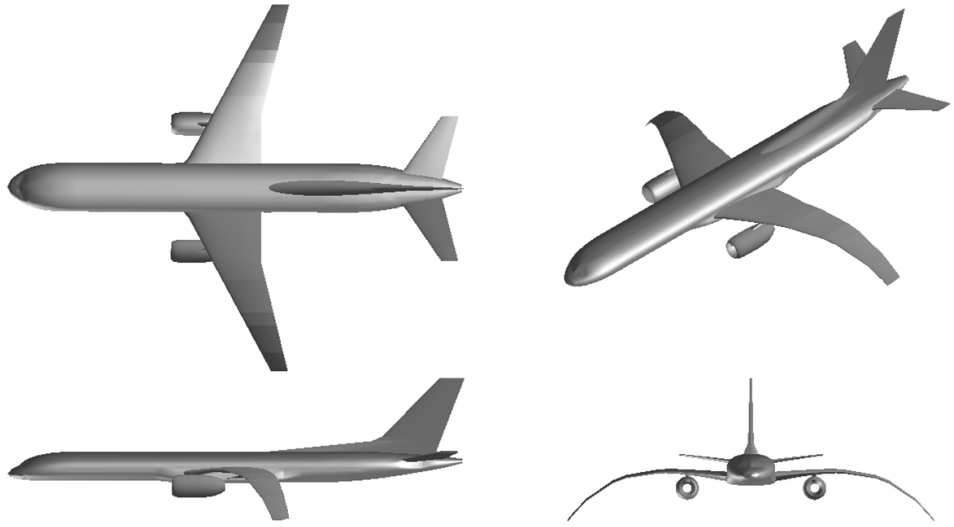

Figure 2.21 - Squashed-Fuselage Drooped-Wing Aircraft Concept

Figures 2.22, 2.23, and 2.24 are plots of C_L and C_D versus α and the drag polar for the squashed-fuselage drooped-wing aircraft concept. The small increase in lift due to fuselage lift contribution can be seen to result in a significant

induced drag reduction as shown in the drag polar. The C_L value for this aircraft concept is 0.00812 which represents more than 14 drag count or 15% reduction in the induced drag. This is a substantial increase in terms of the aerodynamic efficiency.

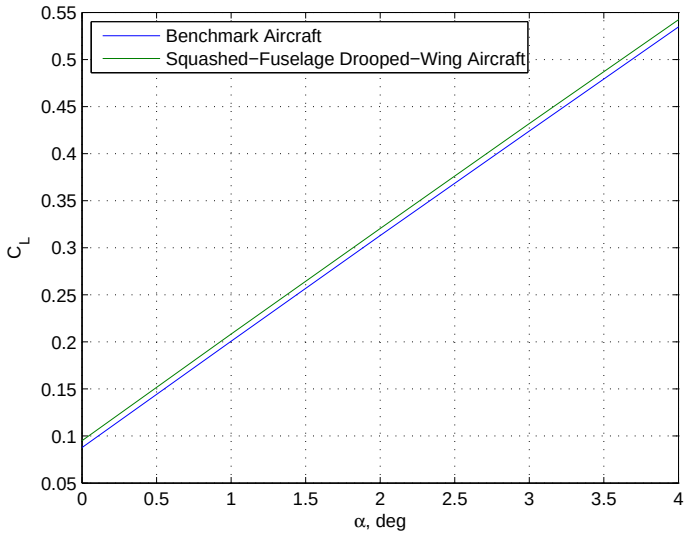

Figure 2.22 - C_L vs. α for Squashed-Fuselage Drooped-Wing Aircraft

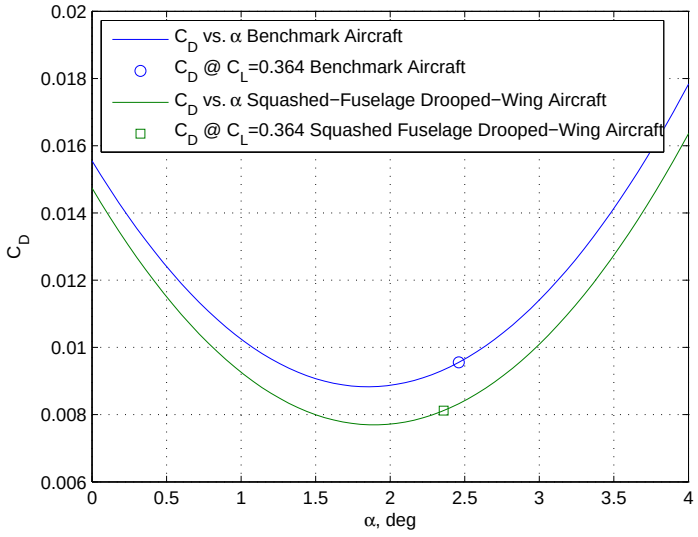

Figure 2.23 - C_D vs. α for Squashed-Fuselage Drooped-Wing Aircraft

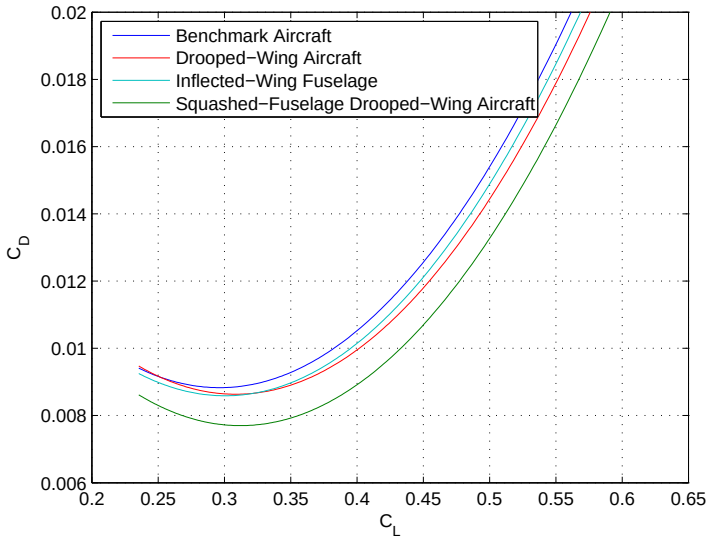

Figure 2.24 - Drag Polar for Squashed-Fuselage Drooped-Wing Aircraft

The benefit of drag reduction of the squashed fuselage concept is quite substantial, and thus it is of interest to investigate the squashed fuselage concept with the benchmark wing shape and inflected wing shape. The results show that the squashed fuselage provides almost the same relative drag reduction over the benchmark aircraft and the inflected-wing aircraft. In particular, the C_L value for the squashed-fuselage benchmark-wing aircraft is 0.00858 and the C_L value for the squashed-fuselage inflected-wing aircraft is 0.00825.

The outcome of this study shows that, from an implementation perspective, the squashed fuselage concept has a potential big pay-off since the concept can be easily implemented without a major change in the manufacturing process.

2.6 Preliminary CFD Verification with Cart3D

In order to check the potential induced drag benefits of some of the new concepts identified by the optimization, NASA's Cart3D simulation package was used in conjunction with adjoint-based mesh adaptation to verify the drooped-wing and inflected-wing aircraft concepts. Cart3D is a high-fidelity inviscid (Euler) analysis package targeted at analyzing aircraft performance in conceptual and preliminary aerodynamic design. The adjoint-based mesh refinement module, used in this study, makes use of adjoint-weighted residual error-estimates to drive mesh adaptation in order to eradicate discretization error in the numerical solution ensuring accurate estimates of integrated forces such as lift or drag.

2.6.1 Comparison with VORVIEW and Wind Tunnel

Previously, both VORVIEW and Cart3D had been used to model the GTM geometry with various damages to aerodynamic surfaces for the NASA Damage Adaptive Control System (DACS) project under the NASA Aviation Safety and Security program in 2005 [3]. Wind tunnel data for the 5.5% model of the GTM were obtained in the 14-by 22-foot low speed subsonic wind tunnel at NASA Langley. The test section Mach number is fixed at 0.084 which is well within the incompressible flow regime. Force and moment data were collected over a wide range of angle of attack and angle of sideslip. Computational results from VORVIEW and Cart3D were subsequently compared with wind tunnel data to assess relative accuracy of the aerodynamic prediction. Due to a convergence issue with Cart3D which caused a substantial difference with the wind tunnel data, the Mach number for Cart3D was increased to 0.2 to improve the solution convergence while VORVIEW results were for Mach number of 0.084. Figures 2.25 and 2.26 shows the comparison of the C_L and C_D values versus the angle of attack at zero sideslip angle [3].

VORVIEW lift prediction matched wind tunnel data very well up to almost $\alpha = 10^o$. Cart3D seemed to overpredict the lift coefficient. However, this could be due to Cart3D results computed for a higher Mach number than both VORVIEW results and wind tunnel data. Both VORVIEW and Cart3D produced a very similar drag prediction, but

they were lower than the measured drag in the wind tunnel. The measured drag in the wind tunnel is not corrected for a full-scale Reynold number at cruise. When a Reynolds number correction is applied, the C_D coefficient should decrease in theory as the Reynolds number increases. The discrepancy could also arise from the lack of viscous loss models in both VORVIEW and Cart3D results. Nonetheless, both of these aerodynamic codes seem to have similar predictive capabilities when compressibility is not a factor. In compressible simulations, Cart3D is expected to be substantially more accurate since the vortex panel method used by VORVIEW cannot account for compressibility effects (e.g. shock formation and wave-drag) within the flow.

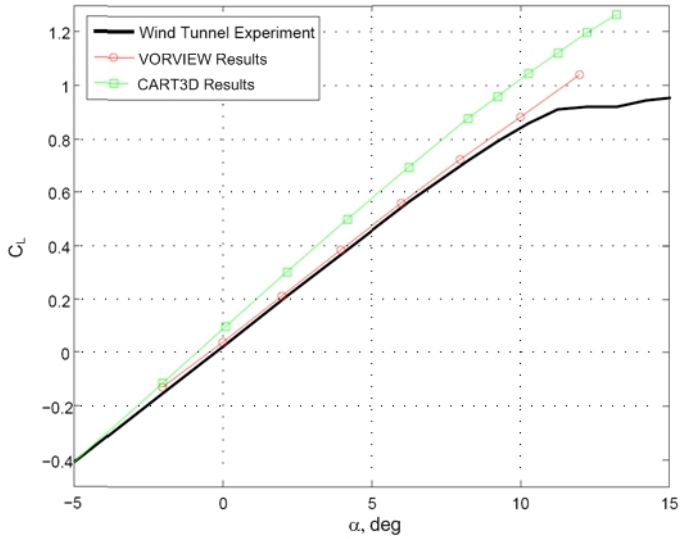

Figure 2.25 - C_L vs. α Comparison

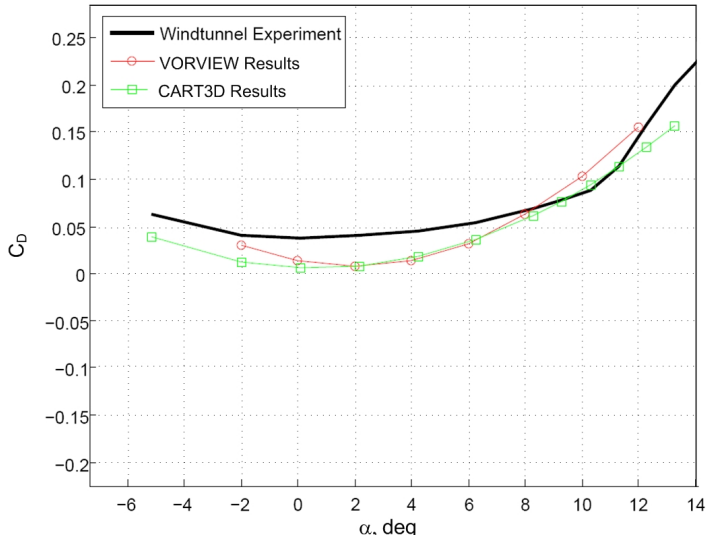

Figure 2.26 - C_D vs. α Comparison

2.6.2 Geometry and Mesh Generation

The geometry used for this study is a scaled-up version of a 5.5 % model of the GTM obtained from NASA Langley. A ProE assembly of all the parts was provided which was then converted to a water-tight CFD quality triangulation by triangulating each part individually and then intersecting. This is the same baseline triangulation used in previous

work [3]. Once this water-tight geometry has been created, Cart3D automatically generates an initial Cartesian volume mesh around the triangulation. Cart3D then refines this initial coarse mesh in a manner described in the next section. A user-prescribed input in Cart3D is the aspect ratio of the volume cells. With the flow primarily along the chordwise direction of the wing, there is no need for the same resolution in the spanwise direction. Hence, present computations use a cell aspect ratio of about two in the spanwise direction.

2.6.3 Flow Solver

Cart3D is a three-dimensional Euler solver suitable for CFD analysis of complex geometries. Cart3D has a mesh adaptation feature that uses adjoint-weighted residual error estimates to drive mesh adaptation for user selected outputs (such as drag or lift). In this way, the mesh refinement procedure generates a mesh that reduces the discretization errors in the outputs so that the influence of these errors on the output functional is below a specified error tolerance. A more complete analysis of the adjoint formulation and its applications on complex geometries can be found in [6] and [7]. For the current study, 12 mesh adaptation cycles were used. One complete mesh adapted flow solution took on average 7 hours on 64 CPUs of the Columbia supercomputer. Another valuable capability of Cart3D, which is used in the current study, is the ability to achieve a user-requested C_L value by modifying the angle of attack at specified time steps. This capability is helpful in comparing induced-drag benefits across different geometries. A C_L value of 0.6 is chosen for the current study as this results in the best convergence of drag. For a lower C_L value such as the design cruise C_L value of 0.364, there could be an issue with a solution convergence.

2.6.4 Wing Bending Implementation

In order to properly model the deformation of the benchmark aircraft wings, a program was written to manipulate the triangulation. This program reads in the benchmark aircraft configuration, applies a given twist angle about a pre-computed centroidal axis for the wings prescribed by the twist shape function in Eq. (2.10), deflects the wing in the normal direction according to the bending shape function prescribed by Eq. (2.11), and then outputs a final water-tight, CFD quality triangulation. Both twist and bending deflection are applied outboard of the engine pylons on both wings. The exact location is at a spanwise location of 22.12 ft (BBL 22.12 ft) from the aircraft x- axis. The location between this engine pylon location and the wing tip is normalized such that $u = 0$ at the pylon and $u = 1$ at the wing tip, where $u = (y_V - y_t) / (y_t - y_e)$ is the normalized coordinate along the wing span. This can be seen in Figure 2.27.

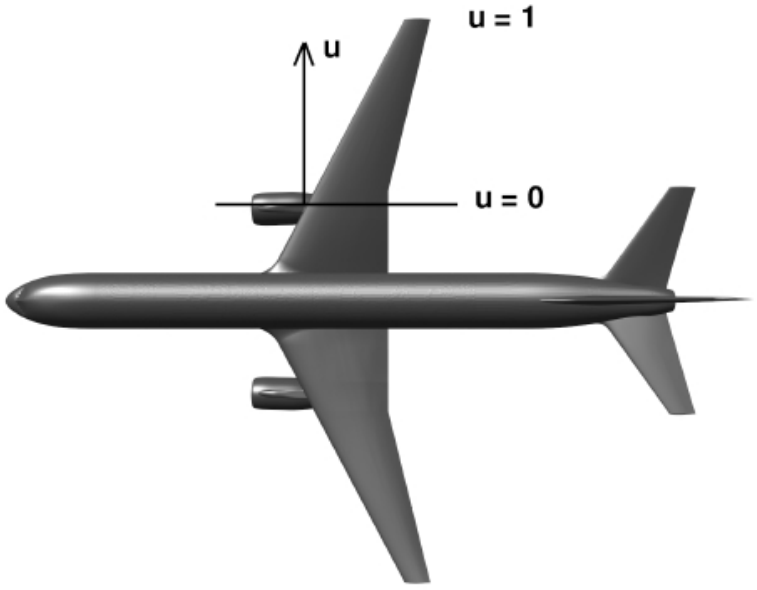

Figure 2.27 - Shape Function Schematic

The deformed geometries (under the prescribed bending deflection, no twist) are shown in Figure 2.28. The drooped wing and inflected wing geometries were found to be optimal in terms of induced-drag reduction using

VORVIEW. All of the cases for the current study were examined with bending deflection only. Future studies will include both bending deflection and twist.

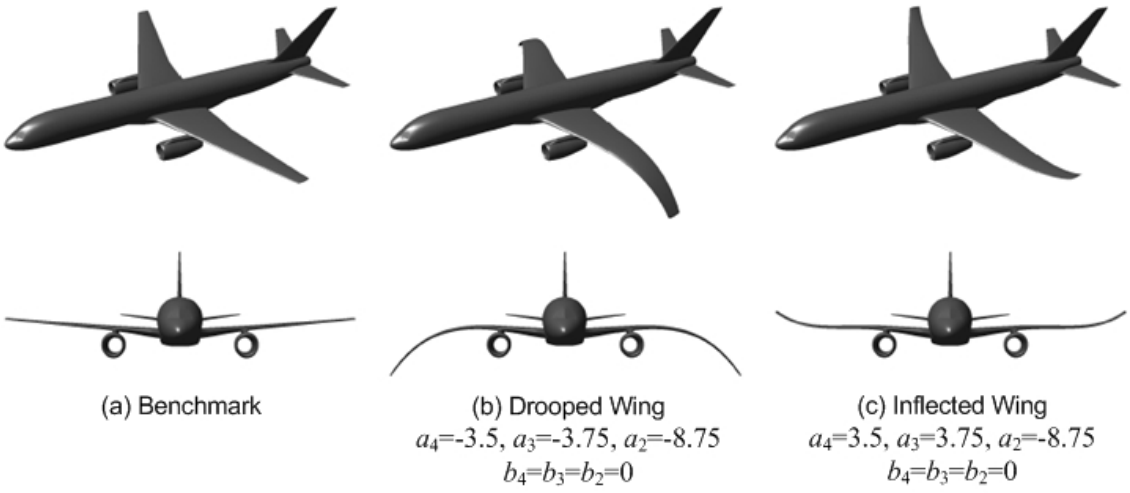

Figure 2.28 - Deformed Geometries under Prescribed Bending Deflection (no Twist)

The functional used to drive mesh adaptation is given by

$$J = 0.01C_L + C_D \tag{2.16}$$

Since the main goal of the study is to capture the induced drag of the wings, and because the C_L value is much greater than the C_D value, therefore converges faster than drag, a heavier weighting is given to the drag coefficient.

2.6.5 Results

The following cases were run at a Mach number of 0.3 for verification with VORVIEW. Figures 2.29 and 2.30 display Mach contours and surface pressures of the three aircraft configurations. The Mach number near the wing tip of the drooped-wing aircraft appears lower than the Mach number for both the benchmark aircraft and inflected-wing aircraft which seem to have a similar Mach number distribution. The pressure distribution over the upper surface of the wings for the three configurations appears to be quite similar, although there is a stronger low pressure region at the wing leading edge in the benchmark aircraft. This could translate into a faster localized flow field in the leading edge region that might result in shock-induced separation at higher Mach number. Figure 31 is the convergence plot for the functional and error convergence.

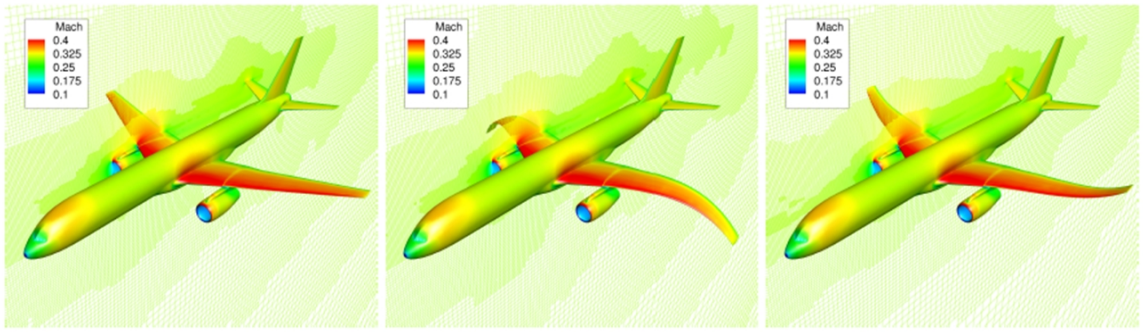

Figure 2.29 - Mach Contours

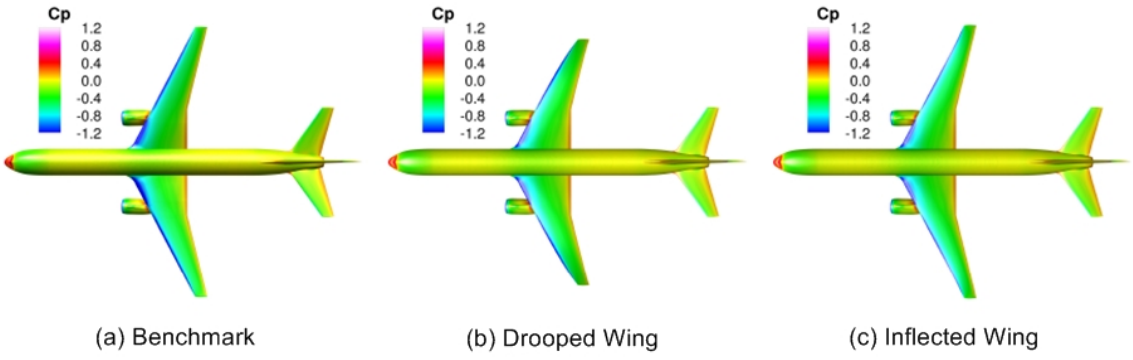

Figure 2.30 - Surface c_p Contours

Table 2.4 below summarizes the Cart3D results for the three aircraft configurations. The parameter e in the table represents the span efficiency factor for the wings, where $e = C_L^2/(\pi ARC_D)$ is 1 for the ideal elliptical lift distribution. Based on these results, it appears that the inflected-wing aircraft configuration provides a better benefit in terms of induced-drag reduction. The inflected-wing configuration yields a 2.3 % improvement over the benchmark aircraft configuration in span efficiency and a 2.0 % reduction in drag. The drooped-wing aircraft configuration, however, does not appear to provide any improvement. This could be due to not having the prescribed twists applied in the geometries since the twist can potentially affect the local angle of attack on a wing section.

	α, deg	C_L	C_D	e
Benchmark	4.94	0.6	0.0224	0.731
Drooped Wing	5.15	0.6	0.0224	0.733
Inflected Wing	4.92	0.6	0.0220	0.748

Table 2.4 - Drag Reduction at Mach 0.3

For comparison, VORVIEW results for $C_L = 0.6$ for the drooped-wing and inflected-wing aircraft configurations are computed. The results are from the optimal configurations with twists incorporated, so they might not give a direct comparison. Table 2.5 shows the drag comparison among the three aircraft configurations. The relative benefits of the induced drag reduction for the drooped-wing and inflected-wing aircraft configurations remain about the same as the optimization results.

	α, deg	C_L	C_D	e
Benchmark	4.50	0.6	0.0235	0.696
Drooped Wing	4.45	0.6	0.0224	0.731
Inflected Wing	4.51	0.6	0.0229	0.716

Table 2.5 - Drag Reduction at Mach 0.8

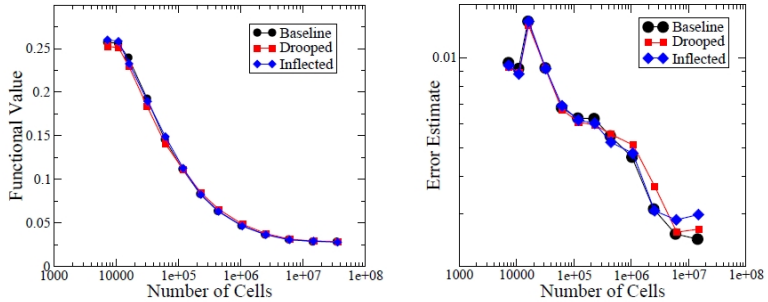

(a) Functional Convergence (b) Error Convergence

Figure 2.31 - Functional and Error Convergence

In summary, the inflected wing geometry shows a beneficial effect; however, potential does exist for the drooped wing case as well. If the wing tip bending deflection was incorporated with wing twist so that the same lift could be achieved at a lower angle of attack, the drooped wing geometry could provide a larger benefit. In any case, no definitive conclusion could be made in regards to the merits of the drooped-wing and inflected-wing aircraft configurations at this point since the validation effort is very limited in scope due to the time and resource constraints. Given that these concepts could be potentially beneficial for induced drag reduction, a further follow-on effort should be considered to conduct a more thorough analysis that includes the effect of the optimal wing twists which are neglected in this study.

3 Elastic Wing Shaping Control Actuation

Based on the optimization results, the drooped-wing aircraft concept is selected for the active wing shaping control design since it provides the best induced drag reduction. Since the optimal wing shape is not sensitive to changes in the cruise lift coefficient, to maintain the best cruise efficiency, the wing shape would need to be actively controlled. A concept of operation is now defined as follows:

- The design point for wing shaping control actuator requirements is defined to be at the half way point of cruise at 30,000 ft corresponding to an aircraft weight of 175,000 lbs with 50% fuel in the tank.
- The active wing shaping control actuator will be a series of leading edge slats and trailing edge flaps.
- The wing shape at the design point corresponds to the optimal drooped-wing shape. This would mean that the as-built wing shape would be the optimal drooped wing shape minus the differential bending and torsional deflections at 1-g loading at the design point. Under the 1-g loading at cruise, the wing shape is aerodynamically loaded and deflected into the optimal drooped-wing shape with no flap or slat deflection.
- At the start of cruise, the aircraft weight is 190,000 lbs with 80% fuel in the tank. This would correspond to a higher wing loading that causes the wing shape to move up from the optimal drooped wing shape. Active wing shaping control flaps and slats are deployed to bring the wing shape back to the optimal drooped wing shape. This would result in a lower wing loading that would cause the aircraft to decrease in altitude.
- At the end of cruise, the aircraft weight is 160,000 lbs with 20% fuel in the tank. This would correspond to a lower wing loading that causes the wing shape to move down from the optimal drooped wing shape. Active wing shaping control flaps and slats are deployed to bring the wing shape back to the optimal drooped wing shape. This would result in a higher wing loading that would cause the aircraft to increase in altitude.

Two wing shaping control actuator concepts are considered in the study: a conventional flap concept and a novel variable camber continuous flap concept. Boeing, in partnership with NASA, has contributed their system-level expertise and participated in the development of wing shaping actuation concepts

3.1 Baseline Flap and Slat Layout

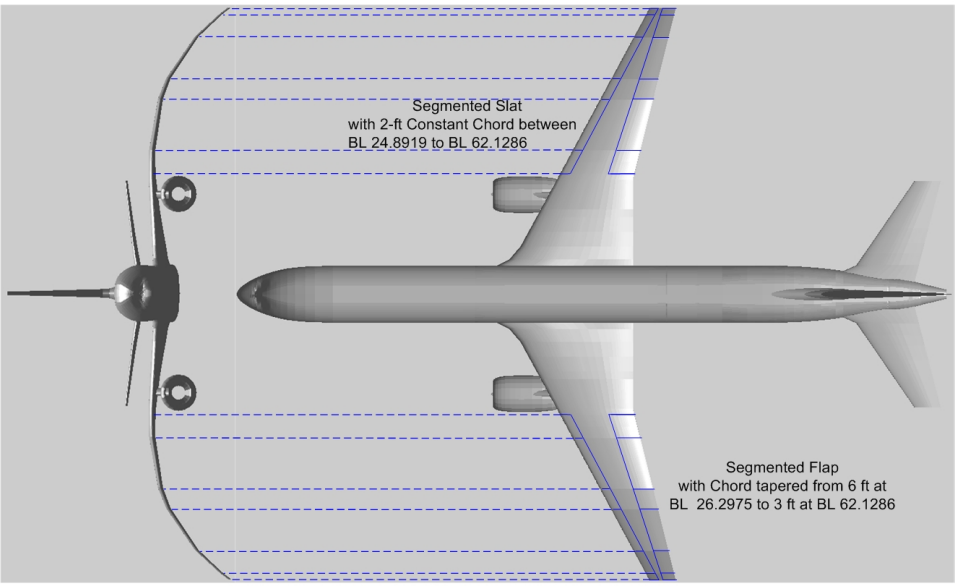

Figure 3.1 - Conventional Flap System

The baseline flap and slat systems for active wing shaping control are based on a conventional simple flap design. A proposed flap and slat layout is as shown in Figure 3.1. There are 6 flaps and slats on each wing that can be

actuated independently to provide necessary control forces and moments to actively shape the aircraft wings. They are numbered from 1 to 6 from outboard to inboard. The outboard flaps can be configured as ailerons for roll control as needed. The slats have constant chords of 2 ft that span from the BBL 26.2975 ft to BBL 62.1286 ft. The flaps have linearly tapered chords from 6 ft at BBL 24.8919 ft to 3 ft at BBL 62.1286 ft. The flap drive systems are sized to provide sufficient flap deflection travel and be fast enough for feedback control.

3.2 Flap and Slat Deflection Requirements

The flap and slat systems must be able to provide sufficient aeroelastic forces and moments to change the wing shape in-flight. The flap and slat deflections therefore are proportional to the aeroelastic deflections between the optimal drooped wing shape and the operating wing shape. The requirements for the flap and slat deflections can be established by the differences between the wing shapes at the start and end of cruise and the optimal drooped wing shape at the half way point of cruise. To estimate the flap and slat deflections, a static aeroelastic analysis is conducted to compute the generalized aeroelastic stiffness and the generalized deflection of the wing shapes in bending and torsion, and the generalized force derivative for the flaps and slats. The aeroelastic analysis is described in detail later in the report.

Using a pseudo-inverse method, the flap and slat deflections can be computed from Eq. (5.57) derived later in the report as:

$$f = RG^\top \left(GRG^\top\right)^{-1} (K_d \delta_d - K\delta) \tag{3.1}$$

where $f = \begin{bmatrix} f_1 & f_2 & \dots & f_6 & s_1 & s_2 & \dots & s_6 \end{bmatrix}^\top$ are the flap and slat deflections, $\delta = \begin{bmatrix} w & \theta \end{bmatrix}^\top$ is the generalized aeroelastic deflections in bending and torsion, δ_d is the generalized aeroelastic deflections at the half way point of cruise, K and K_d are the generalized stiffness in bending and torsion, G is the generalized force derivative for the flaps and slats, and $R > 0$ is a positive-definite weighting matrix.

Numerically, these quantities are computed to be

$$x_d = \begin{bmatrix} 1.5277 \\ -0.0272 \end{bmatrix} \quad x_s = \begin{bmatrix} 1.6290 \\ -0.0311 \end{bmatrix} \quad x_e = \begin{bmatrix} 1.4260 \\ -0.0233 \end{bmatrix}$$

$$K_d = 10^6 \begin{bmatrix} 0.0209 & 0.9378 \\ -0.0611 & 3.0680 \end{bmatrix} \quad K_s = 10^6 \begin{bmatrix} 0.0209 & 0.9360 \\ -0.0610 & 3.0743 \end{bmatrix} \quad K_e = 10^6 \begin{bmatrix} 0.0210 & 0.9397 \\ -0.0612 & 3.0616 \end{bmatrix}$$

$$G_s = 10^5 \begin{bmatrix} 0.0012 & 0.0249 & 0.1601 & 0.0269 & 0.2790 & 0.0298 & -0.0002 & 0.0249 & 0.1601 & 0.0269 & 0.2790 & 0.0298 \\ -0.0012 & -0.0334 & -0.3258 & -0.0787 & -1.2337 & -0.2137 & 0.0002 & 0.0044 & 0.0206 & 0.0062 & 0.0251 & 0.0061 \end{bmatrix}$$

$$G_e = 10^5 \begin{bmatrix} 0.0013 & 0.0253 & 0.1609 & 0.0269 & 0.2808 & 0.0304 & -0.0002 & 0.0253 & 0.1609 & 0.0269 & 0.2808 & 0.0304 \\ -0.0014 & -0.0339 & -0.3275 & -0.0787 & -1.2415 & -0.2184 & 0.0002 & 0.0044 & 0.0206 & 0.0062 & 0.0250 & 0.0039 \end{bmatrix}$$

where the subscripts s and e denote the start and end of cruise, respectively.

Note that the actual deflections can be computed by multiplying the generalized deflections by the first bending (1B) and first torsion (1T) normalized mode shapes. For these mode shapes, the bending and torsional deflections at the wing tip are 2 and $\sqrt{2}$, respectively. Thus the actual deflections at the wing tip are

$$\begin{bmatrix} W(y_t) \\ \Theta(y_t) \end{bmatrix}_d = \begin{bmatrix} 3.0554 \\ -0.0385 \end{bmatrix} \quad \begin{bmatrix} W(y_t) \\ \Theta(y_t) \end{bmatrix}_s = \begin{bmatrix} 3.2581 \\ -0.0440 \end{bmatrix} \quad \begin{bmatrix} W(y_t) \\ \Theta(y_t) \end{bmatrix}_e = \begin{bmatrix} 2.8519 \\ -0.0330 \end{bmatrix}$$

where W is in feet and Θ is in radians.

There are multiple solutions of the flap and slat deflections. One thing to note is that the flaps and slats will incur a drag penalty as they are used to control the wing shape to reduce the induced drag. If the flap and slat deflections are too large, there would be a significant drag penalty associated with the flap and slat deflections. Thus, to minimize

the drag penalty, an optimization method is used to find the flap and slat deflection requirements that minimize the following cost functional:

$$J = \left| C_{D_f} \right| |f| \tag{3.2}$$

where C_{D_f} is the drag derivative due to the flap and slat deflections which are computed in VORVIEW at zero flap and slat deflection to be

$$C_{D_f} = \begin{bmatrix} 0.0009 & 0.0044 & 0.0159 & 0.0097 & 0.0185 & 0.0107 \\ & & & & 0.0002 & 0.0004 & -0.0024 & -0.0025 & 0.0012 & 0.0085 \end{bmatrix}$$

To optimize the deflection requirements, the weighting matrix R is adjusted randomly to seek a minimum value of the cost functional J. Tables 3.1 and 3.2 show the flap and slat deflection requirements as computed from the optimization.

	1	2	3	4	5	6
Flap, deg	0.0270	0.2402	5.2260	0.0226	-9.5552	-0.0467
Slat, deg	-0.0027	0.7553	7.6052	2.5670	4.6545	3.2970

Table 3.1 - Flap and Slat Deflection Requirements at Start of Cruise

	1	2	3	4	5	6
Flap, deg	-0.0301	-0.2412	-5.2001	-0.0225	9.5031	0.0472
Slat, deg	0.0026	-0.7576	-7.5604	-2.5392	-4.6332	-3.2568

Table 3.2 - Flap and Slat Deflection Requirements at End of Cruise

The minimum incremental C_D values due to the deflections are 0.00189 at the start of cruise and 0.00188 at the end of cruise. It should be noted that the minimum incremental C_D estimates are non-conservative using the drag derivative at zero deflection. As a check, these flap deflections are incorporated in VORVIEW for drag estimation. The VORVIEW results indicated that the incremental C_D values are 0.00630 at the start of cruise and 0.00437 at the end of cruise. These incremental C_D values are much larger than those estimated using the drag derivative. Thus, the drag penalty of the conventional flap system is substantial.

It is noted that flap 1, 2, 4, and 6, and slat 1 are not very active. Thus, this suggests a possibility for a better flap and slat layout that could reduce the numbers of flaps and slats.

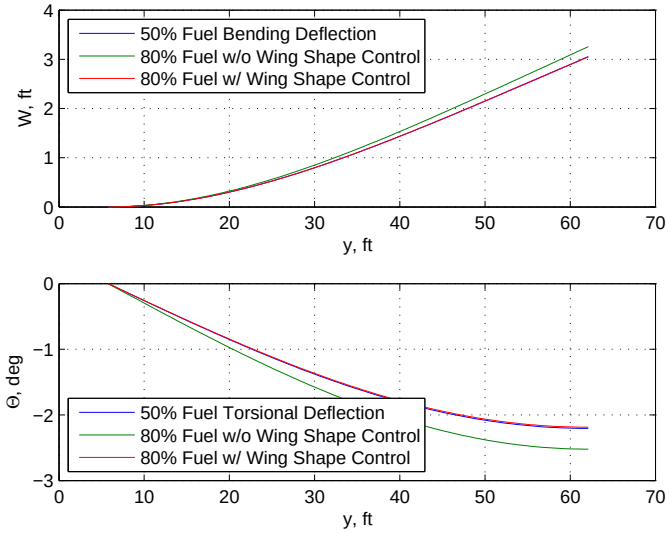

Figure 3.2 - Wing Deflections at Start of Cruise

A better estimation would require an iterative process by using the flap estimates to compute the new drag values in VORVIEW iteratively in the optimization. Currently, this capability is not available and therefore should be considered as a future follow-on effort. It is noted that even the best effort in minimizing the drag penalty may not improve the situation much if the aerodynamic losses due to the conventional flap system are too great to overcome. This realization leads to the development of a novel continuous trailing edge flap concept which will be presented subsequently.

Figures 3.2 and 3.3 show the bending and torsional deflections with and without active wing shaping control. The differences between the deflections at the start and end of cruise and the deflection for the optimal drooped wing shape represent the actual wing deflections since the as-built drooped wing already accounts for the 1-g deflection.

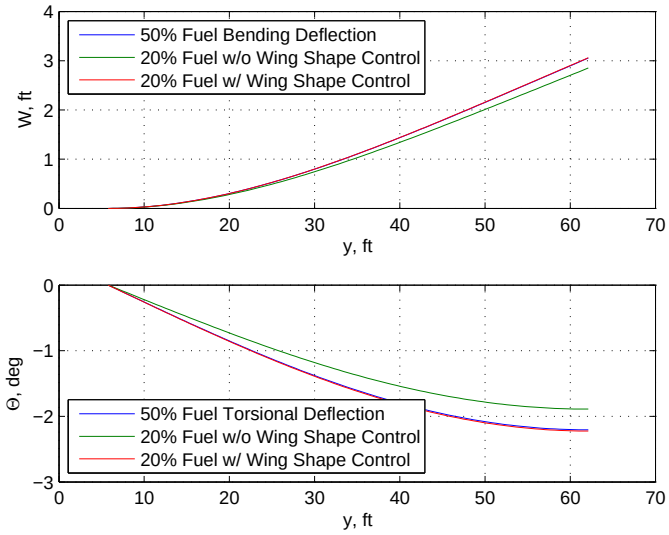

Figure 3.3 - Wing Deflections at End of Cruise

3.3 Actuation System Development

Boeing, in partnership with NASA, has used the baseline configuration shown in Figure 3.1, as well as MATLAB® data files provided by NASA Ames, to develop an analysis of actuation loads to maintain the NASA droop-wing shaping. All analysis was conducted for a cruise condition of 0.8M and 30K ft. altitude. The actuation shall operate within the cruise condition, maintaining the same full droop wing configuration during weight change due to fuel burn starting at an 80% fuel status to as low as 20% fuel remaining. At a 50% fuel state the wing actuation will be at a null position, meaning that this would be the most efficient corresponding to the optimal drooped wing configuration for minimum drag.

This condition was used as the basis of analysis for sizing of Electro-Mechanical Actuators (EMAs) as the primary form of flight control actuators addressed by this study, in order to develop indicators of other key flight control actuation parameters such as weight, volume, hinge moments and stall torque requirements, etc.

Many other factors (a short list is provided below) will weigh in to a more detailed analysis from which a fully compliant aircraft production design flight control actuation system can be achieved:

- Loads and rate consideration during:
  - Maneuvering in cruise conditions
  - Takeoff and landing configuration and control requirements
- Bandwidth and frequency response requirements due to structural mode dynamics
- Geometric constraints imposed by a final configuration and inter-surface separation requirements
- Trade-offs between weight and power which can lead to hybrid actuation configurations, including both electrical and hydraulic solutions, as a better fit

- Reliability requirements
- Maintainability requirements

The goal of this first phase analysis was to determine preliminary design requirement parameters that would support a flight control actuation system providing the required wing shape throughout the cruise flight envelope. This analysis also describes how this actuation system can practically be constructed using size, weight and power that would be achievable, either within today's available technology or near term developmental electric actuation technology.

3.3.1 Actuation System Analysis

The geometry provided by NASA Ames to Boeing's Research and Technology group was chosen to define the droop wing configuration and the wing control surface layout as shown in Figure 3.1 and provided as a part of Table 3.3 following. This geometry, as well as static condition data files provided, include the following features for control surface actuation:

- 6 Trailing Edge Flaps of tapered Chord from 6 ft. at BL 24.8919 to 2 ft. at BL 62.1286 (Each Wing)
- 6 Leading Edge Slats w/ 2 ft. Constant Chord between BL 24.8919 through BL 62.1286 (Each Wing)
- *y* span dimensions of all Flap and Slat geometry
- Full Chord dimensions of wing sections
- Aero. for flight conditions at 0.8M and 30K ft

Boeing, in turn, used these properties and dimensions, to derive the lift distribution curves as well as torsion moment distribution for the full *y* span dimension. From these distributions and properties chord ratios of the flap and slat surfaces were used to apply the lifting load distribution to the six individual flap and slat areas at their center of pressure chord points to develop loading for each actuation pairing.

From this loading and using a typical moment arm encountered in flight control for each flap and slat within a wing-type like the GTM model, a total actuation force requirement for each surface was developed. Using this force, an individual force requirement for the actuator pair's single actuator was obtained. Figure 3.4 is a model of the moment relationships used to calculate the actuation relationships in terms of generally accepted principles for actuator sizing.

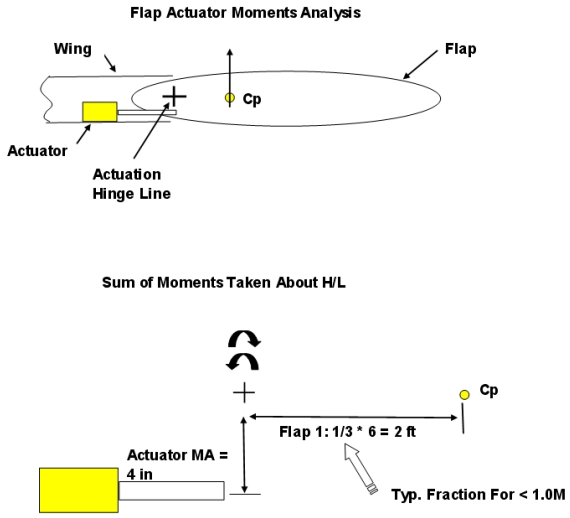

Figure 3.4 - Actuator Moment Relationships (Boeing Research and Technology)

Control Effectors for Maintaining Optimum Wing Shape
For The NASA Droop Configuration

Configuration Requirement:

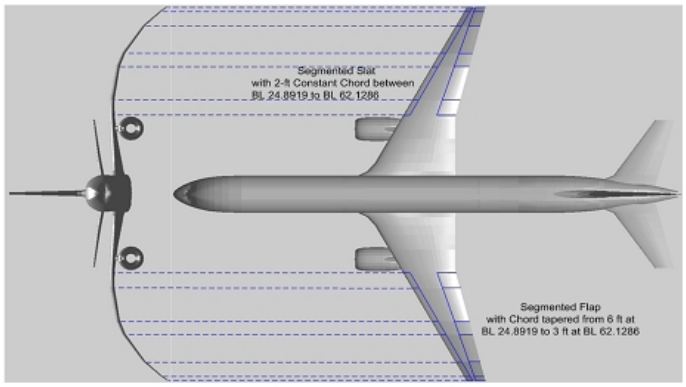

Wing Station (y)	Units	Flap 1	Flap 2	Flap 3	Flap 4	Flap 5	Flap 6
(y) for Cp	Start	31.2052	42.2216	46.7028	55.7581	60.6115	62.1860
	End	24.8919	31.2052	42.2216	46.7028	55.7581	60.6115
(y) span midpt f,s	Ft	28.0486	36.7134	44.4622	51.2305	58.1848	61.3988
	Length	6.3133	11.0164	4.4812	9.0553	4.8534	1.5745
Chord	Start	16.5998	14.7464	11.5265	10.2165	7.5689	6.1840
	End	14.7464	11.5265	10.2165	7.5689	6.1840	5.7041
Chord Midpt (Total)	Ft	15.6731	13.1365	10.8715	8.8927	6.8765	5.9441
FLAP ANALYSIS: (Unsigned)							
80% FUEL CASE							
Flap Deflection (f)	Deg	-8.4657	-8.2779	-0.2916	-6.3313	-0.3388	-0.0133
Length	Ft	15.6731	13.1365	10.8715	8.8927	6.8765	5.9441
Width	Ft	6.0000	5.0000	5.0000	4.0000	4.0000	3.0000
Area	Ft^2	37.8798	55.0820	22.4060	36.2212	19.4136	4.7235
Est.Flap Contrib. L							
Chord Midpt (Total)	Ft	0.0000	0.0000	0.0000	0.0000	0.0000	0.0000
Chord Flap Ratio	%	0.3828	0.3806	0.4599	0.4498	0.5817	0.5047
Lift Distribution at Cp	lbsf	8970.9000	15046.0000	3888.3000	5343.1000	1324.1000	43.5220
Flap Contr.	lbsf	3434.2536	5726.8136	1788.2997	2403.3646	770.2230	21.9658
Actuation Force Est.							
Cp MA	In	20.0000	20.0000	20.0000	20.0000	20.0000	20.0000
Flap Moment	in-lbsf	68685.0719	114536.2712	35765.9937	48067.2911	15404.4602	439.3166
Actuator MA	In	4.0000	4.0000	4.0000	4.0000	2.0000	2.0000
Total Force (f)	lbsf	17171.2680	28634.0678	8941.4984	12016.8228	7702.2301	219.6583
Actuator Qty		2.0000	2.0000	2.0000	2.0000	2.0000	2.0000
Per Actuator Force	lbsf	8585.6340	14317.0339	4470.7492	6008.4114	3851.1150	109.8292
20% FUEL CASE							
Flap Deflection (f)	Deg	8.4446	8.2573	0.2911	6.3176	0.3382	0.0133
Length	Ft	15.6731	13.1365	10.8715	8.8927	6.8765	5.9441
Actuation Force Est.							
Actuator Qty		2.0000	2.0000	2.0000	2.0000	2.0000	2.0000
Per Actuator Force	lbsf	858.5634	1718.0441	536.4899	901.2617	288.8336	10.9829

Table 3.3 - Design Data for Wing Flaps (Boeing Research and Technology)

Note: Flap & Slat 1 (Inboard) . . . Flap & Slat 6 (Wing Tip)

Control Effectors for Maintaining Optimum Wing Shape
For The NASA Droop Configuration

SLAT ANALYSIS: (Unsigned)		Slat 1	Slat 2	Slat 3	Slat 4	Slat 5	Slat 6
80% FUEL CASE							
Slat Deflection (*s*)	Deg	1.1338	14.0560	1.8102	5.2352	0.1040	0.0002
Est.Slat Contrib. L							
Chord Midpt (Total)	Ft	0.0000	0.0000	0.0000	0.0000	0.0000	0.0000
Chord Slat Ratio	%	0.1276	0.1522	0.1840	0.2249	0.2908	0.3365
Lift Distribution at Cp	lbsf	8970.9000	15046.0000	3888.3000	5343.1000	1324.1000	43.5220
Slat Contr.	lbsf	1144.7512	2290.7254	715.3199	1201.6823	385.1115	14.6439
Actuation Force Est.							
Total Force (*s*)	lbsf	1717.1268	3436.0881	1072.9798	1802.5234	577.6673	21.9658
Actuator Qty		2.0000	2.0000	2.0000	2.0000	2.0000	2.0000
Per Actuator Force	lbsf	858.5634	1718.0441	536.4899	901.2617	288.8336	10.9829
20% FUEL CASE							
Slat Deflection (*s*)	Deg	-1.1315	-14.0560	-1.8088	-5.2232	-0.1037	-0.0002
Est.Slat Contrib. L							
Chord Midpt (Total)	Ft	0.0000	0.0000	0.0000	0.0000	0.0000	0.0000
Lift Distribution at Cp	lbsf	8970.9000	15046.0000	3888.3000	5343.1000	1324.1000	43.5220
Slat Contr.	lbsf	1144.7512	2290.7254	715.3199	1201.6823	385.1115	14.6439
Actuation Force Est.							
Total Force (*s*)	lbsf	1717.1268	3436.0881	1072.9798	1802.5234	577.6673	21.9658
Actuator Qty		2.0000	2.0000	2.0000	2.0000	2.0000	2.0000
Per Actuator Force	lbsf	858.5634	1718.0441	536.4899	901.2617	288.8336	10.9829

Table 3.3 (Cont) - Design Data for Wing Flaps (Boeing Research and Technology)

Note: Flap & Slat 1 (Inboard) . . . Flap & Slat 6 (Wing Tip)

This procedure can be extended in the case of each flap (and slat), using the moments about the hinge line shown with some radius (values of radius are approximately as shown in Table 3.3 for Actuator MA (Moment Arm). Table 3.3 represents the derived force, in lbf (pounds force), for each actuator, where actuator quantities per flap/slat were determined. In each case, for flap cases 1-6, force requirement levels are less (i.e. the largest per actuator force required is 14,317 lbf in Table 3.3) than the capabilities of current EMA technology (~ 65K lbf maximum). For the 80% Fuel Flap Actuator Case complete calculations are included; however, for the 20% Fuel Flap Actuator Case and both of the Slat Actuator Cases these additional calculations are removed and only results are displayed for brevity.

Using Table 3.3 data, the total power required for wing control actuation can be determined. This would permit design of power distribution and aircraft wiring. Also specified for the design will be dynamic response bandpass and rate requirements.

In each case above, for the wing flaps and for the wing slats, the values derived for the actuator force required are well within current technologies for single electromechanical actuation, which this analysis has addressed. Table 3.3 considers both the 80% Fuel Full case and the 20% Fuel Remaining case in developing the actuator sizing required for the flaps as well as the slat actuators. Boeing, using NASA lift data, developed an integrated lift vector for each flap and slat surface and applied these through a chord-wise ratio of the flap or slat element lengths for the actuator analysis above.

A linear model was used and the constraints of other effects can be added to improve the accuracy of this sizing. Stall torque load margins and drag effects, for instance, would increase the actuator sizing shown. However, since the force requirements above are well within the capability of current electromechanical actuation technology, the additional requirements are anticipated to be relatively easily achievable.

3.3.2 Actuation Alternatives

The actuation system can be of many forms, including all electric, all hydraulic and a combined form termed electro-hydrostatic. The electro-mechanical actuators (EMAs) can address several categories that can offer advantages and disadvantages when considered in a design trade study for an architecture of a flight control system for a morphing wing structure, the subject of this study.

EMAs can be differentiated by their motor type (Brushless DC, AC, etc.) but also by the type of drive mechanism they employ. One common aircraft type utilizes a “ballscrew” design, wherein rollers within a geared “nut” are used to turn a rotating screw which then also translates driving into the load. A generalized arrangement of this type is shown below in Figure 3.5.

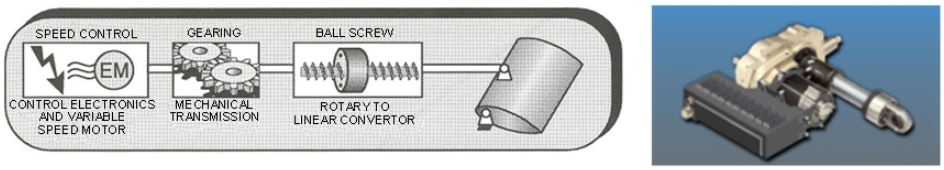

Figure 3.5 - Electromechanical Actuator (Boeing Research & Technology)

A variation of this type of EMA uses a “roller screw” in place of the “ballscrew” internally for its drive, which is connected through gearing to a variable speed electric motor. Each of these types of EMAs is electric motor driven and generally has a frequency response of 6-12 Hz (maximum).

Another actuator type is the electrohydrostatic actuator that employs a hydraulic motor but uses its variable speed electric motor to drive the internal hydraulic pump required for the hydraulic portion under electronic flight control. This type is broken down into its component pieces in Figure 3.6 below.

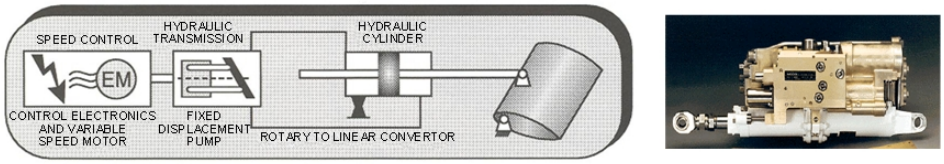

Figure 3.6 - Electrohydrostatic Actuator (Boeing Research & Technology)

Most common in service today, even with the advent of high voltage electric power systems and EMAs, is the traditional hydraulic actuation system. This system requires, of course, a central hydraulic reservoir system and hydraulic main pumps, usually engine driven and plumbing, valves etc. for hydraulic fluid distribution throughout the aircraft. A generalized version of the actuator itself is provided on Figure 3.7 below.

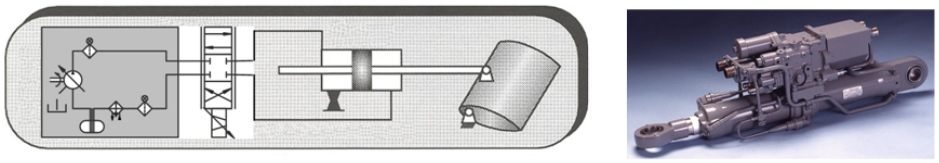

Figure 3.7 - Electrohydrostatic Actuator (Boeing Research & Technology)

Trends in actuator weight vs. power are presented in Figure 3.8 below. Weight is directly proportional to output power, so load and rate must be established. Usually Boeing would specify stall load and no load rate, take the product, convert to power and use 40% to define the design output power. Peak power for each is 100% of the product of stall load and no load rate. What is more challenging is that the weight of different components has a different slope vs. power and the y intercept is positive and varies as well.

Although weights for the larger EMA actuators needed for flap actuation would fall into the 150-200 lb range, the future trends in development point to possible 20% and greater reduction in unit actuator weights.

Real keys in determining the design for the actual actuator to be used trade weight vs. range requirements and power vs. range. Knowing these, a range sensitivity can be determined to pick the optimal operating points.

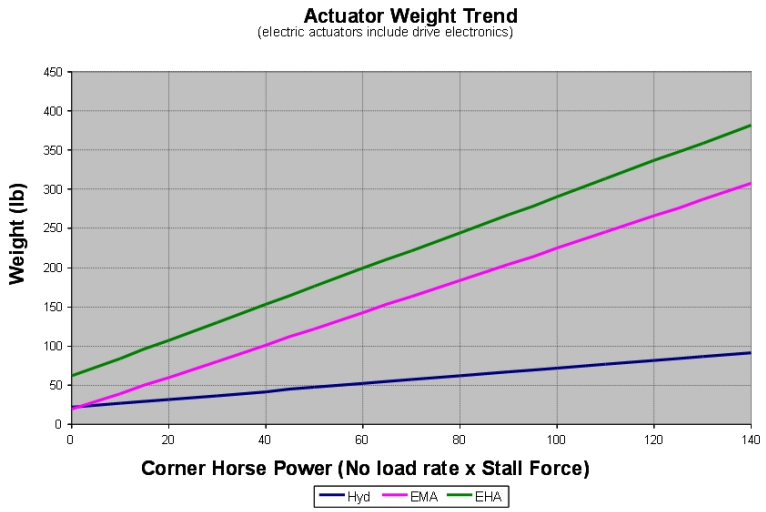

Figure 3.8 - Actuator Weight Trend by Type (Boeing Research & Technology)

3.4 Low-Drag Variable Camber Continuous Trailing Edge Flap Concept

In a conventional flap design, individual flaps are actuated independently. As a result, the trailing edge of a wing formed by the flap deflections is discontinuous. This discontinuity is a source of drag penalty as well as acoustic emissions. The VORVIEW results show that the drag penalty due to the conventional flap system is substantial. One way to reduce the drag penalty is to use a single flap surface over a wide wing span. However, this would compromise the flexibility and effectiveness of wing shaping control. A novel new flap concept is thus introduced to address the drag reduction goal of the study. This flap concept is called a variable camber continuous trailing edge flap. Figure 3.9 illustrates the continuous flap concept.

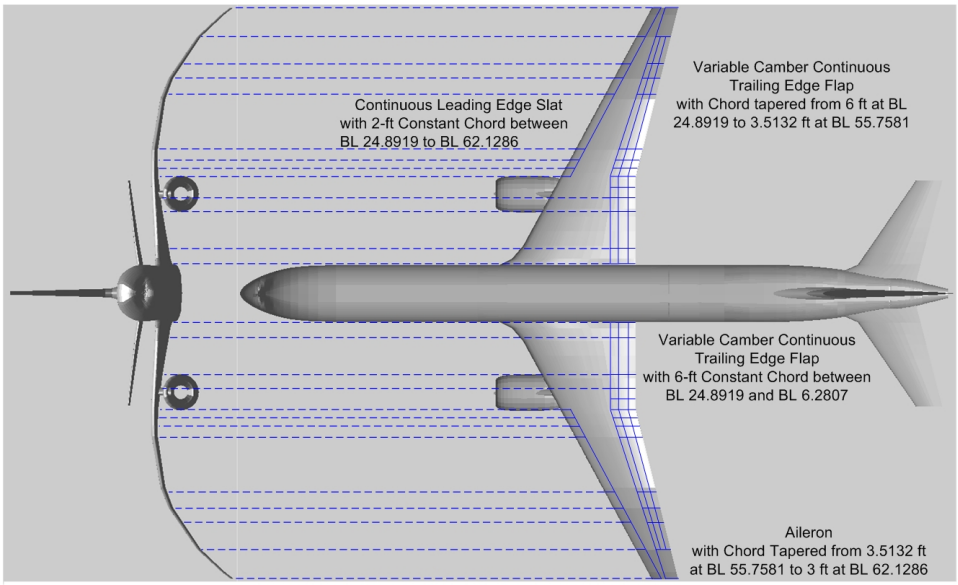

Figure 3.9 - Variable Camber Continuous Trailing Edge Flap System

The two main features of this flap concepts that provide significant drag reduction benefits are:

- Variable camber flap - The flap chord is comprised of three chordwise segments of equal chord length as shown in Figure 3.10. These three flap segments are actuated in unison when a flap deflection command is given. Each

flap segment is deflected by an angle equal to one third of the commanded flap deflection relative to each other. For example, for a commanded flap deflection of 12°, flap segment 1 which is positioned next to the wing is deflected 4°, flap segment 2 that follows flap segment 1 is deflected 8°, and flap segment 3 at the trailing edge is deflected by 12°. Thus

$$f_1 = \frac{f_c}{3} \tag{3.3}$$

$$f_2 = \frac{2f_c}{3} \tag{3.4}$$

$$f_3 = f_c \tag{3.5}$$

where f_c is the commanded flap deflection.

The camber angle of the flap is the difference between between f_3 and f_1. Thus, the variable camber angle $\chi = 2f_c/3$ is a function of the commanded flap deflection. A cambered flap is more effective in producing lift than a straight uncambered flap.

The variable camber flap produces about the same downwash as a simple plain flap deflected by the same angle, as seen in Figure 3.10. However, the normal surface area of the variable camber flap exposed to the flow field is significantly reduced. Thus, the drag reduction benefit of the variable camber flap is realized since the pressure drag across the flap surface is reduced due to less exposed normal surface area.

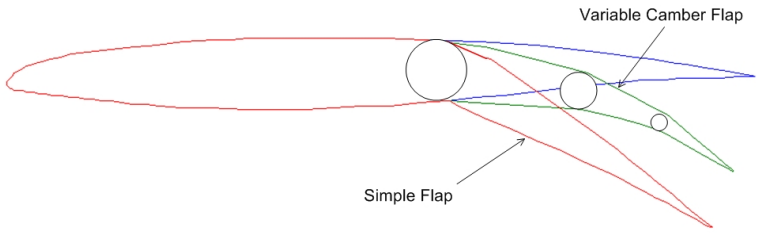

Figure 3.10 -Variable Camber Flap

- Continuous trailing edge flap - The continuous flap is comprised of 12 spanwise segments to form a continuous trailing edge when the flap is deflected. This continuous trailing edge would eliminate vortices which otherwise would have formed at the conventional flap discontinuity in the trailing edge region. By reducing or eliminating vortex formation, drag losses as well as acoustic emissions from turbulence could be attenuated. Thus, this feature further provides a drag reduction benefit in addition to the variable camber flap concept.

  The flap spans the wing trailing edge from BBL 6.2807 ft, which is abutted to the fuselage, to BBL 55.7581 ft. The flap deflection angle varies continuously from zero at these two BBL stations to the maximum commanded flap deflection at BBL 24.8919 ft. The chord is tapered from 6 ft at BBL 24.8919 ft to 3.5132 ft at BBL 55.7581 ft, and then remains constant at 6 ft between BBL 6.2807 ft to BBL 24.8919 ft. A theoretical smooth trailing edge shape is generated by a 5th-degree polynomial to enforce the boundary conditions as follows:

$$f_n(y) = a_5 y^5 + a_4 y^4 + a_3 y^3 + a_2 y^2 + a_1 y + a_0 \tag{3.6}$$

  where f_n is the continuous flap deflection of flap n, $n = 1,2,3$, y is the BBL station, and a_i, $i = 1,2,3,4,5$ are the polynomial coefficients that satisfy the following boundary conditions

$$f_n(y_1 = 6.2807) = 0$$

$$f_n'(y_1 = 6.2807) = 0$$

$$f_n(y_2 = 24.8919) = \frac{nf_c}{3}$$

$$f_n'(y_2 = 24.8919) = 0$$

$$f_n(y_3 = 55.7581) = 0$$

$$f_n'(y_3 = 55.7581) = 0$$

The coefficients a_i, $i = 1,2,3,4,5$ are determined as

$$\begin{bmatrix} a_5 \\ a_4 \\ a_3 \\ a_2 \\ a_1 \\ a_0 \end{bmatrix} = \begin{bmatrix} y_1^5 & y_1^4 & y_1^3 & y_1^2 & y_1 & 1 \\ 5y_1^4 & 4y_1^3 & 3y_1^2 & 2y_1 & 1 & 0 \\ y_2^5 & y_2^4 & y_2^3 & y_2^2 & y_2 & 1 \\ 5y_2^4 & 4y^3 & 3y_2^2 & 2y_2 & 1 & 0 \\ y_3^5 & y_3^4 & y_3^3 & y_3^2 & y_3 & 1 \\ 5y_3^4 & 4y_3^3 & 3y_3^2 & 2y_3 & 1 & 0 \end{bmatrix}^{-1} \begin{bmatrix} 0 \\ 0 \\ \frac{nf_c}{3} \\ 0 \\ 0 \\ 0 \end{bmatrix} = nf_c \begin{bmatrix} -1.2929 \times 10^{-7} \\ 2.2291 \times 10^{-5} \\ -4.5450 \times 10^{-4} \\ 3.4045 \times 10^{-2} \\ -2.8738 \times 10^{-1} \\ 7.6635 \times 10^{-1} \end{bmatrix} \tag{3.7}$$

Figure 3.11 shows the theoretical continuous trailing edge flap deflection curve and the flap chord distribution.

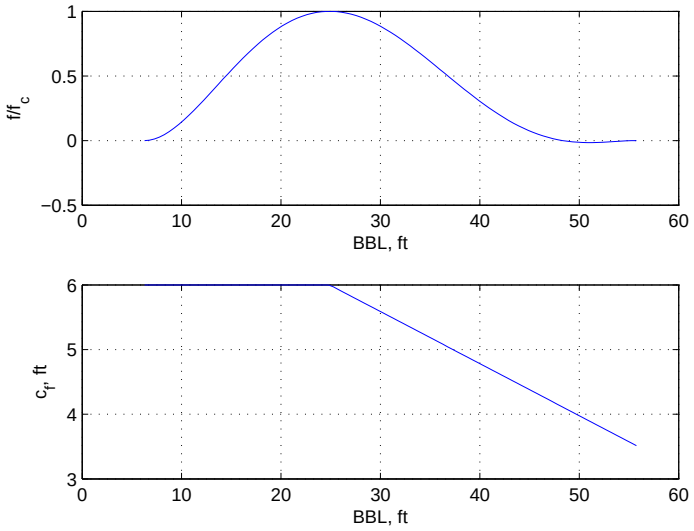

Figure 3.11 - Theoretical Continuous Trailing Edge Flap Deflection

To approximate this continuous trailing edge curve, the continuous flap system can be made of 12 continuous flap segments where they join together to form a continuous trailing edge. Each flap segment is designed to be actuated in relation to the adjacent flap segments in the spanwise direction to form a continuous trailing edge, as well as in the chordwise direction to form a desired camber. Tables 3.4(a) and 3.4(b) show the BBL stations of the 12 flap segments numbered from 1 to 12 from outboard to inboard.

	1	2	3	4	5	6
Outboard BBL	55.7581	49.1475	46.2442	42.6498	31.0369	28.4101
Inboard BBL	49.1475	46.2442	42.6498	31.0369	28.4101	26.7512
Outboard $3f_n/nf_c$	0	-0.0085	0.0390	0.1669	0.8374	0.9433
Inboard $3f_n/nf_c$	-0.0085	0.0390	0.1669	0.8374	0.9433	0.9837

Table 3.4(a) - Continuous Trailing Edge Flap Segments 1 to 6

	7	8	9	10	11	12
Outboard BBL	26.7512	24.8919	22.7419	20.6682	17.6267	9.4700
Inboard BBL	24.8919	22.7419	20.6682	17.6267	9.4700	6.2807
Outboard $3f_n/nf_c$	0.9837	1.0000	0.9772	0.9115	0.7430	0.1095
Inboard $3f_n/nf_c$	1.0000	0.9772	0.9115	0.7430	0.1095	0

Table 3.4(b) - Continuous Trailing Edge Flap Segments 7 to 12

Figure 3.12 shows the BBL stations of the 12 flap segments.

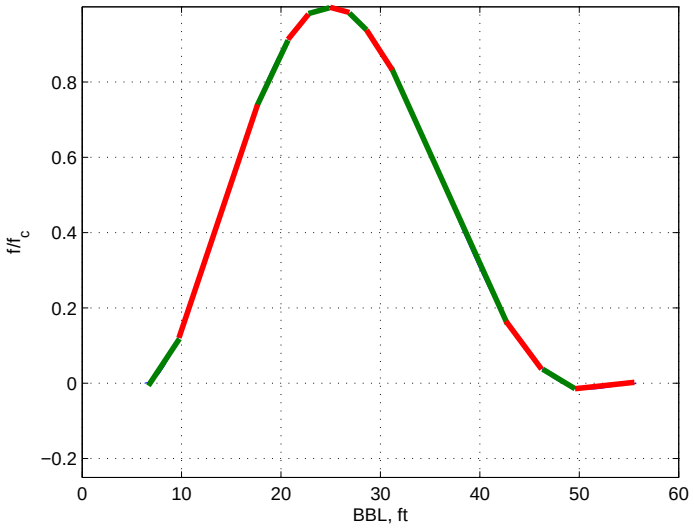

Figure 3.12 - Continuous Trailing Edge Flap Segments

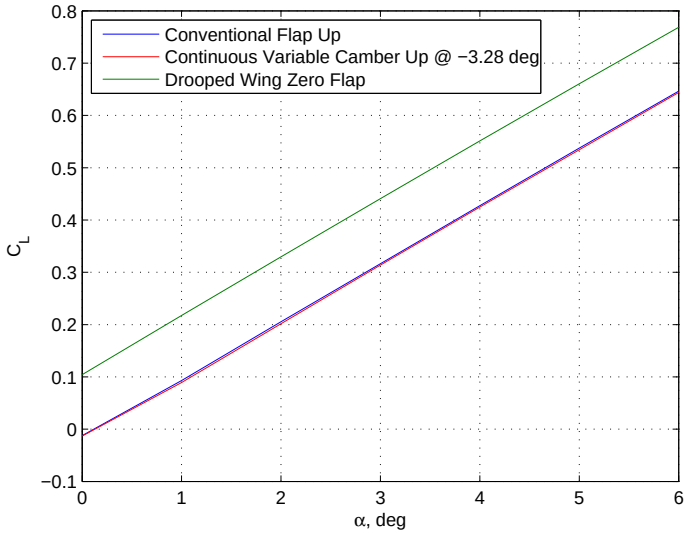

Figure 3.13 - C_L versus α for Negative Flaps at Start of Cruise

The variable camber continuous trailing edge flap concept is implemented in VORVIEW to estimate the potential drag reduction benefit. The commanded flap deflection is adjusted until the C_L versus α curve matches that for the drooped-wing aircraft with the previously computed conventional flap deflections at the start and end of cruise. Figures 3.13 and 3.14 show the C_L versus α curves for the flap deflections at the start and end of cruise. The drag reduction benefits of the variable camber continuous trailing flap system can be demonstrated by Figures 3.15 and 3.16. It is apparent that the variable camber continuous trailing edge flap concept offers substantial drag reduction benefits. The incremental C_D values are 0.00216 at the start and 0.00234 at the end of cruise. The results show drag reduction benefits ranging from 66% at the start of cruise to 46% at the end of cruise. Moreover, it is noted that the C_D values for the variable camber continuous trailing edge flap are even lower than the baseline values for the drooped wing for C_L values greater than 0.43. This implies that the variable camber continuous flap concept is more aerodynamically efficient of producing lift at high C_L values.

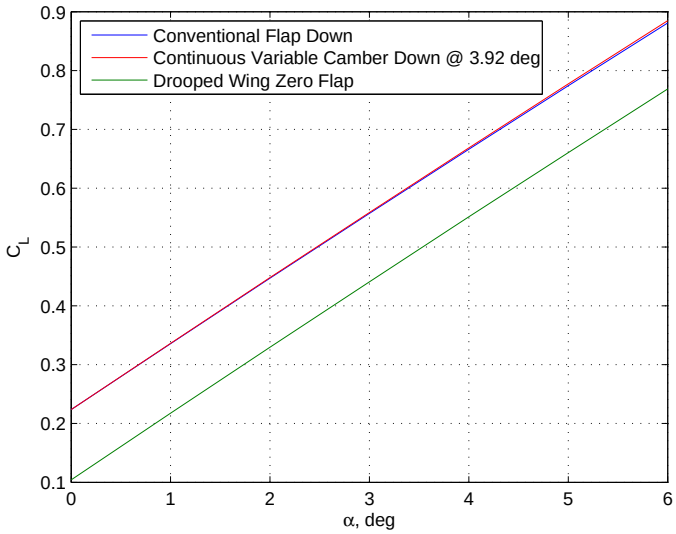

Figure 3.14 - C_L versus α for Positive Flaps at End of Cruise

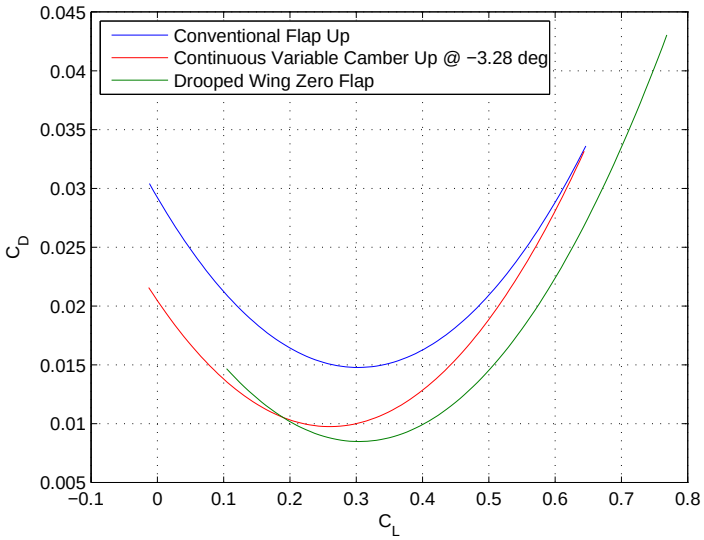

Figure 3.15 - Drag Polars for Plain Discrete Flaps and Variable Camber Continuous T.E. Flap at Negative Deflection

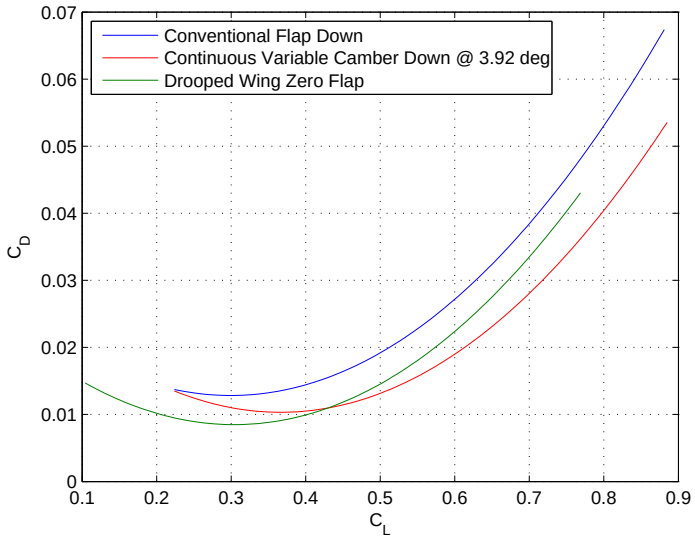

Figure 3.16 - Drag Polars for Plain Discrete Flaps and Variable Camber Continuous T.E. Flap at Positive Deflection

4 Performance Analysis

The ultimate goal of optimal wing shape and wing shaping control is to reduce fuel burn. Among the three configurations presented, the drooped-wing shape aircraft configuration is chosen for comparison with the benchmark aircraft. Although the squashed fuselage concept appears to be a better configuration, the comparison would not be on the same basis due to the fuselage aerodynamic improvement in addition to the optimal drooped wing. Moreover, the potential benefit of wing shaping control can be better demonstrated with the drooped-wing aircraft configuration.

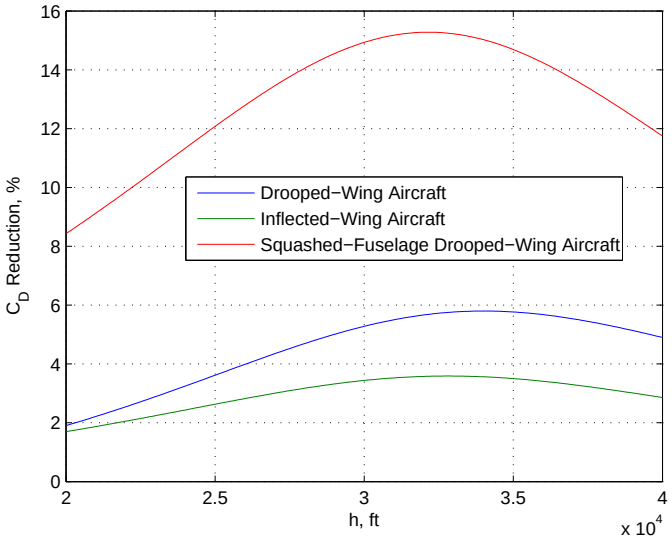

Figure 4.1 - C_D versus Altitude of Three Optimal Configurations

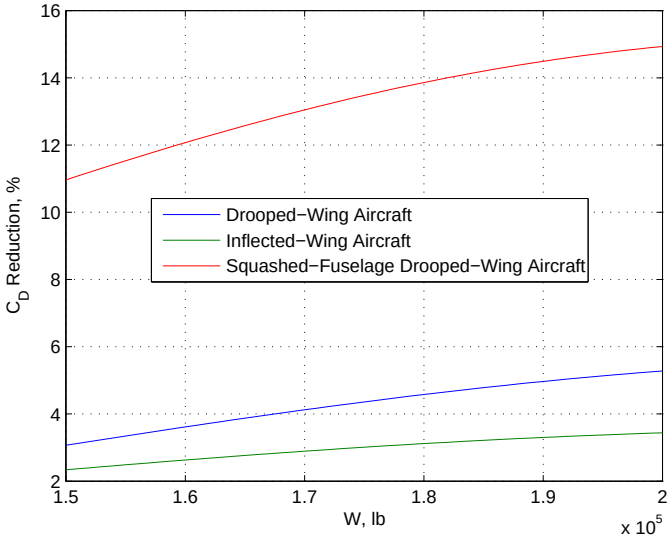

Figure 4.2 - C_D versus Aircraft Weight of Three Optimal Configurations

As the lift coefficient changes due to changes in altitude or aircraft weight resulting from the fuel burn, the drag coefficient changes accordingly. There is a combination of optimal aircraft weight and altitude that minimize drag. Figures 4.1 and 4.2 show the induced-drag reduction relative to the baseline C_D value of the benchmark aircraft as a function of altitude and the aircraft weight. Figure 4.1 indicates that the best C_D reduction for the drooped-wing aircraft configuration is at about 34,000 ft with a drag reduction of almost 6%. On the other hand, the squash-fuselage

drooped-wing aircraft configuration achieves about 15% induced drag reduction. In terms of the optimal weight for drag reduction, Figure 4.2 shows that better drag reduction is achieved at a higher aircraft weight than at a lower value. Thus, the best drag reducing flight condition for the drooped-wing aircraft concept is at 34,000 ft with the aircraft weight at 200,000 lbs. However, if the optimal drooped wing shape is at the full tank point in cruise, the difference in aircraft weight at the end of cruise when most of the fuel has been expended could be substantial that could drive the wing shaping control flap and slat deflection requirements to large values which would incur a large drag penalty. For this reason, the half-way point in cruise is select as the design flight condition at which the wing shape attains it optimal drooped-wing shape with no flap or slat deflection.

4.1 Aeroelastic Deflection Effect

Aeroelastic deflection can affect aircraft aerodynamics. As the aircraft cruises, fuel is burned and the wing loading is reduced, thereby causing the wing shape to displace downward and the wing twist to pitch nose-down. The change in wing shape can cause a drag penalty since the wing shape no longer retains its optimal drooped-wing shape. The objective of wing shaping control is to restore the wing shape back to its optimal shape through flap and slat deployments. However, the drag penalty due to flap and slat deflections can negate any benefit attained from wing shaping control. To assess the relative benefit of wing shaping control, a static aeroelastic deflection analysis is conducted to compute the wing bending and torsional deflections as discussed in Section 5. If the optimal wing shape occurs at the half-way point in cruise, then the wing deflections will be due to the $\pm 30\%$ fuel weight variations between the start and end of cruise. The wing bending and torsion deflection shapes are then superimposed on top of the drooped-wing shape to create a new wing shape for which new aerodynamic coefficients are computed using VORVIEW.

The results do indicate a significant drag penalty as the wing shape moves away its optimal shape. Figure 4.3 shows the drag polars at the three points in the cruise envelope: 80% fuel, 50% fuel, and 20% fuel. Let

- C_L and C_D be the values corresponding to the drooped-wing aircraft configuration
- C_{L_f} and C_{D_f} be the values corresponding to the drooped-wing aircraft configuration with wing shaping control using variable camber continuous trailing edge flap system which results in incremental ΔC_{L_f} and ΔC_{D_f} values which are assumed to be linearly varying with flap deflections
- C_L^* and C_D^* be the baseline values corresponding to the benchmark aircraft

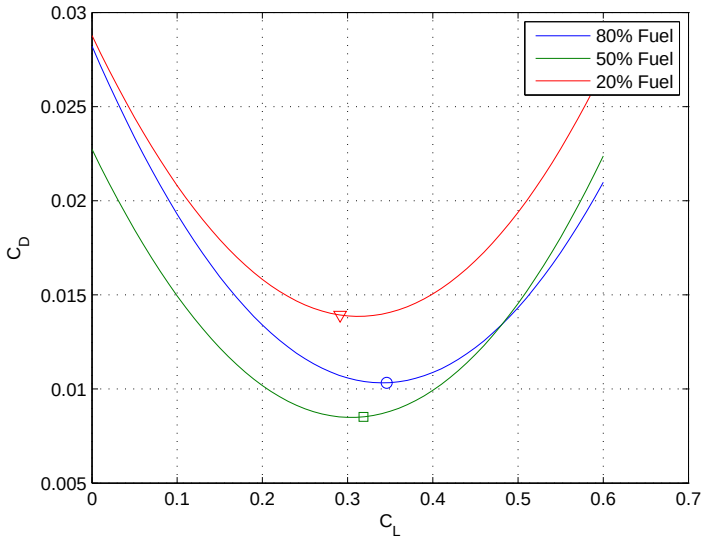

Figure 4.3 - C_D Penalty due to Aeroelastic Deflection for Drooped-Wing Aircraft

Table 4.1 shows the lift and drag coefficients as a function of the fuel burn and with aeroelastic deflections taken into account

Fuel Ratio	C_L	C_D	C_D^*	ΔC_{D_f}	C_{D_f}	ΔC_{L_f}	C_{L_f}
0.2	0.2913	0.01393	0.01530	0.00234	0.01085	0.1347	0.4260
0.3	0.3004	0.01371	0.01533	0.00156	0.01005	0.0898	0.3902
0.4	0.3095	0.01358	0.01539	0.00078	0.00927	0.0449	0.3544
0.5	0.3186	0.00852	0.01541	0	0.00852	0	0.31858
0.6	0.3277	0.01051	0.01543	0.00072	0.00929	-0.0426	0.2851
0.7	0.3368	0.01042	0.01552	0.00144	0.01009	-0.0852	0.2516
0.8	0.3459	0.01033	0.01557	0.00216	0.01092	-0.1278	0.2180

Table 4.1 - C_L and C_D due to Aeroelastic Deflection and Fuel Burn

Clearly wing shaping control would be beneficial if the drag penalty due to the flap and slat deflections does not exceed that due to a non-optimal wing shape. It is also clear that the conventional flap and slat systems are not beneficial for wing shaping control because of its large drag penalty. Table 4.1 shows that the variable camber continuous trailing edge flaps are not beneficial until the fuel point reaches about 70%. However, for the flap down configuration when the fuel is less than half full, the variable camber continuous trailing edge flaps become quite beneficial as the C_{D_f} values are significantly less than the C_D values. Comparing the C_{D_f} values with the baseline C_D^* values, the drag reduction of the wing shaping control of the drooped-wing aircraft configuration is quite apparent. The large C_D^* values are due to the adverse effect of aeroelastic deflections. Also since the drooped-wing aircraft configuration includes a 1-g aeroelastic deflection in the as-built configuration, the adverse effect of aeroelastic deflections is minimized for the drooped-wing aircraft configuration.

4.2 Cruise Analysis

During cruise, fuel is burned by the engines that causes a change in the aircraft weight according to the weight equation

$$\dot{W} = -cT \tag{4.1}$$

where T is the engine thrust and c is the Thrust Specific Fuel Consumption (TSFC) which is equal to 0.593/hr for Mach 0.8 and 30,000 ft according to Eq. (2.2).

Range and endurance are two performance parameters for an aircraft in a cruise phase. Range is defined as the distance that an aircraft can fly for a given amount of fuel available. The range can be computed from the Breguet range equation [12]

$$r = -\int_{W_t}^{W_f} \frac{V_\infty}{cT} dW \tag{4.2}$$

In cruise, drag is equal to thrust and lift equal to weight. Then the range equation can be written as

$$r = -\int_{W_t}^{W_f} \frac{V_\infty}{c} \left(\frac{C_L}{C_D}\right) \frac{dW}{W} \tag{4.3}$$

Thus the range is proportional to the aerodynamic efficiency which is defined as the lift-to-drag ratio or $E = C_L/C_D$. Table 4.2 shows the value of the aerodynamic efficiency.

Fuel Ratio	E	E^*	E_f
0.2	20.9131	18.8654	39.2563
0.3	21.9139	19.5893	38.8319
0.4	22.7914	20.2627	38.2267
0.5	37.3963	20.9571	37.3963
0.6	31.1770	21.6148	30.6735
0.7	32.3193	22.1613	24.9207
0.8	33.4859	22.7027	19.9656

Table 4.2- Aerodynamic Efficiency

An interesting observation is made in that the aerodynamic efficiency for the flap-up configuration when the fuel is more than 50% is lower than the no-flap configuration. Thus, there is no advantage for wing shaping control when the flaps are configured in the upward position. On the other hand, the downward deflection of flaps is highly beneficial in increasing the aerodynamic efficiency. Hence, for the cruise analysis, it will be assumed that wing shaping control will only be used when the fuel is less than half full in the tank.

Figure 4.4 is a plot of three different cruise ranges for the three aircraft configurations. The drooped-wing aircraft configuration with no wing shaping control provides a significant benefit of fuel savings. At a first glance, it appears that the fuel savings with the drooped-wing aircraft configuration are huge as compared to the benchmark aircraft . However, the comparison may not be on the same basis since the drooped-wing aircraft configuration has an advantage of the aeroelastic tailoring by incorporating the 1-g aeroelastic deflection into the as-built configuration. If this aeroelastic tailoring is also applied to the benchmark aircraft, then the fuel savings will be less and probably will be in the ball park of the 5.3% drag reduction.

Comparing between the drooped-wing aircraft configuration with and without wing shaping control, The advantage of wing shaping control can clearly be demonstrated. For a 4500 mile range, a fuel saving of 17% is realized due to wing shaping control. This result clearly indicates the benefits of wing shaping control for long range cruises. For short range cruises with the fuel burn less than half of the fuel, there is no benefit of wing shaping control. Thus, in summary, the drag reduction benefits of both the drooped-wing shape and the variable camber continuous trailing edge flap can result in substantial fuel savings. The result thus merits a further investigation as part of a follow-on effort to develop the concepts in a more-in-depth study.

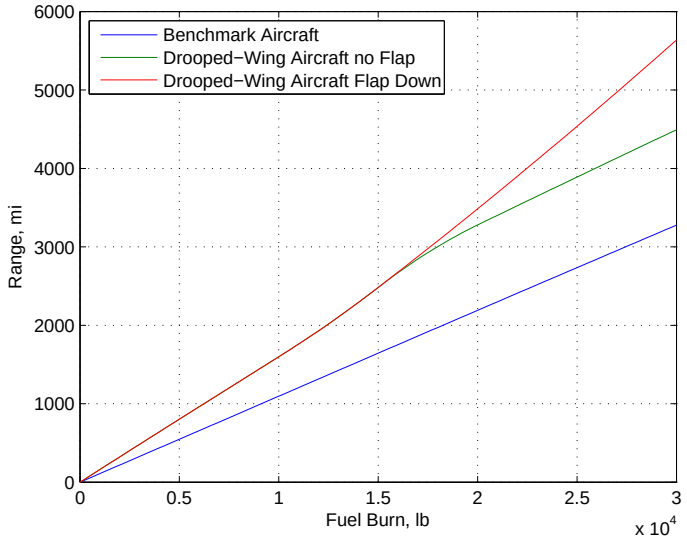

Figure 4.4 - Comparison of Cruise Ranges

5 Aeroelastic Flight Dynamic Modeling

The elastic shaped aircraft concept is assumed to have flexible wings that can be elastically shaped in-flight by wing shaping control. In order to develop active wing shaping control, the effect of structural flexibility of the wing on aircraft flight dynamics must be considered. Aeroelasticity theory is used to develop an aeroelastic flight dynamic model of the elastically shaped aircraft concept to account for interactions between wing bending and torsion on aircraft performance and stability.

5.1 Reference Frames

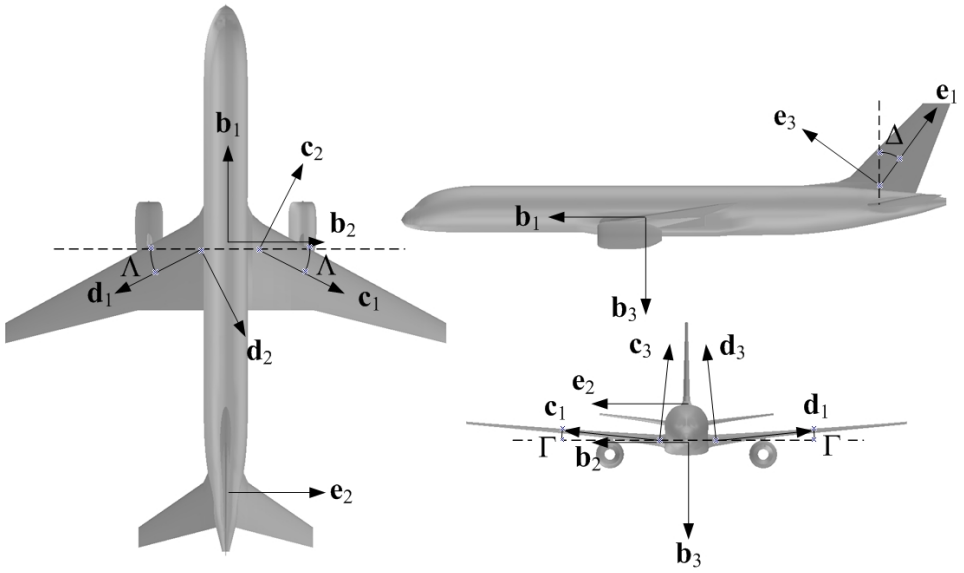

Figure 5.1 - Aircraft Reference Frames

Figure 5.1 illustrates three orthogonal views of a typical aircraft. Several reference frames are introduced to facilitate the rigid-body dynamic and structural dynamic analysis of the lifting surfaces. For example, the aircraft inertial reference frame A is defined by unit vectors $\mathbf{a}_1$, $\mathbf{a}_2$, and $\mathbf{a}_3$ fixed to the non-rotating earth. The aircraft body-fixed reference frame B is defined by unit vectors $\mathbf{b}_1$, $\mathbf{b}_2$, and $\mathbf{b}_3$. The reference frames A and B are related by three successive rotations: 1) the first rotation about $\mathbf{a}_3$ by the heading angle ψ that results in an intermediate reference frame A$'$ defined by unit vectors $\mathbf{a}_1'$, $\mathbf{a}_2'$, and $\mathbf{a}_3'$ (not shown), 2) the second rotation about $\mathbf{a}_2'$ by the pitch angle θ that results in an intermediate reference frame B$'$ defined by unit vectors $\mathbf{b}_1'$, $\mathbf{b}_2'$, and $\mathbf{b}_3'$ (not shown), and 3) the third rotation about $\mathbf{b}_1'$ by the bank angle ϕ that results in the reference frame B. This relationship can be expressed as

$$\begin{bmatrix} \mathbf{a}_1 \\ \mathbf{a}_2 \\ \mathbf{a}_3 \end{bmatrix} = \begin{bmatrix} \cos\psi & -\sin\psi & 0 \\ \sin\psi & \cos\psi & 0 \\ 0 & 0 & 1 \end{bmatrix} \begin{bmatrix} \cos\theta & 0 & \sin\theta \\ 0 & 1 & 0 \\ -\sin\theta & 0 & \cos\theta \end{bmatrix} \begin{bmatrix} 1 & 0 & 0 \\ 0 & \cos\phi & -\sin\phi \\ 0 & \sin\phi & \cos\phi \end{bmatrix} \begin{bmatrix} \mathbf{b}_1 \\ \mathbf{b}_2 \\ \mathbf{b}_3 \end{bmatrix}$$

$$= \begin{bmatrix} \cos\psi\cos\theta & -\sin\psi\cos\phi + \cos\psi\sin\theta\sin\phi & \sin\psi\sin\phi + \cos\psi\sin\theta\cos\phi \\ \sin\psi\cos\theta & \cos\psi\cos\phi + \sin\psi\sin\theta\sin\phi & -\cos\psi\sin\phi + \sin\psi\sin\theta\cos\phi \\ -\sin\theta & \cos\theta\sin\phi & \cos\theta\cos\phi \end{bmatrix} \begin{bmatrix} \mathbf{b}_1 \\ \mathbf{b}_2 \\ \mathbf{b}_3 \end{bmatrix} \quad (5.1)$$

The left wing elastic reference frame D is defined by unit vectors $\mathbf{d}_1$, $\mathbf{d}_2$, and $\mathbf{d}_3$. The reference frames B and D are related by three successive rotations: 1) the first rotation about $\mathbf{b}_3$ by the elastic axis sweep angle $\frac{3\pi}{2} - \Lambda$ that results in an intermediate reference frame B$''$ defined by unit vectors $\mathbf{b}_1''$, $\mathbf{b}_2''$, and $\mathbf{b}_3''$ (not shown), 2) the second rotation about negative $\mathbf{b}_2''$ by the elastic axis dihedral angle Γ that results in an intermediate reference frame D$'$ defined by unit vectors $\mathbf{d}_1'$, $\mathbf{d}_2'$, and $\mathbf{d}_3'$ (not shown), and 3) the third rotation about $\mathbf{d}_1'$ by an angle π that results in the reference frame

D. This relationship can be expressed as

$$\begin{bmatrix} \mathbf{b}_1 \\ \mathbf{b}_2 \\ \mathbf{b}_3 \end{bmatrix} = \begin{bmatrix} -\sin\Lambda & \cos\Lambda & 0 \\ -\cos\Lambda & -\sin\Lambda & 0 \\ 0 & 0 & 1 \end{bmatrix} \begin{bmatrix} \cos\Gamma & 0 & -\sin\Gamma \\ 0 & 1 & 0 \\ \sin\Gamma & 0 & \cos\Gamma \end{bmatrix} \begin{bmatrix} 1 & 0 & 0 \\ 0 & -1 & 0 \\ 0 & 0 & -1 \end{bmatrix} \begin{bmatrix} \mathbf{d}_1 \\ \mathbf{d}_2 \\ \mathbf{d}_3 \end{bmatrix}$$

$$= \begin{bmatrix} -\sin\Lambda\cos\Gamma & -\cos\Lambda & -\sin\Lambda\sin\Gamma \\ -\cos\Lambda\cos\Gamma & \sin\Lambda & \cos\Lambda\sin\Gamma \\ \sin\Gamma & 0 & -\cos\Gamma \end{bmatrix} \begin{bmatrix} \mathbf{d}_1 \\ \mathbf{d}_2 \\ \mathbf{d}_3 \end{bmatrix} \tag{5.2}$$

Generally, the effect of the dihedral angle can be significant. A full analysis with the dihedral angle can be performed but can also result in a very complex analytical formulation. Thus, to simplify the analysis, the dihedral effect is assumed to be negligible in this study. The right wing reference frame C can be established in a similar manner. In the analysis, the aeroelastic effects on the fuselage, horizontal stabilizers, and vertical stabilizer are not considered, but the analytical method can be formulated for analyzing these lifting surfaces if necessary. In general, a whole aircraft analysis approach should be conducted to provide a comprehensive assessment of the effect of structural flexibility on aircraft performance and stability. However, the scope of this study pertains to only the wing structures.

5.2 Elastic Analysis

In the subsequent analysis, the combined motion of the left wing is considered. The wing has a varying pre-twist angle $\gamma(x)$ common in many aircraft. Typically, the wing pre-twist angle varies from being nose-up at the wing root to nose-down at the wing tip. The nose-down pre-twist at the wing tip is designed to delay stall onsets. This is called a wash-out twist distribution. Under aerodynamic forces and moments, wing structural deflections introduce strains in the wing structure. For high aspect ratio wings, an equivalent beam approach can be used to analyze structural deflections with a reasonable accuracy. The equivalent beam approach is a typical formulation in many aeroelasticity studies [13]. Experimental validation can show that equivalent beam approach is accurate for an aspect ratio as low as 3:1. The internal structure of a wing typically comprises a complex arrangement of load carrying spars and wing boxes. Nonetheless, the elastic behavior of a wing can be captured by the use of equivalent stiffness properties. These properties can be derived from structural certification testing that yields information about wing deflection as a function of loading. It is assumed that the effect of wing curvature is ignored and the straight beam theory is used to model the wing deflection.

Consider an airfoil section on the left wing as shown in Figure 5.2 undergoing bending and twist deflections.

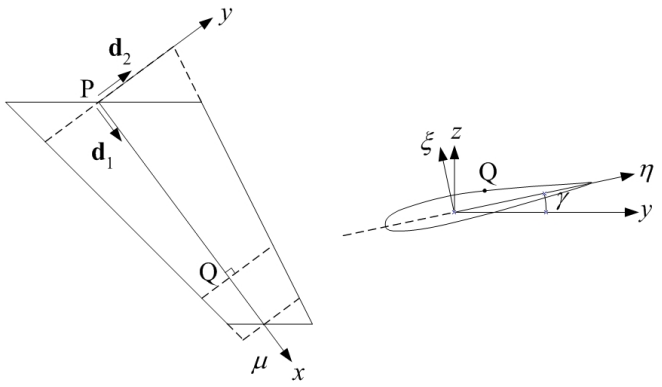

Figure 5.2 - Left Wing Reference Frame

Let (x,y,z) be the coordinates of a point Q on the airfoil. Then

$$\begin{bmatrix} y \\ z \end{bmatrix} = \begin{bmatrix} \cos\gamma & -\sin\gamma \\ \sin\gamma & \cos\gamma \end{bmatrix} \begin{bmatrix} \eta \\ \xi \end{bmatrix} \tag{5.3}$$

where η and ξ are local airfoil coordinates, and γ is the wing section pre-twist angle, positive nose-down [14].

The axial or extensional deflection of a wing is generally very small and therefore can usually be neglected. Let V and W be chordwise and flapwise bending deflections of point Q, respectively, and let Θ be a torsional twist angle about the x-axis, positive nose-down. Then, the rotation angle due to the structural deformation can be expressed as

$$\phi(x,t) = \Theta \mathbf{d}_1 - W_x \mathbf{d}_2 + V_x \mathbf{d}_3 \tag{5.4}$$

where the subscripts x and t denote the partial derivatives of V, W, and Θ.

Let (x_1, y_1, z_1) be the coordinates of point Q on the airfoil in the reference frame D. Then the coordinates (x_1, y_1, z_1) are computed using the small angle approximation as [15]

$$\begin{bmatrix} x_1(x,t) \\ y_1(x,t) \\ z_1(x,t) \end{bmatrix} = \begin{bmatrix} x \\ y+V \\ z+W \end{bmatrix} + \begin{bmatrix} \phi \times (y\mathbf{d}_2 + z\mathbf{d}_3) . \mathbf{d}_1 \\ \phi \times (y\mathbf{d}_2 + z\mathbf{d}_3) . \mathbf{d}_2 \\ \phi \times (y\mathbf{d}_2 + z\mathbf{d}_3) . \mathbf{d}_3 \end{bmatrix} = \begin{bmatrix} x - yV_x - zW_x \\ y + V - z\Theta \\ z + W + y\Theta \end{bmatrix} \tag{5.5}$$

Differentiating x_1, y_1, and z_1 with respect to x yields

$$\begin{bmatrix} x_{1,x} \\ y_{1,x} \\ z_{1,x} \end{bmatrix} = \begin{bmatrix} 1 - yV_{xx} + z\gamma' V_x - zW_{xx} - y\gamma' W_x \\ -z\gamma' + V_x - z\Theta_x - y\gamma'\Theta \\ y\gamma' + W_x + y\Theta_x - z\gamma'\Theta \end{bmatrix} \tag{5.6}$$

Neglecting the transverse shear effect, the longitudinal strain is computed as

$$\varepsilon = \frac{ds_1 - ds}{ds} = \frac{s_{1,x}}{s_x} - 1 \tag{5.7}$$

where

$$s_x = \sqrt{1 + y_x^2 + z_x^2} = \sqrt{1 + (y^2 + z^2)(\gamma')^2} \tag{5.8}$$

$$s_{1,x} = \sqrt{x_{1,x}^2 + y_{1,x}^2 + z_{1,x}^2} = \sqrt{1 + (y^2 + z^2)(\gamma')^2 - 2yV_{xx} - 2zW_{xx} + 2(y^2 + z^2)\gamma'\Theta_x} \tag{5.9}$$

For a small wing twist angle γ, the longitudinal strain is obtained as [15]

$$\varepsilon = -yV_{xx} - zW_{xx} + (y^2 + z^2)\gamma'\Theta_x \tag{5.10}$$

The moments acting on the wing are then obtained as

$$\begin{bmatrix} M_x \\ M_y \\ M_z \end{bmatrix} = \begin{bmatrix} GJ\Theta_x \\ 0 \\ 0 \end{bmatrix} + \iint E\varepsilon \begin{bmatrix} (y^2 + z^2)(\gamma' + \Theta_x) \\ -z \\ -y \end{bmatrix} dydz = \begin{bmatrix} GJ + EB_1(\gamma')^2 & -EB_2\gamma' & -EB_3\gamma' \\ -EB_2\gamma' & EI_{yy} & -EI_{yz} \\ -EB_3\gamma' & -EI_{yz} & EI_{zz} \end{bmatrix} \begin{bmatrix} \Theta_x \\ W_{xx} \\ V_{xx} \end{bmatrix} \tag{5.11}$$

where E is the Young's modulus; G is the shear modulus; γ' is the derivative of the wing pre-twist angle; I_{yy}, I_{yz}, and I_{zz} are the section area moments of inertia about the flapwise axis; J is the torsional constant; and B_1, B_2, and B_3 are the bending-torsion coupling constants which are defined as

$$\begin{bmatrix} B_1 \\ B_2 \\ B_3 \end{bmatrix} = \iint (y^2 + z^2) \begin{bmatrix} y^2 + z^2 \\ z \\ y \end{bmatrix} dydz \tag{5.12}$$

The strain analysis shows that for a pre-twisted wing the bending deflections V and W are coupled to the torsional deflection Θ via the slope of the wing pre-twist angle. This coupling can be significant if the term γ' is dominant as in highly twisted wings such as turbomachinery blades. For an aircraft wing structure, a simplification can be made by neglecting the chordwise bending deflection. Thus, the resulting moments are now given as

$$\begin{bmatrix} M_x \\ M_y \end{bmatrix} = \begin{bmatrix} GJ + EB_1(\gamma')^2 & -EB_2\gamma' \\ -EB_2\gamma' & EI_{yy} \end{bmatrix} \begin{bmatrix} \Theta_x \\ W_{xx} \end{bmatrix} \tag{5.13}$$

5.3 Structural Stiffness Estimates

Structural information for aircraft is generally not publicly available. Therefore, the uncertainty on the structural analysis can be high. Nonetheless, certain assumptions can be made for the structural stiffness of a wing if the wing deflection is known. In the study, the wing deflection for the benchmark vehicle at 1-g loading at cruise is assumed to be about 3 ft at the tip. This is based on an observation of the result of a structural certification test on a Boeing 777 wing. This wing deflected at the tip about 24 ft with an applied load of 3.75 g's. This corresponds to 1.5 times the design load which is established at 2.5 g's. The wing span of Boeing 777 is 200 ft. So the deflection at 1-g loading is estimated to be about 6.4 ft by scaling the deflection by the loading ratio. The wing tip deflection for a cantilever beam with a different length L and structural stiffness EI is proportional to L^3/EI. Assuming that EI is proportional to $L^{3/2}$. Then, the wing tip deflection is proportional to $L^{3/2}$. Using this approximation, the wing tip deflection at 1-g loading for the benchmark aircraft wing is estimated to be about 3 ft.

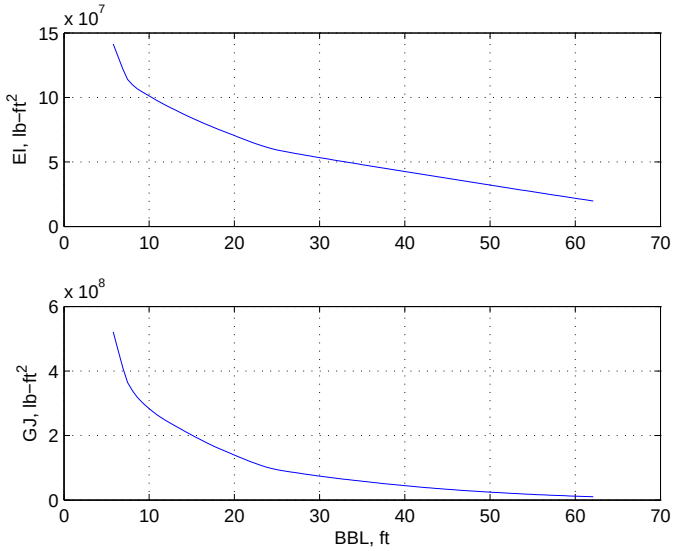

Figure 5.3 - Estimated Wing Bending and Torsional Stiffness

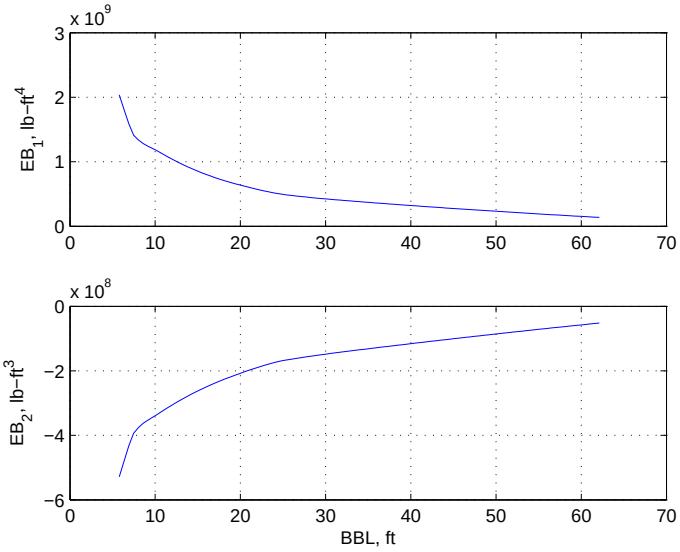

Figure 5.4 - Estimated Wing Bending-Torsion Coupling Stiffness

The wing is modeled as a thin-walled shell structure for which the section properties are computed. The Young's modulus and shear modulus are then adjusted by trial and error until the desired wing tip deflection is obtained. The distributions of the wing structural stiffness characteristics are plotted in Figures 5.2 and 5.3.

5.4 Aeroelastic Angle of Attack

The relative velocity of the air approaching a wing section includes the contribution from the wing structural deflection that results in changes in the local angle of attack. Since aerodynamic forces and moments are dependent on the local angle of attack, the wing structural deflection will generate additional elastic forces and moments. The local angle of attack depends on the relative approaching air velocity as well as the rotation angle ϕ from Eq. (5.4). The relative air velocity in turn also depends on a structural-deflection induced velocity. The local velocity components at point Q in the reference frame D are given by

$$\begin{bmatrix} v_x \\ v_y \\ v_z \end{bmatrix} = \begin{bmatrix} -u\sin\Lambda + x_{1,t} \\ -u\cos\Lambda + y_{1,t} \\ -w - qx_a + z_{1,t} \end{bmatrix} = \begin{bmatrix} -u\sin\Lambda - zW_{xt} \\ -u\cos\Lambda - z\Theta_t \\ -w - qx_a + W_t + y\Theta_t \end{bmatrix} \tag{5.14}$$

where $u \approx V_\infty$, $w \approx V_\infty \alpha$, q is the aircraft pitch rate, x_a is the position of point Q with respect to the aircraft C.G. (positive aft of C.G.) measured in the aircraft stability reference frame B, and y and z are coordinates of point Q in the reference frame D.

In order to compute the aeroelastic forces and moments, the velocity must be transformed from the reference frame D to the airfoil local coordinate reference frame defined by (μ, η, ξ) (see Figure 5.2). Then the transformation can be performed using two successive rotation matrix multiplication operations as

$$\begin{bmatrix} v_\mu \\ v_\eta \\ v_\xi \end{bmatrix} = \begin{bmatrix} 1 & 0 & 0 \\ 0 & 1 & \Theta+\gamma \\ 0 & -(\Theta+\gamma) & 1 \end{bmatrix} \begin{bmatrix} 1 & 0 & W_x \\ 0 & 1 & 0 \\ -W_x & 0 & 1 \end{bmatrix} \begin{bmatrix} v_x \\ v_y \\ v_z \end{bmatrix} = \begin{bmatrix} v_x + W_x v_z \\ v_y + (\Theta+\gamma)(v_z - W_x v_x) \\ v_z - W_x v_x - (\Theta+\gamma) v_y \end{bmatrix} \tag{5.15}$$

Referring to Figure 5.5, the local aeroelastic angle of attack on the airfoil section is due to the velocity components v_η and v_ξ and is computed as

$$\alpha_c = \frac{v_\xi}{v_\eta} \tag{5.16}$$

where

$$v_\xi \approx w + qx_a - W_t - y\Theta_t - W_x u\sin\Lambda - (\Theta+\gamma)\, u\cos\Lambda \tag{5.17}$$

$$v_\eta \approx u\cos\Lambda \tag{5.18}$$

Thus, the local aeroelastic angle of attack becomes[14]

$$\alpha_c(x) = \frac{\alpha}{\cos\Lambda} + \frac{qx_a}{V_\infty\cos\Lambda} - \gamma(x) - W_x\tan\Lambda - \Theta - \frac{W_t + y\Theta_t}{V_\infty\cos\Lambda} \tag{5.19}$$

The terms W_t and Θ_t contribute to aerodynamic damping forces which can be significant for aeroelastic stability.

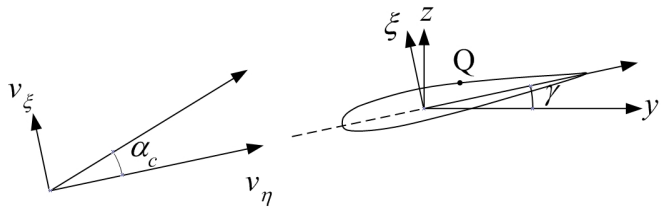

Figure 5.5 - Aeroelastic Angle of Attack

There are two methods for aeroelastic analysis. The steady state aerodynamic method assumes that the steady state lift circulation occurs at the aerodynamic center of the oscillating airfoil, which is usually at the quarter-point. On the other hand, the Theodorsen's aeroelasticity theory assumes unsteady aerodynamics which results in an unsteady circulation at the $3/4$-chord point[14]. In this study, the first method is used. The local angle of attack of an airfoil section is then given by

$$\alpha_c(x) = \frac{\alpha}{\cos\Lambda} + \frac{qx_{ac}}{V_\infty \cos\Lambda} - \gamma(x) - W_x \tan\Lambda - \Theta - \frac{W_t - e\Theta_t}{V_\infty \cos\Lambda} \tag{5.20}$$

where x_{ac} is the distance from aircraft C.G. to the quarter-chord point measured in aircraft stability reference frame (positive aft of C.G.) and e is the distance between the quarter-chord point and the elastic axis.

It is noted that by setting $q = W_t = \Theta_t = 0$, the static aeroelastic angle of attack is the same as the previous expression in Eq. (2.15) as discussed in connection with the explanation of the drooped wing shape in Section 2.5.1.

5.5 Wing Aeroelasticity

The wing shape is comprised of two components: bending deflection $W(x)$ and torsional deflection $\Theta(x)$, where x is the wing local elastic axis. Furthermore, these deflections include both the static and dynamic contributions. Thus

$$W(x,t) = \bar{W}(x) + \Delta W(x,t) \tag{5.21}$$

$$\Theta(x,t) = \bar{\Theta}(x) + \Delta\Theta(x,t) \tag{5.22}$$

where $\bar{W}(x)$ and $\bar{\Theta}(x)$ are the static deflections, and $\Delta W(x,t)$ and $\Delta\Theta(x,t)$ are the dynamic deflections.

The static bending and torsional deflections are achieved by wing-shaping control flaps and are given by

$$\bar{W}(x) = W_f \bar{f} \tag{5.23}$$

$$\bar{\Theta}(x) = \Theta_f \bar{f} \tag{5.24}$$

where $W_f = \begin{bmatrix} W_{f_1} & W_{f_2} & \dots & W_{f_{12}} \end{bmatrix}$ is the bending deflection derivative due to the flap deflections,
$\Theta_f = \begin{bmatrix} \Theta_{f_1} & \Theta_{f_2} & \dots & \Theta_{f_{12}} \end{bmatrix}$ is the torsional deflection derivative due to the flap deflections, and
$f = \begin{bmatrix} f_1 & f_2 & \dots & f_6 & s_1 & s_2 & \dots & s_6 \end{bmatrix}^\top$ are the flap and slat deflections.

The force and moment equilibrium conditions for bending and torsion are expressed as

$$\frac{\partial M_x}{\partial x} = -m_x \tag{5.25}$$

$$\frac{\partial^2 M_y}{\partial x^2} = f_z - \frac{\partial m_y}{\partial x} \tag{5.26}$$

where m_x is the pitching moment per unit span about the elastic axis, f_z is the lift force per unit span, and m_y is the bending moment per unit span about the flapwise axis of the wing which is assumed to be zero.

The local pitching moment and lift coefficients are given by

$$c_m(x) = \bar{c}_m + c_{m_\alpha}\alpha_c(x) + \frac{e}{c}\left[\bar{c}_L + c_{L_\alpha}\alpha_c(x)\right] + \left(c_{m_f} + \frac{e}{c}c_{L_f}\right) f \tag{5.27}$$

$$c_L(x) = \bar{c}_L + c_{L_\alpha}\alpha_c(x) + c_{L_f} f \tag{5.28}$$

where $\bar{c}_m$ is the section pitching moment coefficient about the section at the quarter-chord point at trim which is usually small and thus may be assumed to be zero, c_{m_α} is the section pitching moment vs. alpha curve slope which is zero at the quarter-chord point, c_{m_f} is the section pitching moment control derivative due to the flaps and slats which is assumed to be zero, $\bar{c}_L$ is the section lift coefficient at trim, $c_{L\alpha}$ is the section lift vs. angle of attack curve slope, c_{L_f} is the section lift control derivative due to the flaps and slats, e is the distance between the quarter-chord point and the elastic axis, and c is the section chord.

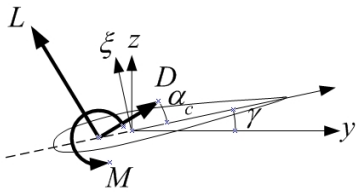

Figure 5.6 - Airfoil Forces and Moment

Using the sign convention as shown in Figure 5.6, the pitching moment per unit span can now be expressed as

$$m_x = -\left[\bar{c}_L + c_{L_\alpha}\left(\frac{\alpha}{\cos\Lambda} + \frac{qx_{ac}}{V_\infty \cos\Lambda} - \gamma - W_x \tan\Lambda - \Theta - \frac{W_t - e\Theta_t}{V_\infty \cos\Lambda}\right) + c_{L_f} f\right] eq_\infty \cos^2\Lambda c - \rho I_{xx}\Theta_{tt} \tag{5.29}$$

where q_∞ is the dynamic pressure, ρ is the wing material density including fuel density, and I_{xx} is the section polar area moment of inertia, and the term $\cos^2\Lambda$ comes from the fact the velocity component normal to the wing leading edge is reduced by a factor of $\cos\Lambda$.

The lift force per unit span is given by

$$f_z = \left[\bar{c}_L + c_{L_\alpha}\left(\frac{\alpha}{\cos\Lambda} + \frac{qx_{ac}}{V_\infty \cos\Lambda} - \gamma - W_x \tan\Lambda - \Theta - \frac{W_t - e\Theta_t}{V_\infty \cos\Lambda}\right) + c_{L_f} f\right] q_\infty \cos^2\Lambda c - \rho g A - \rho A W_{tt} \tag{5.30}$$

where A is the cross sectional area of a wing section.

The aeroservoelastic bending and torsional equations then become

$$\frac{\partial}{\partial x}\left\{\left[GJ + EB_1\left(\gamma'\right)^2\right]\Theta_x - EB_2\gamma' W_{xx}\right\} = \left[\bar{c}_L + c_{L_\alpha}\left(\frac{\alpha}{\cos\Lambda} + \frac{qx_{ac}}{V_\infty \cos\Lambda} - \gamma - W_x \tan\Lambda - \Theta - \frac{W_t - e\Theta_t}{V_\infty \cos\Lambda}\right) + c_{L_f} f\right] eq_\infty \cos^2\Lambda c + \rho I_{xx}\Theta_{tt} \tag{5.31}$$

$$\frac{\partial^2}{\partial x^2}\left(-EB_2\gamma'\Theta_x + EI_{yy}W_{xx}\right) = \left[\bar{c}_L + c_{L_\alpha}\left(\frac{\alpha}{\cos\Lambda} + \frac{qx_{ac}}{V_\infty \cos\Lambda} - \gamma - W_x \tan\Lambda - \Theta - \frac{W_t - e\Theta_t}{V_\infty \cos\Lambda}\right) + c_{L_f} f\right] q_\infty \cos^2\Lambda c - \rho g A - \rho A W_{tt} \tag{5.32}$$

subject to fixed-end symmetric-mode boundary conditions $\Theta(0,t) = \Theta_x(L,t) = 0$ and $W(0,t) = W_x(0,t) = EIW_{xx}(L,t) = \frac{d}{dx}(EIW_{xx}(L,t)) = 0$, whereupon the x-coordinate of the wing elastic axis is translated such that the wing root section is at $x = 0$ and wing tip section is at $x = L$.

These equations describe the wing bending and torsion deflections due to aerodynamic forces and moments. Using the Galerkin's method [13], the bending and torsional deflections can be approximated by the method of separation of variables as

$$\Theta(x,t) = \theta(t)\Psi(x) \tag{5.33}$$

$$W(x,t) = w(t)\Phi(x) \tag{5.34}$$

where $\theta(t)$ and $w(t)$ are the generalized coordinates and $\Psi(x)$ and $\Phi(x)$ are the assumed normalized modes which are given by

$$\Psi(x) = \sqrt{2}\sin\frac{\pi x}{2L} \tag{5.35}$$

$$\Phi(x) = \cosh(\beta_1 x) - \cos(\beta_1 x) - \frac{\cosh(\beta_1 L) + \cos(\beta_1 L)}{\sinh(\beta_1 L) + \sin(\beta_1 L)}\left[\sinh(\beta_1 x) - \sin(\beta_1 x)\right] \tag{5.36}$$

where $\beta_1 L = 1.8751$ is the eigenvalue of the first bending mode of a uniform cantilever beam, and the mode shapes $\Psi(x)$ and $\Phi(x)$ satisfy the normalization condition

$$\int_0^L \Psi^2 dx = \int_0^L \Phi^2 dx = L \tag{5.37}$$

The weak-form integral expressions of the aeroelastic equations are obtained by multiplying the torsional and bending equations by $\Psi(x)$ and $\Phi(x)$ and then integrating over the wing span. This yields

$$\int_0^L \Psi \frac{d}{dx}\left\{\left[GJ+EB_1\left(\gamma'\right)^2\right]\theta\Psi' - EB_2\gamma' w\Phi''\right\}dx = \int_0^L \Psi\left[\bar{c}_L + c_{L_\alpha}\left(\frac{\alpha}{\cos\Lambda}+\frac{qx_{ac}}{V_\infty\cos\Lambda}-\gamma-w\Phi'\tan\Lambda-\theta\Psi-\frac{\dot{w}\Phi-e\dot{\theta}\Psi}{V_\infty\cos\Lambda}\right)+c_{L_f}f\right]eq_\infty\cos^2\Lambda c dx + \int_0^L \Psi\rho I_{xx}\ddot{\theta}\Psi dx \quad (5.38)$$

$$\int_0^L \Phi\frac{d^2}{dx^2}\left(-EB_2\gamma'\theta\Psi' + EI_{yy}w\Phi''\right)dx = \int_0^L \Phi\left[\bar{c}_L + c_{L_\alpha}\left(\frac{\alpha}{\cos\Lambda}+\frac{qx_{ac}}{V_\infty\cos\Lambda}-\gamma-w\Phi'\tan\Lambda-\theta\Psi-\frac{\dot{w}\Phi-e\dot{\theta}\Psi}{V_\infty\cos\Lambda}\right)+c_{L_f}f\right]q_\infty\cos^2\Lambda c dx - \int_0^L \Phi\rho g A dx - \int_0^L \Phi\rho A\ddot{w}\Phi dx \quad (5.39)$$

The expressions of the left hand sides can be integrated by parts as

$$\int_0^L \Psi\frac{d}{dx}\left\{\left[GJ+EB_1\left(\gamma'\right)^2\right]\theta\Psi' - EB_2\gamma' w\Phi''\right\}dx = \Psi\left\{\left[GJ+EB_1\left(\gamma'\right)^2\right]\theta\Psi' - EB_2\gamma' w\Phi''\right\}\Big|_0^L - \int_0^L\left\{\left[GJ+EB_1\left(\gamma'\right)^2\right]\theta\left(\Psi'\right)^2 - EB_2\gamma' w\Psi'\Phi''\right\}dx \quad (5.40)$$

$$\int_0^L \Phi\frac{d^2}{dx^2}\left(-EB_2\gamma'\theta\Psi' + EI_{yy}w\Phi''\right)dx = \Phi\frac{d}{dx}\left(-EB_2\gamma'\theta\Psi' + EI_{yy}w\Phi''\right)\Big|_0^L - \Phi'\left(-EB_2\gamma'\theta\Psi' + EI_{yy}w\Phi''\right)\Big|_0^L + \int_0^L \Phi''\left(-EB_2\gamma'\theta\Psi' + EI_{yy}w\Phi''\right)dx \quad (5.41)$$

Then, by enforcing the zero boundary conditions at the two end points, the weak-form aeroelastic equations are obtained as

$$\int_0^L\left\{\left[GJ+EB_1\left(\gamma'\right)^2\right]\theta\left(\Psi'\right)^2 - EB_2\gamma' w\Psi'\Phi''\right\}dx + \int_0^L \Psi\left[\bar{c}_L + c_{L_\alpha}\left(\frac{\alpha}{\cos\Lambda}+\frac{qx_{ac}}{V_\infty\cos\Lambda}-\gamma-w\Phi'\tan\Lambda-\theta\Psi-\frac{\dot{w}\Phi-e\dot{\theta}\Psi}{V_\infty\cos\Lambda}\right)+c_{L_f}f\right]eq_\infty\cos^2\Lambda c dx + \int_0^L \Psi\rho I_{xx}\ddot{\theta}\Psi dx = 0 \quad (5.42)$$

$$\int_0^L \Phi''\left(-EB_2\gamma'\theta\Psi' + EI_{yy}w\Phi''\right)dx - \int_0^L \Phi\left[\bar{c}_L + c_{L_\alpha}\left(\frac{\alpha}{\cos\Lambda}+\frac{qx_{ac}}{V_\infty\cos\Lambda}-\gamma-w\Phi'\tan\Lambda-\theta\Psi-\frac{\dot{w}\Phi-e\dot{\theta}\Psi}{V_\infty\cos\Lambda}\right)+c_{L_f}f\right]q_\infty\cos^2\Lambda c dx + \int_0^L \Phi\rho g A dx + \int_0^L \Phi\rho A\ddot{w}\Phi dx = 0 \quad (5.43)$$

These equations are then expressed in a matrix form as

$$\begin{bmatrix} m_{ww} & 0 \\ 0 & m_{\theta\theta} \end{bmatrix}\begin{bmatrix} \ddot{w} \\ \ddot{\theta} \end{bmatrix}+\begin{bmatrix} c_{ww} & c_{w\theta} \\ c_{\theta w} & c_{\theta\theta} \end{bmatrix}\begin{bmatrix} \dot{w} \\ \dot{\theta} \end{bmatrix}+\begin{bmatrix} k_{ww} & k_{w\theta} \\ k_{\theta w} & k_{\theta\theta} \end{bmatrix}\begin{bmatrix} w \\ \theta \end{bmatrix} + \begin{bmatrix} h_{w\alpha} & h_{wq} \\ h_{\theta\alpha} & h_{\theta q} \end{bmatrix}\begin{bmatrix} \alpha \\ q \end{bmatrix}=\begin{bmatrix} f_w \\ f_\theta \end{bmatrix}+\begin{bmatrix} g_w \\ g_\theta \end{bmatrix} f \quad (5.44)$$

or

$$M\ddot{x}_e + C\dot{x}_e + Kx_e + Hx_r = F + Gf \quad (5.45)$$

where $x_e = \begin{bmatrix} w & \theta \end{bmatrix}^\top$, $x_r = \begin{bmatrix} \alpha & q \end{bmatrix}^\top$, M is the generalized mass matrix, C is the generalized aerodynamic damping matrix, K is the generalized stiffness, H is the generalized aerodynamic coupling matrix, F is the generalized force vector, and G is the generalized force derivative vector due to the flap and slat deflections.

These matrices are evaluated as

$$M = \rho\int_0^L \begin{bmatrix} A\Phi^2 & 0 \\ 0 & I_{xx}\Psi^2 \end{bmatrix} dx \quad (5.46)$$

$$C = \frac{q_\infty c_{L_\alpha}}{V_\infty}\int_0^L \begin{bmatrix} \cos\Lambda_c\Phi^2 & -e\cos\Lambda_c\Psi\Phi \\ -e\cos\Lambda_c\Psi\Phi & e^2\cos\Lambda_c\Psi^2 \end{bmatrix} dx \quad (5.47)$$

$$K = \int_0^L \begin{bmatrix} EI_{yy}\left(\Phi''\right)^2 + q_\infty c_{L_\alpha}\tan\Lambda\cos^2\Lambda_c\Phi\Phi' & -EB_2\gamma'\Psi'\Phi'' + q_\infty c_{L_\alpha}\cos^2\Lambda_c\Psi\Phi \\ -EB_2\gamma'\Psi'\Phi'' - q_\infty c_{L_\alpha} e\tan\Lambda\cos^2\Lambda_c\Psi\Phi' & \left[GJ + EB_1\left(\gamma'\right)^2\right]\left(\Psi'\right)^2 - q_\infty c_{L_\alpha} e\cos^2\Lambda_c\Psi^2 \end{bmatrix} dx \quad (5.48)$$

$$H = \frac{q_\infty c_{L_\alpha}}{V_\infty}\int_0^L \begin{bmatrix} -V_\infty\cos\Lambda_c\Phi & -x_{ac}\cos\Lambda_c\Phi \\ V_\infty e\cos\Lambda_c\Psi & x_{ac}e\cos\Lambda_c\Psi \end{bmatrix} dx \quad (5.49)$$

$$F = \int_0^L \begin{bmatrix} q_\infty\bar{c}_L\cos^2\Lambda_c\Phi + \Phi\rho gA \\ -q_\infty\bar{c}_L e\cos^2\Lambda_c\Psi \end{bmatrix} dx \quad (5.50)$$

$$G = q_\infty\int_0^L \begin{bmatrix} c_{L_f}\cos^2\Lambda_c\Phi \\ -c_{L_f} e\cos^2\Lambda_c\Psi \end{bmatrix} dx \quad (5.51)$$

A program has been developed in MATLAB based on this analysis for the study to analyze wing bending and torsional deflections and to design wing shaping control strategies for the drooped-wing aircraft concept.

Typical values of these matrices are given for the drooped-wing aircraft concept with 80% fuel in the tank.

$$M = 10^4\begin{bmatrix} 0.0863 & 0 \\ 0 & 2.0849 \end{bmatrix} \quad C = 10^4\begin{bmatrix} 0.1290 & -0.3479 \\ -0.3479 & 1.4643 \end{bmatrix} \quad K = 10^6\begin{bmatrix} 0.0209 & 0.9360 \\ -0.0610 & 3.0743 \end{bmatrix}$$

$$H = 10^6\begin{bmatrix} -0.9527 & -0.0264 \\ 4.2340 & 0.0909 \end{bmatrix} \quad F = 10^5\begin{bmatrix} 0.3001 \\ -1.9498 \end{bmatrix}$$

$$G = 10^5\begin{bmatrix} 0.0012 & 0.0249 & 0.1601 & 0.0269 & 0.2790 & 0.0298 \\ -0.0012 & -0.0334 & -0.3258 & -0.0787 & -1.2337 & -0.2137 \\ -0.0002 & 0.0249 & 0.1601 & 0.0269 & 0.2790 & 0.0298 \\ 0.0002 & 0.0044 & 0.0206 & 0.0062 & 0.0251 & 0.0061 \end{bmatrix}$$

5.5.1 Static Wing Deflection and Aeroelastically Tailored As-Built Wing Shape

The aeroservoelastic equation includes both the static and dynamic components of the bending and torsional deflections. The wing-shaping control flaps therefore also have both static and dynamic components. Let $\theta(t) = \bar{\theta} + \Delta\theta(t)$, $w(t) = \bar{w} + \Delta w(t)$, and $f(t) = \bar{f} + \Delta f(t)$. Then the static wing shaping control equation then is obtained as

$$\begin{bmatrix} k_{ww} & k_{w\theta} \\ k_{\theta w} & k_{\theta\theta} \end{bmatrix}\begin{bmatrix} \bar{w} \\ \bar{\theta} \end{bmatrix} = \begin{bmatrix} f_w \\ f_\theta \end{bmatrix} + \begin{bmatrix} g_\theta \\ g_w \end{bmatrix}\bar{f} \quad (5.52)$$

and the dynamic wing shaping control equation is given by

$$\begin{bmatrix} m_{ww} & 0 \\ 0 & m_{\theta\theta} \end{bmatrix} \begin{bmatrix} \Delta\ddot{w} \\ \Delta\ddot{\theta} \end{bmatrix} + \begin{bmatrix} c_{ww} & c_{w\theta} \\ c_{\theta w} & c_{\theta\theta} \end{bmatrix} \begin{bmatrix} \Delta\dot{w} \\ \Delta\dot{\theta} \end{bmatrix} + \begin{bmatrix} k_{ww} & k_{w\theta} \\ k_{\theta w} & k_{\theta\theta} \end{bmatrix} \begin{bmatrix} \Delta w \\ \Delta\theta \end{bmatrix} + \begin{bmatrix} h_{w\alpha} & h_{wq} \\ h_{\theta\alpha} & h_{\theta q} \end{bmatrix} \begin{bmatrix} \alpha \\ q \end{bmatrix} = \begin{bmatrix} g_w \\ g_\theta \end{bmatrix} \Delta f \quad (5.53)$$

The aircraft's optimal wing shape is designed to be maintained at all times during cruise by wing shaping control flaps and slats. To achieve a desired wing shape, the flap and slat must be deflected to change the aerodynamic forces and moments acting on the wing so as to cause the wing to deflect to the desired wing shape. To determine the flap deflection requirements, the static wing shaping control equation can be written for two difference wing shapes as

$$K_d\delta_d + H_d x_{r_d} = F + G\bar{f}_d \quad (5.54)$$

$$K\delta + Hx_r = F + G\bar{f} \quad (5.55)$$

where $\delta = \begin{bmatrix} \bar{w} & \bar{\theta} \end{bmatrix}^\top$ and the subscript d denotes the quantities associated with the desired wing shape.

Then subtracting these equations yields

$$K_d\delta_d - K\delta = G\Delta\bar{f} \quad (5.56)$$

Using a Moore-Penrose pseudo-inverse method, $\Delta\bar{f}$ can be computed as

$$\Delta\bar{f} = RG^\top \left(GRG^\top\right)^{-1} (K_d\delta_d - K\delta) \quad (5.57)$$

where $R > 0$ is a weighting matrix.

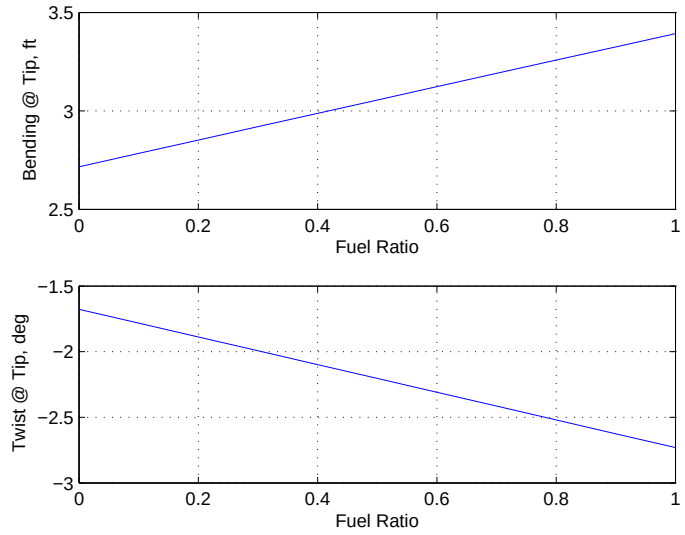

Figure 5.7 - Wing Tip Bending Deflection and Twist

The static wing bending and torsional deflections with and without wing shaping control are shown in Figures 3.2 and 3.3 in Section.3.2. The wing tip bending and torsion deflections as a function of fuel burn is shown in Figure 5.7. It can be seen that the wing tip bending and torsional deflections decrease linearly with fuel burn. The deflections are maximum with the fuel tank full. The 50% fuel point is where the wing shape reaches its optimal drooped wing shape under the 1-g loading. Thus, the as-built wing shape would have an additional negative downward bending deflection of 3.0554 ft and an additional positive nose-down twist of 2.2040°. This aeroelastic tailoring allows the as-built wing shape to take on the desired wing shape in-flight under aerodynamic loading. The optimal and as-built drooped wing shape and twist are shown in Figures 5.8 and 5.9.

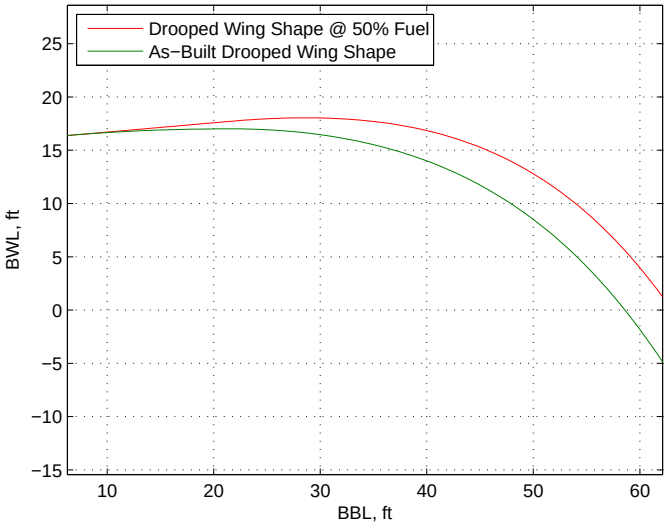

Figure 5.8 - Optimal and As-Built Drooped Wing Shapes

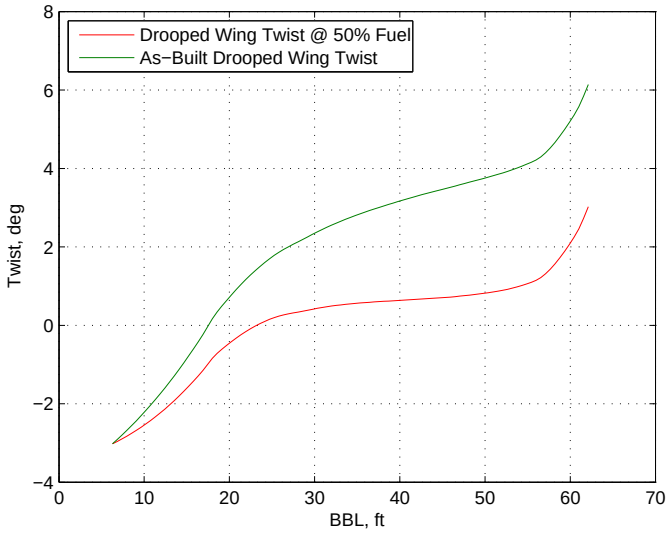

Figure 5.9 - Optimal and As-Built Drooped Wing Twists

5.5.2 Aeroelastic Modal Frequency and Damping

Aeroelastic instability resulting in flutter can be encountered if the damping of aeroelastic modes become negative. Structural damping is incorporated into the dynamic wing shaping control equation by adding the following structural damping matrix

$$C_s = 2\zeta MX\Omega X^{-1} \tag{5.58}$$

where $\zeta = 0.1$ is the structural damping ratio, X is the eigenfunction of the eigenvalue problem

$$M^{-1}Kx_e = \lambda x_e \tag{5.59}$$

and $\Omega = \text{diag}(\omega_1, \omega_2)$ is the diagonal matrix of the natural frequencies of the first bending (1T) and first torsion (1T) modes.

The aeroelastic modal frequencies and damping are then obtained by solving the following eigenvalue problem

$$\begin{bmatrix} -M^{-1}(C+C_s) & -M^{-1}K \\ I & 0 \end{bmatrix} \begin{bmatrix} \dot{x}_e \\ x_e \end{bmatrix} = \lambda \begin{bmatrix} \dot{x}_e \\ x_e \end{bmatrix} \tag{5.60}$$

The computed frequencies and damping ratios of the 1B and 1T modes for the drooped-wing aircraft concept with 80% fuel in the tank are shown in Table 5.1.

	Frequency, rad/sec	Damping Ratio
Mode 1B	7.3183	0.3718
Mode 1T	11.2201	0.0188

Table 5.1 - Aeroelastic Modal Frequency and Damping

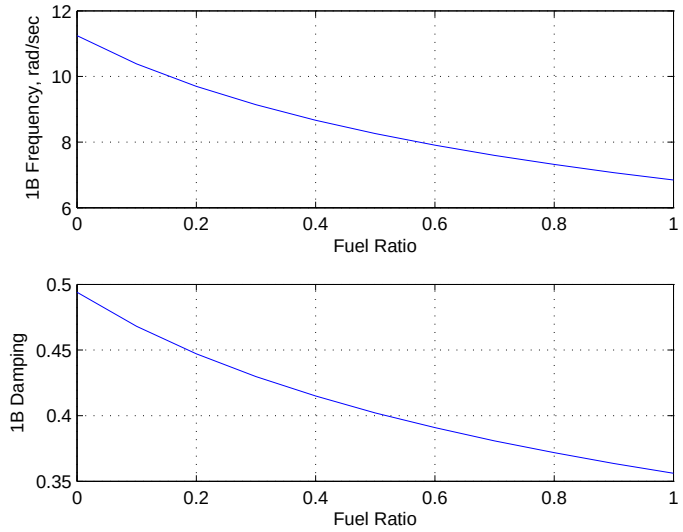

Figure 5.10 - Frequency and Damping of Mode 1B

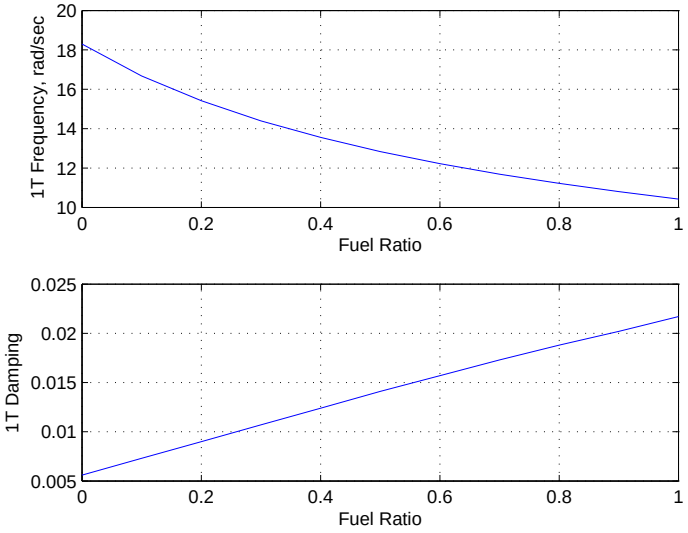

Figure 5.11 - Frequency and Damping of Mode 1T

The damping ratios are all positive which indicate that the aerolastic modes are stable. The frequencies and damping ratios of the 1B and 1T modes as a function of fuel burn are as shown in Figures 5.10 and 5.11. Generally, the frequency increases as fuel is burned since the frequency is inversely proportional to the square root of the generalized mass. The damping ratio of mode 1B increases with fuel burn but the damping ratio of mode 1T decreases with fuel burn. The low damping ratio of the torsion mode can be a problem for aircraft stability. Active feedback control can potentially help improve the stability margin of aeroelastic modes.

5.6 Aeroelastic Longitudinal Flight Dynamics

Assuming that c_{L_0} and c_{L_α} are the same for all airfoil sections by neglecting the effects of camber and thickness distribution of the wing airfoil sections, and also assuming a zero lift contribution from the fuselage. Then the aircraft lift coefficient is computed as

$$C_L = \frac{2\int_0^L c_L q_\infty \cos^2\Lambda c dx}{q_\infty S} = \frac{2}{S}\int_0^L \left[\bar{c}_L + c_{L_\alpha}\left(\frac{\alpha}{\cos\Lambda} - \gamma - w\Phi' \tan\Lambda - \theta\Psi - \frac{\dot{w}\Phi - e\dot{\theta}\Psi}{V_\infty \cos\Lambda}\right) + c_{L_f} f\right]\cos^2\Lambda c dx \tag{5.61}$$

The lift coefficient can be expressed in terms of various lift derivatives as

$$C_L = \bar{C}_L + C_{L_\alpha}\alpha + C_{L_\theta}\theta + C_{L_w} w + C_{L_{\dot{\theta}}}\dot{\theta} + C_{L_{\dot{w}}}\dot{w} + C_{L_f} f \tag{5.62}$$

where

$$\bar{C}_L = \frac{2}{S}\int_0^L (\bar{c}_L - c_{L_\alpha}\gamma)\cos^2\Lambda c dx \tag{5.63}$$

$$C_{L_\alpha} = \frac{2c_{L_\alpha}}{S}\int_0^L \cos\Lambda c dx \tag{5.64}$$

$$C_{L_\theta} = -\frac{2c_{L_\alpha}}{S}\int_0^L \cos^2\Lambda c\Psi dx \tag{5.65}$$

$$C_{L_w} = -\frac{2c_{L_\alpha}}{S}\int_0^L \tan\Lambda\cos^2\Lambda c\Phi' dx \tag{5.66}$$

$$C_{L_{\dot{\theta}}} = \frac{2c_{L_\alpha}}{V_\infty S}\int_0^L e\cos\Lambda c\Psi dx \tag{5.67}$$

$$C_{L_{\dot{w}}} = -\frac{2c_{L_\alpha}}{V_\infty S}\int_0^L \cos\Lambda c\Phi dx \tag{5.68}$$

$$C_{L_f} = \frac{2}{S}\int_0^L c_{L_f}\cos^2\Lambda c dx \tag{5.69}$$

Note that the lift coefficient is sensitive to the wing deflections as well as wing deflection velocities as evidenced by the terms C_{L_θ}, C_{L_w}, $C_{L_{\dot{\theta}}}$, and $C_{L_{\dot{w}}}$.

The wing deflection contribution to the pitching moment about aircraft C.G. is given by

$$\Delta M = -\int_0^L \Delta l x_{ac} dx \tag{5.70}$$

where Δl is the additional lift contribution due to the wing bending and torsional deflections.

Thus, the pitching moment coefficient is expressed in terms of various pitching moment coefficients as

$$C_m = \bar{C}_m + C_{m_\alpha}\alpha + C_{m_\theta}\theta + C_{m_w} w + C_{m_{\dot{\theta}}}\dot{\theta} + C_{m_{\dot{w}}}\dot{w} + C_{m_f} f \tag{5.71}$$

where

$$C_{m_\theta} = \frac{2c_{L_\alpha}}{S\bar{c}}\int_0^L x_{ac}\cos^2\Lambda c\Psi dx \tag{5.72}$$

$$C_{m_w} = \frac{2c_{L_\alpha}}{S\bar{c}}\int_0^L x_{ac}\tan\Lambda\cos^2\Lambda c\Phi' dx \tag{5.73}$$

$$C_{m_{\dot{\theta}}} = -\frac{2c_{L_\alpha}}{V_\infty S\bar{c}} \int_0^L x_{ac} e \cos\Lambda c \Psi dx \tag{5.74}$$

$$C_{m_{\dot{w}}} = \frac{2c_{L_\alpha}}{V_\infty S\bar{c}} \int_0^L x_{ac} \cos\Lambda c \Phi dx \tag{5.75}$$

The aircraft pitch rate dynamics are then described by

$$\frac{\bar{I}_{yy}}{q_\infty S\bar{c}}\dot{q} - \frac{C_{m_{\dot{\alpha}}}\bar{c}}{2V_\infty}\dot{\alpha} = \frac{C_{m_q}\bar{c}}{2V_\infty}q + C_{m_\alpha}\alpha + C_{m_\theta}\theta + C_{m_w}w + C_{m_{\dot{\theta}}}\dot{\theta} + C_{m_{\dot{w}}}\dot{w} + C_{m_{\delta_e}}\delta_e + C_{m_f}f \tag{5.76}$$

where q is the pitch rate.

The aircraft angle of attack dynamics are also described by

$$\left(\frac{mV_\infty}{q_\infty S} + \frac{C_{L_{\dot{\alpha}}}\bar{c}}{2V_\infty}\right)\dot{\alpha} = \left(\frac{mV_\infty}{q_\infty S} - \frac{C_{L_q}\bar{c}}{2V_\infty}\right)q - C_{L_\alpha}\alpha - C_{L_\theta}\theta - C_{L_w}w - C_{L_{\dot{\theta}}}\dot{\theta} - C_{L_{\dot{w}}}\dot{w} - C_{L_{\delta_e}}\delta_e - C_{L_f}f \tag{5.77}$$

where α is the incremental angle of attack from trim.

Let

$$m_{\alpha\alpha} = \frac{mV_\infty}{q_\infty S} + \frac{C_{L_{\dot{\alpha}}}\bar{c}}{2V_\infty} \tag{5.78}$$

$$m_{q\alpha} = -\frac{C_{m_{\dot{\alpha}}}\bar{c}}{2V_\infty} \tag{5.79}$$

$$m_{qq} = \frac{\bar{I}_{yy}}{q_\infty S\bar{c}} \tag{5.80}$$

then

$$\dot{\alpha} = -\frac{1}{m_{\alpha\alpha}}\left[C_{L_\alpha}\alpha + \left(\frac{C_{L_q}\bar{c}}{2V_\infty} - \frac{mV_\infty}{q_\infty S}\right)q + C_{L_\theta}\theta + C_{L_w}w + C_{L_{\dot{\theta}}}\dot{\theta} + C_{L_{\dot{w}}}\dot{w} + C_{L_{\delta_e}}\delta_e + C_{L_f}f\right] \tag{5.81}$$

$$\begin{aligned}\dot{q} = \frac{1}{m_{qq}}\Bigg\{&\left(C_{m_\alpha} + \frac{m_{q\alpha}}{m_{\alpha\alpha}}C_{L_\alpha}\right)\alpha + \left[\frac{C_{m_q}\bar{c}}{2V_\infty} + \frac{m_{q\alpha}}{m_{\alpha\alpha}}\left(\frac{C_{L_q}\bar{c}}{2V_\infty} - \frac{mV_\infty}{q_\infty S}\right)\right]q + \left(C_{m_\theta} + \frac{m_{q\alpha}}{m_{\alpha\alpha}}C_{L_\theta}\right)\theta + \left(C_{m_w} + \frac{m_{q\alpha}}{m_{\alpha\alpha}}C_{L_w}\right)w \\ &+ \left(C_{m_{\dot{\theta}}} + \frac{m_{q\alpha}}{m_{\alpha\alpha}}C_{L_{\dot{\theta}}}\right)\dot{\theta} + \left(C_{m_{\dot{w}}} + \frac{m_{q\alpha}}{m_{\alpha\alpha}}C_{L_{\dot{w}}}\right)\dot{w} + \left(C_{m_{\delta_e}} + \frac{m_{q\alpha}}{m_{\alpha\alpha}}C_{L_{\delta_e}}\right)\delta_e + \left(C_{m_f} + \frac{m_{q\alpha}}{m_{\alpha\alpha}}C_{L_f}\right)f\Bigg\}\end{aligned} \tag{5.82}$$

Thus, the coupled aeroelastic flight dynamic model for the elastically shaped aircraft can be expressed in the following state space form:

$$
\begin{bmatrix} \dot{\alpha} \\ \dot{q} \\ \dot{w} \\ \dot{\theta} \\ \ddot{w} \\ \ddot{\theta} \end{bmatrix} = \begin{bmatrix} -\frac{1}{m_{\alpha\alpha}} C_{L_\alpha} & \frac{1}{m_{\alpha\alpha}} \left(\frac{mV_\infty}{q_\infty S} - \frac{C_{L_q} \bar{c}}{2V_\infty} \right) & -\frac{1}{m_{\alpha\alpha}} C_{L_w} \\ \frac{1}{m_{qq}} \left(C_{m_\alpha} + \frac{m_{q\alpha}}{m_{\alpha\alpha}} C_{L_\alpha} \right) & \frac{1}{m_{qq}} \left[\frac{C_{m_q} \bar{c}}{2V_\infty} + \frac{m_{q\alpha}}{m_{\alpha\alpha}} \left(\frac{C_{L_q} \bar{c}}{2V_\infty} - \frac{mV_\infty}{q_\infty S} \right) \right] & \frac{1}{m_{qq}} \left(C_{m_w} + \frac{m_{q\alpha}}{m_{\alpha\alpha}} C_{L_w} \right) \\ 0 & 0 & 0 \\ 0 & 0 & 0 \\ -\frac{1}{m_{ww}} h_{w\alpha} & -\frac{1}{m_{ww}} h_{wq} & -\frac{1}{m_{ww}} k_{ww} \\ -\frac{1}{m_{\theta\theta}} h_{\theta\alpha} & -\frac{1}{m_{\theta\theta}} h_{\theta q} & -\frac{1}{m_{\theta\theta}} k_{\theta w} \end{bmatrix}
$$

$$
+ \begin{bmatrix} -\frac{1}{m_{\alpha\alpha}} C_{L_\theta} & -\frac{1}{m_{\alpha\alpha}} C_{L_{\dot{w}}} & -\frac{1}{m_{\alpha\alpha}} C_{L_{\dot{\theta}}} \\ \frac{1}{m_{qq}} \left(C_{m_\theta} + \frac{m_{q\alpha}}{m_{\alpha\alpha}} C_{L_\theta} \right) & \frac{1}{m_{qq}} \left(C_{m_{\dot{\theta}}} + \frac{m_{q\alpha}}{m_{\alpha\alpha}} C_{L_{\dot{\theta}}} \right) & \frac{1}{m_{qq}} \left(C_{m_{\dot{w}}} + \frac{m_{q\alpha}}{m_{\alpha\alpha}} C_{L_{\dot{w}}} \right) \\ 0 & 1 & 0 \\ 0 & 0 & 1 \\ -\frac{1}{m_{ww}} k_{w\theta} & -\frac{1}{m_{ww}} c_{ww} & -\frac{1}{m_{ww}} c_{w\theta} \\ -\frac{1}{m_{\theta\theta}} k_{\theta\theta} & -\frac{1}{m_{\theta\theta}} c_{\theta w} & -\frac{1}{m_{\theta\theta}} c_{\theta\theta} \end{bmatrix} \begin{bmatrix} \alpha \\ q \\ w \\ \theta \\ \dot{w} \\ \dot{\theta} \end{bmatrix}
$$

$$
+ \begin{bmatrix} -\frac{1}{m_{\alpha\alpha}} C_{L_{\delta_e}} & -\frac{1}{m_{\alpha\alpha}} C_{L_f} \\ \frac{1}{m_{qq}} \left(C_{m_{\delta_e}} + \frac{m_{q\alpha}}{m_{\alpha\alpha}} C_{L_{\delta_e}} \right) & \frac{1}{m_{qq}} \left(C_{m_f} + \frac{m_{q\alpha}}{m_{\alpha\alpha}} C_{L_f} \right) \\ 0 & 0 \\ 0 & 0 \\ C_{m_{\delta_e}} & C_{m_f} \\ -C_{L_{\delta_e}} & -C_{L_f} \end{bmatrix} \begin{bmatrix} \delta_e \\ f \end{bmatrix} \tag{5.83}
$$

For the configuration with 80% fuel in the tank, the A matrix is given by

$$
A = \begin{bmatrix} -7.3750 \times 10^{-1} & 9.6851 \times 10^{-1} & 1.1604 \times 10^{-2} & 4.6906 \times 10^{-1} & 5.0282 \times 10^{-4} & -2.2347 \times 10^{-3} \\ -2.4727 \times 10^{0} & -9.1566 \times 10^{-1} & 1.7524 \times 10^{-1} & 7.3954 \times 10^{0} & 9.1129 \times 10^{-3} & -3.1127 \times 10^{-2} \\ 0 & 0 & 0 & 0 & 1 & 0 \\ 0 & 0 & 0 & 0 & 0 & 1 \\ 1.1038 \times 10^{3} & 3.0645 \times 10^{1} & -2.4219 \times 10^{1} & -1.0845 \times 10^{3} & -2.6554 \times 10^{0} & -7.8038 \times 10^{0} \\ -2.0307 \times 10^{2} & -4.3609 \times 10^{0} & 2.9241 \times 10^{0} & -1.4745 \times 10^{2} & 1.9877 \times 10^{-1} & -3.2075 \times 10^{0} \end{bmatrix}
$$

The eigenvalues of the rigid aircraft's short period mode can be computed from the 2 by 2 upper left matrix partition. These eigenvalues are stable

$$\lambda_{SP} = -0.8266 \pm 1.5450i$$

The eigenvalues of the 4 by 4 lower right matrix partition are for the 1B and 1T modes which are also stable

$$\lambda_{1B} = -2.7208 \pm 6.7937i$$

$$\lambda_{1T} = -0.2106 \pm 11.2181i$$

However, the eigenvalues of the elastic aircraft are unstable as seen below

$$\lambda_1 = -2.5552$$

$$\lambda_2 = 1.5214$$

$$\lambda_{1B} = -4.0078 \pm 7.4363i$$

$$\lambda_{1T} = 0.7667 \pm 11.4283i$$

Thus, this aircraft concept is marginally unstable due to the low damping of the torsion mode. To increase the stability margin of the 1T mode, feedback control would be needed. This study raises an interesting observation with respect to a trade-off between the desire of having light-weight flexible structures for weight savings and the need for maintaining aeroelastic stability margin. Future work should address this trade-off in a comprehensive manner.

6 Flight Control Design

Flight control design is an integral part of aircraft design. A typical flight control design usually takes into account different sets of requirements for performance and stability that must be considered during a design process. Performance in the context of flight control implies the ability for a flight control system to follow a pilot command. However, in this study, a new notion of aerodynamic performance is introduced into the flight control framework. The goal of the new vehicle is to achieve low drag through active wing shaping control actuation. Thus, drag penalty due to the wing shaping control flap and slat deflections should be considered in a flight control design. Hence, a new concept of multi-objective flight control is proposed to not only achieve a pilot command following objective but also a drag minimization objective.

Stability is of paramount importance for any flight vehicle. Structural flexibility of airframes including wings can cause significant aeroelastic interactions that can degrade vehicle stability margins, potentially leading to loss of control. There exists a trade-off between the desire of having light weight, flexible structures for weight savings and the need for maintaining sufficient robust stability margins from aeroelastic instability. In this study, as can be seen, the overall aircraft is marginally unstable due to low damping ratio of the 1T mode. Thus, a flight control system must be able to stabilize aeroelastic modes. The wing shaping control flap and slat systems thus can be used to achieve this objective. Clearly, it is generally not desirable to operate an unstable vehicle. Thus, in practice, aeroelastic tailoring in the design process can be used to increase aerodynamic and structural damping. Then, the role of a flight control system would be relegated to stability augmentation as opposed to a more demanding task of stabilization. This is acceptable in the current practices as there are many stability augmentation controllers such as yaw dampers in use to provide desired damping characteristics to meet pilot handling quality requirements.

Another objective of a flight control design is to derive requirements for flight control frequency bandwidth and dynamic amplitudes of control surfaces for proper actuation sizing. In Section 3, Boeing Research and Technology has developed actuation system analysis for the wing shaping control flap and slat systems strictly from static deflection requirements. As the wing shaping control surfaces are used for both static wing shaping control as well as for stability augmentation or stabilization, the dynamic deflection requirements for the wing shaping control flap and slat systems should be added to the static deflection requirements to define the overall actuation system design requirements.

In the study, the focus is on outlining the multi-objective flight control framework. Simulations are performed using the standard optimal control method to demonstrate the feasibility of stabilizing the unstable 1T mode while tracking the angle of attack command. Dynamic deflection requirements are not considered due to time constraints. As part of a follow-on study, this effort along with a more detailed development of the multi-objective flight control for wing shaping control should be pursued.

6.1 Multi-Objective Optimal Flight Control for Drag Minimization

Because of the presence of potential structural mode interactions that can compromise aircraft stability, feedback flight control can be used to stabilize aeroelastic modes. Consider the state space representation of the aeroservoelastic flight dynamic model

$$\dot{x} = Ax + Bu \tag{6.1}$$

where $x = \begin{bmatrix} \alpha & q & w & \theta & \dot{w} & \dot{\theta} \end{bmatrix}^\top$ is a state vector and $u = \begin{bmatrix} \delta_e & f \end{bmatrix}$ is a control vector, assuming that all the states and control inputs are accessible.

Consider a flight control design to follow a desired angle of attack in-flight. Let $z = \int_0^t \Delta\alpha d\tau$ be an integral error state of the angle of attack, where $\Delta\alpha = \alpha - \alpha_c$ is the error between the angle of attack and its command signal. The augmented plant is expressed as

$$\begin{bmatrix} \dot{z} \\ \dot{x} \end{bmatrix} = \begin{bmatrix} 0 & I_\alpha \\ 0 & A \end{bmatrix} \begin{bmatrix} z \\ x \end{bmatrix} + \begin{bmatrix} 0 \\ B \end{bmatrix} u - \begin{bmatrix} \alpha_c \\ 0 \end{bmatrix} \tag{6.2}$$

where $I_\alpha = \begin{bmatrix} 1 & 0 & 0 & 0 & 0 & 0 \end{bmatrix}$.

Let $\bar{x} = \begin{bmatrix} z & \alpha & q & w & \theta & \dot{w} & \dot{\theta} \end{bmatrix}^\top$ be an augmented state vector. Then

$$\dot{\bar{x}} = \bar{A}\bar{x} + \bar{B}u - \bar{x}_c \tag{6.3}$$

$$\bar{A} = \begin{bmatrix} 0 & I_\alpha \\ 0 & A \end{bmatrix} \quad \bar{B} = \begin{bmatrix} 0 \\ B \end{bmatrix} \quad \bar{x}_c = -\begin{bmatrix} \alpha_c \\ 0 \end{bmatrix}$$

An optimal control is designed to minimize the following linear quadratic regulator (LQR) cost functional

$$J_1 = \frac{1}{2}\int_0^{t_f} \left(\bar{x}^\top Q\bar{x} + u^\top Ru\right) dt \tag{6.4}$$

where $Q = Q^\top \geq 0$ and $R = R^\top > 0$ are weighting matrices.

However, due to the drag penalty associated with the flap and slat deflections, the control objective must also attempt to minimize the drag penalty. Thus, a multi-objective optimal control problem is posed by imposing an additional cost functional for minimization

$$J_2 = \int_0^{t_f} \left|C_{D_f}\right| |f|\, dt \tag{6.5}$$

This is a mixed $\mathscr{L}_1$ and $\mathscr{L}_2$ optimal control problem whose solution must satisfy both the cost functionals simultaneously. The design is an iterative process whereby an optimal control is obtained using the LQR method. The cost functional J_2 is evaluated over the time interval, the control weighting matrices Q and R are then adjusted by some technique such as the gradient method to give a new set of control inputs. Thus, the goal is then to seek optimal weighting matrices Q and R that solve the multi-objective optimization problem. Due to the dimensionality of the weighting matrices Q and R and the time evolution of the solution which can be unstable, the optimization can be quite complex. Due to the time constraint, only the LQR problem is considered at this time. As a follow-on work, this multi-objective optimal control problem should be considered in the future.

For the $\mathscr{L}_2$ optimal control problem, the Hamiltonian of the system is given by

$$H = \frac{1}{2}\left(\bar{x}^\top Q\bar{x} + u^\top Ru\right) + \lambda^\top \left(\bar{A}\bar{x} + \bar{B}u - \bar{x}_c\right) \tag{6.6}$$

where λ is an adjoint state vector..

The optimality conditions are given by the adjoint equation

$$\dot{\lambda} = -\frac{\partial H^\top}{\partial \bar{x}} = -Q\bar{x} - \bar{A}^\top \lambda \tag{6.7}$$

and the optimal control

$$\frac{\partial H^\top}{\partial u} = Ru + \bar{B}^\top \lambda = 0 \tag{6.8}$$

To solve for these equations, the adjoint equation and the state equation must be solved simultaneously along with the optimal control. Let $\lambda = P\bar{x} + S\bar{x}_c$ be a solution of the optimality conditions. Then, the adjoint equation is obtained as

$$\dot{P}\bar{x} + P\left[\bar{A}\bar{x} - \bar{B}R^{-1}\bar{B}^\top \left(P\bar{x} + S\bar{x}_c\right) - \bar{x}_c\right] + \dot{S}\bar{x}_c + S\dot{\bar{x}}_c = -Q\bar{x} - \bar{A}^\top \left(P\bar{x} + S\bar{x}_c\right) \tag{6.9}$$

Let α_c be a step input so that $\dot{\alpha}_c = 0$. Let $t_f \to \infty$, then the optimal solution approaches a steady state solution. Therefore, $\dot{P}(0) = 0$ and $\dot{S}(0) = 0$. Then, separating terms yields the following expression

$$\left(P\bar{A} + \bar{A}^\top P - P\bar{B}R^{-1}\bar{B}^\top P + Q\right)\bar{x} + \left(-P\bar{B}R^{-1}\bar{B}^\top S - P + \bar{A}^\top S\right)\bar{x}_c = 0 \tag{6.10}$$

The optimal control is then obtained as

$$u = -K\bar{x} + K_c\bar{x}_c \tag{6.11}$$

where $K = R^{-1}\bar{B}^\top P$ is a feedback gain matrix, $K_c = -R^{-1}\bar{B}^\top S$ is a command feedforward gain matrix, and P and S are the steady state solutions of Eq. (6.10) given by

$$P\bar{A} + \bar{A}^\top P - P\bar{B}R^{-1}\bar{B}^\top P + Q = 0 \tag{6.12}$$

$$S = \left(\bar{A}^\top - P\bar{B}R^{-1}\bar{B}^\top\right)^{-1} P \tag{6.13}$$

6.2 Guidance Law

To minimize drag in cruise, the aircraft must schedule changes in its attitudes and wing configurations accordingly. As discussed earlier, for the remaining fuel above the half-way point, there is no need for static wing shaping control. However, wing shaping control flaps and slats must still be used for aeroelastic stability augmentation or stabilization. When the fuel falls below the half-way point, wing shaping control will be engaged continuously until the end of cruise. The angle of attack is also scheduled to change as the fuel is burned. Thus, a guidance law can be developed to schedule the angle of attack and the wing shaping control flaps and slats to engage as a function of the fuel weight.

For the purpose of the guidance law development, the variable camber continuous trailing edge flap system is assumed to be in used. It is further assumed that the incremental ΔC_{L_f} and ΔC_{D_f} are linearly varying with the flap deflections. Let W_f be the weight of the remaining fuel in the tank, which is assumed to be observable through a fuel gauge indicator. Then the weight of the aircraft at any point is the sum of the operational empty weight plus passengers and cargo and the fuel weight. This can be expressed as

$$W = W_e + W_f \tag{6.14}$$

where $W_e = 150,000$ lbs.

The angle of attack can be readily computed as

$$\alpha = \frac{1}{C_{L_\alpha}} \left(\frac{W_e + W_f}{q_\infty S} - C_{L_0} \right) \tag{6.15}$$

for $W_f \geq 0.5 W_{max} = 25,000$ lbs, where $W_{max} = 50,000$ lbs is the maximum fuel weight, $C_{L_0} = 0.1067$, $C_{L_\alpha} = 6.3451$/rad, and $q_\infty S = 549,313$ lbs.

When $W_f < 0.5 W_{max}$, wing shaping control flap is engaged. Then

$$C_{L_f} = C_L + \Delta C_{Lf} \tag{6.16}$$

where the incremental ΔC_{L_f} varies linearly with W_f as

$$\Delta C_{L_f} = -0.4376 \left(\frac{W_f}{W_{max}} - \frac{1}{2} \right) \tag{6.17}$$

So, if the angle of attack is held at a scheduled value for no flap, then the aircraft would have to increase in altitude as a result of increased lift, or conversely the angle of attack would have to be reduced in order to maintain the same altitude. Consider the guidance law for constant altitude cruise. The angle of attack schedule is given by

$$\alpha = \begin{cases} 1.5021 + \frac{W_f}{60,833} & 25,000 \leq W_f \leq 40,000 \\ -0.4736 + \frac{W_f}{10475} & 10,000 \leq W_f < 25,000 \end{cases} \tag{6.18}$$

The flap deflection varies linearly from 3.924^o at 20% fuel in the tank to 0^o at 50% fuel in the tank. So, the flap schedule is

$$f = \begin{cases} 0 & 25,000 \leq W_f \leq 40,000 \\ -13.08 \left(\frac{W_f}{50,000} - \frac{1}{2} \right) & 10,000 \leq W_f < 25,000 \end{cases} \tag{6.19}$$

Figure 6.1 shows the angle of attack and flap deflection schedules.

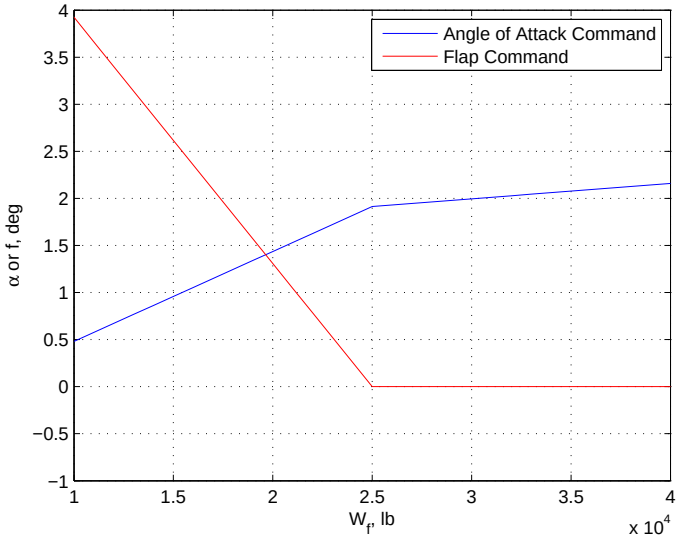

Figure 6.1 - Angle of Attack and Flap Deflection Schedules

6.3 Flight Control Simulation

Using the guidance developed, a flight control simulation is conducted to assess the abilities for the flight control system to track the angle of attack guidance law and, more importantly, to stabilize the unstable 1T mode. The simulation only uses the LQR optimal control. So drag minimization in the flight control is not considered. The standard flap and slat systems are used in the simulation instead of the variable camber continuous trailing edge flap system. The weighting matrices are chosen as $Q = \text{diag}\,(0.1, 0, 0.01, 0.01, 0.01, 0.01, 0.01)$ and $R = 0.1I$. The simulation time is chosen to be 4 hours of cruise time.

The angle of attack command is computed from the guidance law and then is filtered through a first-order filter to smooth out the command signal. The filtered angle of attack is computed as

$$\dot{\alpha}_c = -\lambda\,(\alpha_c - \alpha_g) \tag{6.20}$$

where α_g is the angle of attack obtained from the guidance law, and $\lambda = 2$.

Figure 6.2 is a plot of the aircraft angle of attack response for the first 50 sec. Figure 6.3 is a plot of the aircraft responses. The flight control design is able to stabilize the unstable 1T mode even though the aircraft is open-loop unstable. The maximum aileron deflection is about 8^{o}. Figures 6.4 and 6.5 are the plots of the wing shaping control flap and slat inputs. These flap and slat inputs are not optimized for drag minimization, so they are not necessarily the same as the required deflections developed in Section 3.2. The objective of the simulation is to demonstrate the capabilities of feedback control to stabilize aeroelastic instability and at the same time provide good command-following performance to achieve a desired guidance law.

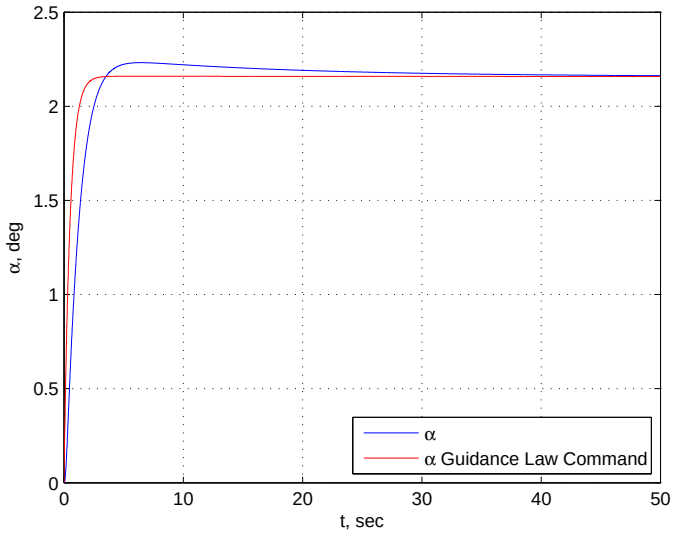

Figure 6.2 - Angle of Attack Response

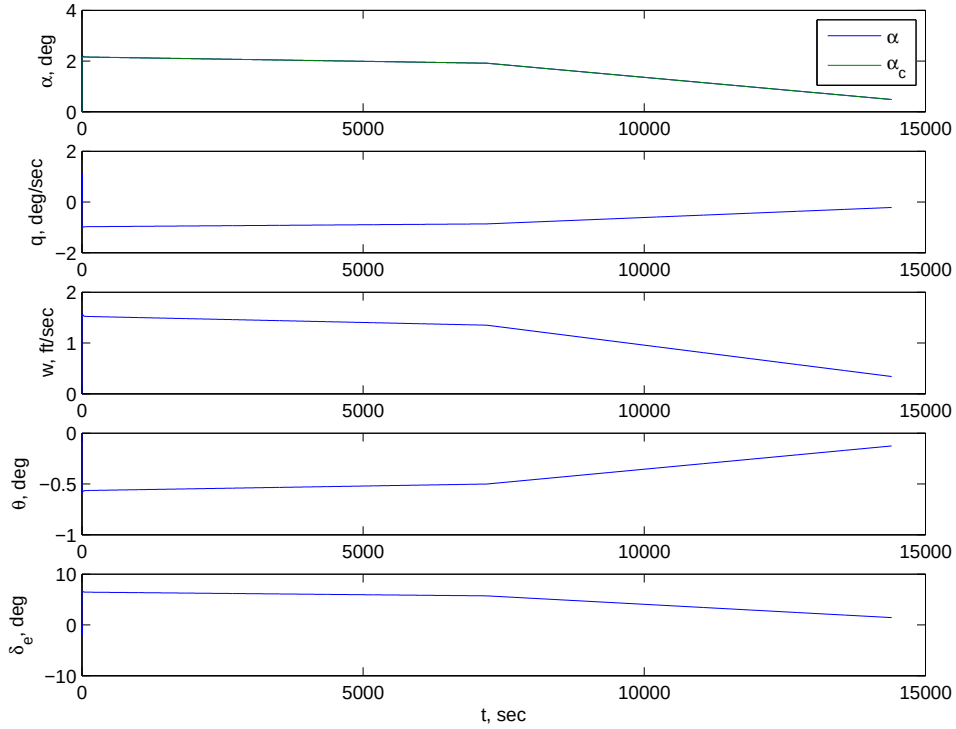

Figure 6.3 - Aircraft Responses

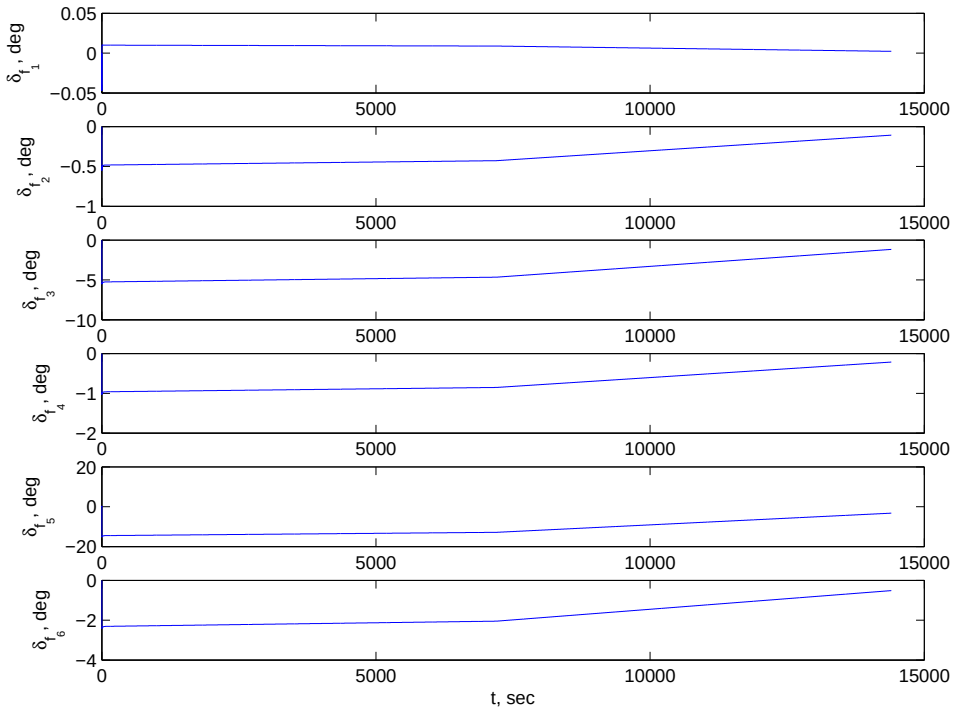

Figure 6.4 - Wing Shaping Control Flap Inputs (Non-Optimized for Drag Minimization)

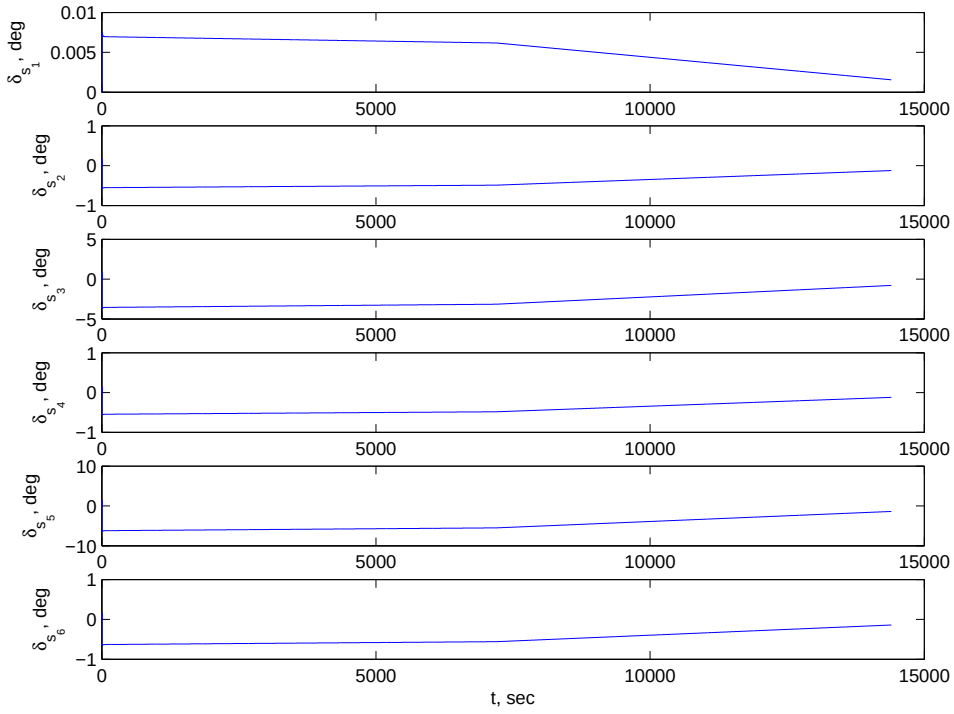

Figure 6.5 - Wing Shaping Control Slat Inputs (Non-Optimized for Drag Minimization)

7 Discussion

The optimization study has identified some potentially promising concepts such as the drooped wing shape, inflected wing shape, and squashed fuselage. The potential drag reduction appears significant. However, this drag reduction may be associated mostly with lift-induced drag. It is still unclear how much changes in parasitic drag associated with these concepts would be. Therefore, more work would be needed to verify the potential drag reduction benefits of these concepts. High-fidelity CFD codes that capture viscous and compressibility effects may be able to better shed light on the merits of these new concepts. Nonetheless, the results of this study do warrant further investigation.

In terms of new revolutionary concepts such as drooped wing shapes if their drag reduction benefits are verified, current constraints in aircraft development capabilities may preclude such concepts to be adopted due to potential technical challenges in many different areas. One obvious area is materials and structure. To accommodate such a wing shape, radical changes in material choices and structural design processes would have to occur. With wing shaping control design, cyclic loadings on aircraft wings during cruise would potentially result in fatigue life issues. Advances in composites material development may be able to address some of the challenges in materials and structure.

Another obvious challenge with the drooped-wing aircraft concept is ground clearance. Figure 5.8 shows that the tip of the aeroelastic tailored as-built drooped wing shape is below BWL 0, which implies that the wing tip would touch the ground. Folded wing concepts such as those used in many World War II vintage aircraft could be used to increase ground clearance for take-off and landing.

Figure 7.1 - Folded Wing Configuration for Take-Off and Landing

The inflected-wing and the squashed-fuselage aircraft concepts may have a better chance for concept adoption without major radical changes to the current aircraft development capabilities. Some technical challenges may still be encountered with these configurations as with any new aircraft configuration no matter how feasible it may look.

Wing shaping control appears to have a potential drag reduction benefit. The study shows that to harvest the potential of wing shaping control, configuration changes in high-lift devices would have to be a part of the wing shaping control strategy. Flap and slat devices inherently generate drag as they increase lift. Conventional flap and slat systems as in the current generation aircraft are not aerodynamically efficient enough for drag-reducing control strategies like wing shaping control. The variable camber continuous trailing flap concept developed in this study does seem to offer a big pay-off for drag reduction even when used in current generation aircraft. Technical challenges would exist as the increase in the number of multiple segmented flaps that form a variable camber continuous flap surface would lead to increased complexity.

Another observation is made with regards to a wing shaping control strategy using flap-type actuation devices in that aerodynamic efficiency, which is the lift-to-drag ratio, would dictate wing shaping control flaps to operate only in the positive (downward) flap deflections. For a positively cambered wing section, a positive flap deflection causes the airfoil camber to increase that in turn generates more lift. Any attendant drag increase as a result of lift increase would be more desirable than drag increase as a result of lift decrease, as would be the case with negative (upward) flap deflections. The optimal point in cruise to harvest the most potential out of wing shaping control would be at the start of cruise when the aircraft wing would be at its desired optimal wing shape, which would require aeroelastic tailoring of the as-built wing shape.

Finally the issues of wing flexibility on vehicle stability cannot be ignored. No matter how aerodynamically efficient an aircraft would be, it would never fly if it is unstable. Flight control can be used to stabilize aeroelastic instability that may be associated with wing flexibility, as demonstrated in this study. However, a stable aircraft is always desirable for commercial aviation. Aeroelastic tailoring by properly distributing wing stiffness throughout the airframe may also improve stability margins of aeroelastic modes. The role of flight control is then relegated to stability augmentation which would reduce the demand on a flight control system. In any case, increased wing flexibility would result in more susceptibility to potentially severe responses to air turbulence and wind gusts. Flight control design would need to take this issue into consideration. The Boeing 787 Dreamliner aircraft is equipped with

a gust load alleviation control technology called Smooth Ride technology. Such a concept may become standard one day for aircraft flight control design as the trend in aircraft design is moving toward a more flexible airframe design for increased performance and reduced fuel burn.

8 Recommendations for Future Work

The study has completed all the objectives as outlined in the NASA Innovation Fund proposal. It is believed that the main goal of creating new ideas that could break new ground in aerospace technologies as sought for by NASA Innovative Partnerships Program has been met through the execution of this project. The study culminates in several recommendations by the NASA project team as well as Boeing Research and Technology, an industry partner participating in the study.

8.1 NASA Project Recommendations

The study has identified several interesting concepts that may hold potential for future development of next generation air vehicles to meet national and global challenges of reducing fuel burn. Three promising concepts have emerged that merit further investigation as part of a follow-on study.

- Drooped and inflected wing shapes and squashed fuselage for drag reduction
- Variable camber continuous trailing edge flap concept for wing shaping control and low drag lift augmentation
- Elastic wing shaping control for drag reduction

While the results appear promising, much work still lies ahead to realize the potential and to further mature these concepts into tangible technologies for future development of new air vehicle concepts. Some of the topics that should be further pursued include, but are not limited to the following:

1. Verification with High-Fidelity Navier-Stokes CFD Code:

   To investigate potential merits of these concepts, high-fidelity CFD tools such as the OVERFLOW code should be used to verify the drag benefits of these concepts. Both VORVIEW and Cart3D are inviscid codes which do not capture potential viscous boundary layer separation. Notwithstanding the drooped wing and inflected wing shape concepts which may be far-termed, the squashed-fuselage concept may have a near-term impact for drag reduction benefits. Therefore, at a minimum, this concept should be further evaluated.

2. Further Optimization:

   The aerodynamic optimization conducted in VORVIEW is quite limited in scope in that a prescribed 4th-degree polynomial shape function is used for the parametric optimization. The optimal solutions were found within a design space that may be too constrained. By removing the shape function constraint or using other types of shape functions, potential improved optimal solutions could be realized. This optimization could be performed with VORVIEW or Cart3D with the adjoint-driven adaptation module to ensure accurate simulations. This ability would provide error estimates to ensure that the drag improvement numbers are meaningfully larger than the numerical error in the simulations.

3. Investigation of Variable Camber Continuous Flap-Type Control Surfaces:

   The variable camber continuous trailing edge concept developed in this study can hold potential for achieving significant drag reduction benefits. The concept provides a continuous trailing edge surface without any discontinuity typically associated with conventional flap-type control surfaces. Boeing Research and Technology has expressed interest in the concept. As a follow-on work, further development of this concept is highly recommended. This development would include better aerodynamic modeling of the flap concept including Navier-Stokes CFD modeling to better understand the performance of the flap concept. From a system-level perspective, partnerships with Boeing Research and Technology could potentially transition this concept into a prototype system for further evaluation in a wind tunnel.

4. Development of Drag Minimization Multi-Objective Wing Shaping Flight Control:

   The advantage of wing shaping for drag reduction has been demonstrated by analysis in this study. Wing shaping is a revolutionary biologically-inspired concept that actually mimics avian flight. Taking cue from highly adaptable wing shapes of birds, this concept can hold promising potential for future air vehicle concept. As a follow-on work, it is recommended that this work be further pursued. Further work is needed to develop

a drag minimization multi-objective flight control with wing shaping capabilities as well as to extend the wing shaping capabilities for other objectives in a typical flight envelope such as high-lift augmentation during take-off and landing.

5. Development of Coupled Aeroelastic-Aerodynamic Modeling Capability:

   The ability to model aeroelastic effects on aerodynamic performance of future vehicles is much needed. These effects have been shown in this study to be quite significant as aeroelastic deflections can result in a large drag penalty. The trend in aircraft development is moving toward the use of light-weight structural materials that could increase airframe flexibility which could exacerbate drag characteristics. By developing a better modeling capability, complex interactions of aeroelasticity with aerodynamics can be captured to improve aerodynamic prediction of future vehicles. As a start, a follow-on work should be considered to develop a method for coupling some existing aeroelastic models such as the one developed in this work with an aerodynamic code like VORVIEW or Cart3D. The aeroelastic code would compute aeroelastic bending and torsional deflections which would then be used to generate a deformed geometry of an aircraft model. The aerodynamic code would compute a flow solution for the deformed model and pass the aerodynamic information back to the aeroelastic code for the next iteration of aeroelastic deflection computation. The iterative solution method would converge when the error in the deformed geometry reaches a prescribed error tolerance.

6. Further Development of Aeroelastic Flight Dynamic Model:

   The aeroelastic model developed in this work only includes longitudinal dynamics. Further development is needed to incorporate aeroelastic coupling for the lateral-directional axes. The model should include methods for computing aerodynamic derivatives due to aeroelastic deflections. The goal of the work is to develop a comprehensive flight dynamic model that includes all the rigid aircraft states as well as elastic aircraft states to account for aeroelastic modes. This flight dynamic model would be highly useful for a flight control development to stabilize potential aeroelastic instability associated with elastically shaped future air vehicle concepts.

8.2 Boeing Research and Technology's Recommendations

Boeing Research and Technology has provided the following recommendations for future work to further develop flight control applications:

1. The wing leading and trailing edge multiple flap surfaces can be used for a variety of control requirements. This combination of control surfaces can also apply to flexible wings that are designed in a straight rather than in a droop configuration. Applications can result in performance drag reduction or enhanced roll control. Some of these applications include:

   Roll Control: During cruise and during take-off and landing, a combination of flaps can be applied to roll the aircraft at required rates. A balance of leading and trailing edge flaps can be used to ensure that the twist of the flexible wing does not result in roll reversal. With use of an adaptive or feedback gain schedule, a very consistent roll rate per stick command can be achieved.

   Another way to roll a flexible wing aircraft is to use some of the leading edge control surfaces to establish a twist in the wing in the direction of the desired roll. This method was flight demonstrated in the NASA/Boeing Active Aeroelastic Wing (AAW) program [9]. A NASA F/A-18 was configured with a flexible wing, and an outboard leading edge flap used to twist the wing for roll control. The horizontal stabilator was set for symmetric pitch response only. Usually the stabilators are dominant in rolling the aircraft at higher speeds due to the roll reversal using ailerons. The AAW program quite successfully demonstrated effective roll control.

   Lift Change: Lift can be increased for takeoff and landing; The wing flaps deploy to effect a wing airfoil shape that can increase the lift for a given angle of attack. After takeoff, the high lift configuration can be altered for varying flap deployment, thus gradually reducing drag during the climb-out to cruise conditions. For cruise flight, the wing slats and flaps can be used to change the wing span-wise lift distribution so that an optimum minimum drag profile can continually be achieved. This may involve both the flap position and the twist of the wing as a function of span.

   Trim for Minimum Drag: Another use for the wing slat and flap controllers is trim configurations that minimize drag. The horizontal tailplane together with the wing control surfaces are commanded to establish optimum

aircraft trim while maintaining an aft center of gravity via fuel transfer. The balance between wing slats and flaps can establish a pitching moment to permit off-loading the horizontal tail settings for the net trim, selecting this balance for minimum drag optimization. As the wing surfaces change, the downwash behind the wing will also change. This can critically affect the horizontal stabilizer position and drag. An adaptive control method can be applied to find the combination of wing flaps and slats together with the stabilizer and elevator trim settings that give minimum drag. For asymmetric aircraft mass distribution conditions, slat and flap settings can be optimized for each wing while maintaining minimum drag profiles.

Directional Control: By using opposite commands on the adjacent wing flaps, a yawing moment can be generated with little change to lift. Using several of these pairs, a yaw control system can be obtained that can stabilize the directional control of the vehicle or establish a sideforce through yaw that can aid cross-wind control situations. This yaw control combined with differential thrust control permits reduction in the size and weight of the vertical tail. For steady sideslip conditions, use of split adjacent flaps on one wing can trim out the sideslip without the need for rudder trim that may induce additional drag.

Another use for split flaps is to create additional drag that may be needed during steep descent flight profiles for air traffic control flight paths that save time and fuel.

Stabilization of Wing Flexible Bending Modes: Flight control modes can be installed that suppress wing structure oscillations that are caused by the flexible design of the wing. Both wing vertical bending and wing torsional bending modes can be suppressed. The flap actuation rates and dynamics must have sufficient bandpass to deal with the higher frequency wing flexibility modes. This requires actuation drive motors that can provide sufficient acceleration to achieve the higher bandpass. These leading and trailing control surfaces will act to reduce the oscillation magnitudes. Not all of the control surfaces are needed for this function. Remaining surfaces not used for this task can have a lower controller bandpass. Acceleration sensors mounted at the maximum deflection location on the wing will provide the control commands sent to certain selected leading and trailing edge surfaces that will suppress the structural mode oscillations to acceptable values. This can be done by changing the actuator command phase angle so that the resulting surface response counter balances the phase of the oscillations.

2. Variable Camber Flap Design for Optimum Control Drag Reduction: Conventional flaps for each segment on the wing trailing edge may result in increased drag at cruise conditions for large flap deflection. A method to segment the flap into multiple sections results in a variable flap camber that provides the necessary force but with less flap deflection and consequently less drag due to the wing control surfaces. Each flap segment would have sufficient flexibility to exactly fit the end of the adjacent flap resulting in a continuous flap surface for cruise.

   Figure 8.1 illustrates the same airframe as the baseline vehicle with trailing edge flaps in a continuous and three segment Variable Camber configuration. There are twelve trailing edge flaps instead of the six flaps on the baseline aircraft (shown in Figure 3.1). The Variable Camber cross section compared to the baseline flap is shown in Figure 8.2. The three segments of the flap would be scheduled in the deflection gearing to an optimum camber for either up or down deflection. The overall deflection pattern for each flap will be set to maintain the best wing droop position for minimum drag. The drag reduction payoff using the variable camber flaps is significant; Figure 8.3 shows the drag coefficient for an example setting of 3.28^{o} up and 3.92^{o} down positions.

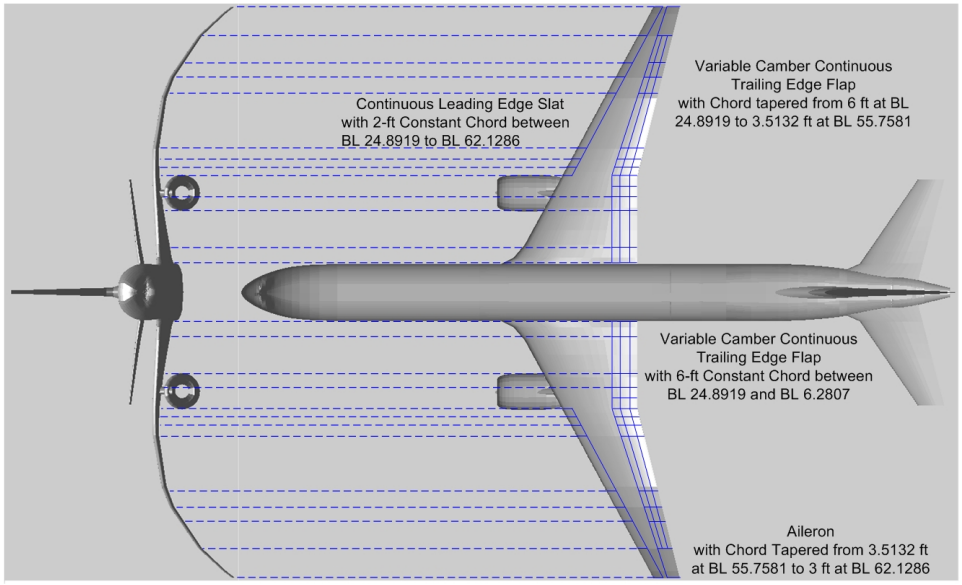

Figure 8.1 - Variable Camber Continuous Trailing Edge Flap System

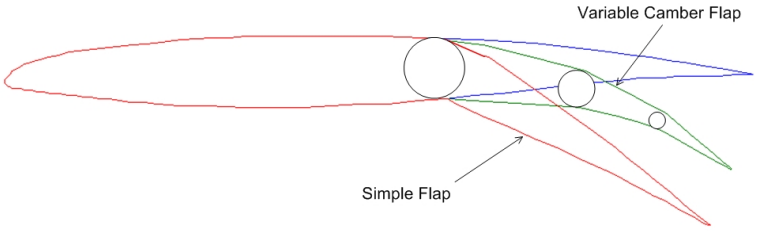

Figure 8.2 -Variable Camber Flap

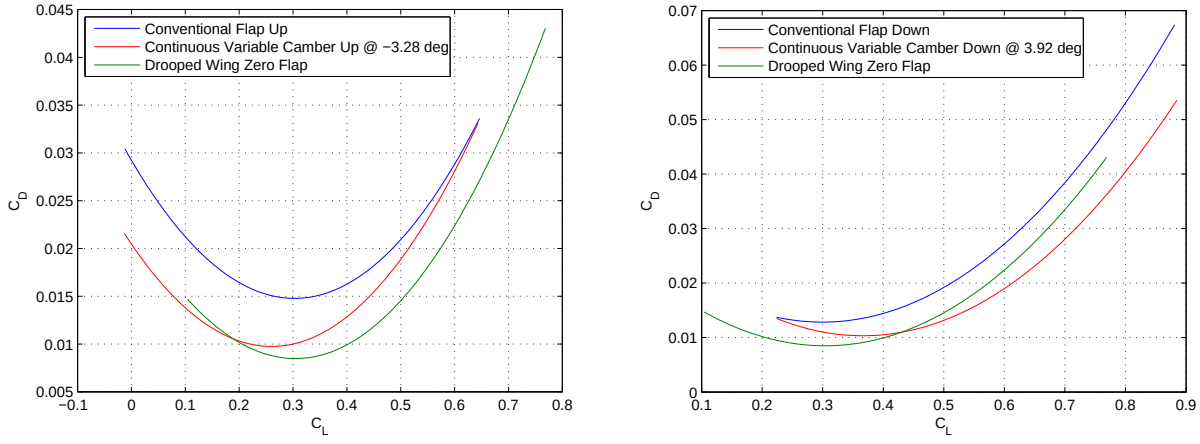

Figure 8.3 - Drag Polars for Plain Discrete Flaps and Variable Camber Continuous T.E. Flaps

Over the last two years Boeing Platform Subsystems Technology (St. Louis, MO) has been engaged in its research and development activities in looking at the performance improvements potential of utilizing split

tabbed flap surfaces (including splitting the surface in multiple locations beyond trim surface addition). The purpose of this research is to evaluate the ability of this adjustable camber of the flap surfaces to both improve overall aerodynamic performance of the aircraft while reducing the need for high power flight control actuation where possible.

3. Roll Control Using Alternate Control Surfaces: Equipping the aircraft with separate left and right control elevators enables roll control primarily for cruise conditions. Rudders can be used to control sideslip to further condition the roll.

4. Roll Control Using the Engines: Use of differential thrust changes is an effective method to roll the aircraft and also for use in limiting the maximum bank angle to prevent entry into an unsafe flight envelope that can initiate a loss of control flight trajectory. For effective roll control, engine dynamic thrust response must be sufficient to prevent excessive thrust response time that can degrade roll handling qualities of the aircraft.

9 Conclusions

This report presents the findings of the NASA Innovation Fund project entitled "Elastically Shaped Air Vehicle Concept". The study has completed all the objectives as outlined in the NASA Innovation Fund proposal. New concrete ideas have been developed to meet the intent and spirit of the NASA Innovation Fund Award. Three emerging themes have been developed in support of meeting national and global aviation challenges of reducing fuel burn for present and future aviation systems. These themes are intertwined and promote the multi-disciplinary nature of the goal of drag reduction in current and future air vehicles.

The first theme addresses the drag reduction goal through innovative vehicle configuration optimization with out-of-the-box thinking. Three new promising concepts have been identified from this theme: a drooped wing shape, an inflected wing shape, and a squashed fuselage. The drooped wing shape is a truly biologically inspired wing concept that mimics a seagull wing and could achieve about 5% to 6% drag reduction, which is aerodynamically significant. The aerodynamic efficiency gain is theoretically justifiable from aeroelasticity theory. The inflected wing concepts could achieve about 3% drag reduction. While the benefit may be modest with the inflected wing, the concept could have a near-term impact since this concept could be developed within the current aircraft development capabilities. The squashed fuselage concept is found to have a substantial drag reduction benefit. Up to 15% drag reduction has been seen in the study. By changing the cross sections of the fuselage, the fuselage can contribute to vehicle lift, thereby reducing the wing lift which in turn reduces lift-induced drag. As with the inflected wing concept, the squashed fuselage could have a near-term impact.

The second theme addresses the drag reduction goal through a new concept of elastic wing shaping control. The multi-disciplinary nature of flight physics is appreciated with the recognition of the adverse effects of aeroelastic wing shape deflections on aerodynamic drag. By aeroelastically tailoring the wing shape with active control, a significant drag reduction benefit could be realized. A 17% drag reduction for long-range cruises from elastic wing shaping control could be realized as has been shown in the study when compared with the drooped-wing aircraft configuration without elastic wing shaping control.

To realize the potential of the elastic wing shaping control concept, the third theme emerges that addresses the drag reduction goal through a new type of aerodynamic control surfaces. This concept is referred to as variable camber continuous trailing edge flap. Conventional aerodynamic control surfaces are discrete independent surfaces that cause geometric discontinuities at the trailing edge region. These discontinuities promote vorticities which result in drag rises. The variable camber trailing edge flap concept could provide a substantial drag reduction benefit over a conventional discrete flap system. Aerodynamic simulations show a drag reduction of over 50% could be achieved with the flap concept over a conventional discrete flap system. Moreover, elastic wing shaping control potential could only be realized with low drag aerodynamic control surfaces such as this flap concept.

Research and technology development of new vehicle concepts to support the drag reduction goal requires a multi-disciplinary approach that integrates knowledge domains across different disciplines to bring forth potential solutions that recognize the interactive nature of these disciplines in contributing to the common goal of drag reduction. The project recognizes this important aspect of research and technology development and proceeds to conduct a multi-disciplinary study that brings together a diverse set of disciplines in aerodynamics, optimization, structural analysis and aeroelasticity, flight dynamics and control, and system analysis to develop integrated solutions for future vehicle systems.

The potential significant contributions of this project to future aviation systems in supporting national and global challenges of fuel efficiency could only be realized by continuing to advance these new ideas toward higher levels of technology readiness through a scientific discovery process that would require more thorough analysis, computation, and experimentation than what has been accomplished by this project within the four-month performance period. Toward that end, the project has compiled a list of recommendations from NASA project personnel and Boeing Research and Technology in St. Louis, the project's industry partner, for a possible follow-on effort to mature these ideas into new areas for research and technology development for future aviation systems. In particular, Boeing Research and Technology has expressed a strong interest in future partnership with NASA to further advance the system-level concepts developed by the project; namely, the variable camber continuous trailing edge flap and the elastic wing shaping control, for possible future aircraft applications. Furthermore, Boeing Research and Technology has also indicated that they will share the results of this study with Boeing Airplane Company in Seattle.

In terms of other accomplishments, the project has filed a NASA Disclosure of Invention and New Technology (Including Software) entitled "Variable Camber Continuous Aerodynamic Control Surfaces and Methods for Active Wing Shaping Control" with NASA Ames Office of the Chief Counsel on October 8, 2010. On a related note, upon

a request of the NASA Aeronautics Research Mission Directorate (ARMD) Subsonic Fixed Wing (SFW) project personnel at NASA Langley at the final project meeting, the project has agreed to allow the SFW project personnel to use the variable camber continuous trailing edge flap concept for their future work. The project is also planning to file one or more invention disclosures on the new aircraft concepts developed by the project. In addition, the project will also plan to file an invention disclosure on the aircraft optimization software tool as well as to further develop the optimization tool for future NASA work. The project will plan to publish the results of this study through NASA publication such as NASA Technical Memorandum and technical papers at the American Institute of Aeronautics and Astronautics (AIAA) Atmospheric Flight Mechanics Conference in 2011 and Aerospace Sciences Meeting in 2012.

In closing, the project team wishes to thank NASA Innovative Partnerships Program for their funding support of this project that has allowed new ideas to be developed that could make positive impacts on the future of aviation. These new ideas could give a new impetus to future aircraft design that would be better able to meet national and global challenges of improving fuel efficiency in environmentally responsible future aviation systems.

References

[1] Jordan, T. L., Langford, W. M., Belcastro, C. M., Foster, J. M., Shah, G. H., Howland, G., and Kidd, R., "Development of a Dynamically Scaled Generic Transport Model Testbed for Flight Research Experiments," AUVSI Unmanned Unlimited, Arlington, VA, 2004.

[2] Stanford University, AA241, "Aircraft Design: Synthesis and Analysis," http://adg.stanford.edu/aa241/structures/weightstatements.html

[3] Nguyen, N. T., Nelson, A., and Pulliam, T., "Damage Adaptive Control System Research Report," Internal NASA Report, April 2006.

[4] Miranda, L.R., Elliot, R.D., and Baker, W.M., "A Generalized Vortex Lattice Method for Subsonic and Supersonic Flow Applications," NASA CR-2865, 1977.

[5] Aftosmis, M. J., Berger, M. J., and Melton, J. E., "Robust and Efficient CartesianMesh Generation for Component- Based Geometry," AIAA Journal, Vol. 36, No. 6, 1998, pp. 953-960.

[6] Nemec, M., Aftosmis, M. J., Murman, S. M., and Pulliam, T. H., "Adjoint Formulation for an Embedded-Boundary Cartesian Method," AIAA 2005-0877, 43rd AIAA Aerospace Sciences Meeting, Reno, NV, Jan. 2005. (Also NASA Technical Report NAS-05-008)

[7] Nemec, M., Aftosmis, M. J., and Wintzer, M., Adjoint-Based Adaptive Mesh Refinement for Complex Geometries, AIAA 2008-0725, 46th AIAA Aerospace Sciences Meeting, Reno, NV, Jan 2008.

[8] Roach, J., "Seagulls May Inspire New Airplane Wings," http://news.nationalgeographic.com/news/2006/10/061024-seagull-wings.html, National Geographic News, October 24, 2006.

[9] The Boeing Company, "The Active Aeroelastic Wing Flight Research Program (The X-53) Final Report,",Vol. I and II, AFRL-VA-WP-TR-2005-3082, October 2005.

[10] Theodorsen, T. and Garrick, I.E., "Mechanism of Flutter - a Theoretical and Experimental Investigation of the Flutter Problem", NACA Report 685, 1940.

[11] Theodorsen, T, "General Theory of Aerodynamic Instability and the Mechanism of Flutter", NACA Report 496, 1935.

[12] Roskam and Lan, *Airplane Aerodynamics and Performance*, DARcorporation, 1997.

[13] Hodges, D.H. and Pierce, G.A., *Introduction to Structural Dynamics and Aeroelasticity*, Cambridge University Press, 2002.

[14] Nguyen, N. T., "Integrated Flight Dynamic Modeling of Flexible Aircraft with Inertial Force-Propulsion-Aeroelastic Coupling," AIAA-2008-194, 46th AIAA Aerospace Sciences Meeting, Reno, NV, Jan 2008.

[15] Houbolt, J. C. and Brooks, G. W., "Differential Equations of Motion for Combined Flapwise Bending, Chordwise Bending, and Torsion of Twisted Nonuniform Rotor Blades," NACA Technical Note 3905, February 1957.